THERMOPOROELASTIC EFFECTS OF DRILLING FLUID TEMPERATURE ON

ROCK DRILLABILITY AT BIT/FORMATION INTERFACE

A Thesis

by

KRITATEE THEPCHATRI

Submitted to the Office of Graduate Studies of
Texas A&M University
in partial fulfillment of the requirements for the degree of

MASTER OF SCIENCE

Approved by:

Chair of Committee,   Frederick E. Beck
Committee Members,   Rashid A. Hasan
                    Jerome J. Schubert
                    Yuefeng Sun
Head of Department,   A. Daniel Hill

December 2012

Major Subject: Petroleum Engineering

ABSTRACT

A drilling operation leads to thermal disturbances in the near-wellbore stress, which is an important cause of many undesired incidents in well drilling. A major cause of this thermal disturbance is the temperature difference between the drilling fluid and the downhole formation. It is critical for drilling engineers to understand this thermal impact to optimize their drilling plans.

This thesis develops a numerical model using partially coupled thermoporoelasticity to study the effects of the temperature difference between the drilling fluid and formation in a drilling operation. This study focuses on the thermal impacts at the bit/formation interface. The model applies the finite-difference method for the pore pressure and temperature solutions, and the finite-element method for the deformation and stress solutions. However, the model also provides the thermoporoelastic effects at the wellbore wall, which involves wellbore fractures and wellbore instability.

The simulation results show pronounced effects of the drilling fluid temperature on near-wellbore stresses. At the bottomhole area, a cool drilling fluid reduces the radial and tangential effective stresses in formation, whereas the vertical effective stress increases. The outcome is a possible enhancement in the drilling rate of the drill bit. At the wellbore wall, the cool drilling fluid reduces the vertical and tangential effective stresses but raises the radial effective stress. The result is a lower wellbore fracture gradient; however, it benefits formation stability and prevents wellbore collapse.

Conversely, the simulation gives opposite induced stress results to the cooling cases when the drilling fluid is hotter than the formation.

DEDICATION

I would like to devote my success to,

My beloved parents and sisters for their love, cares, and encouragements. Without them, I would not have come this far.

My beloved fiancée for her love, support and understanding throughout my study. Her presence gives me strength to pass through all obstacles.

Professors and friends at Texas A&M University for advice and friendships. They made my away-from-home journey so memorable.

ACKNOWLEDGEMENTS

I would like to sincerely thank my committee chair/advisor, Dr. Beck, for his support, guidance and patient during the past two years. His knowledge and direction were the keys leading to my success in research.

I would like to extend my appreciation to my thesis committee members, Dr. Hasan, Dr.Schubert, and Dr.Sun. Their feedback and support helped elevate my research standard.

I would also like to present my thank to Dr. Charles Aubeny for his class, CVEN647 - Numerical Method in Geotechnical Problem, and time to answer all of questions regarding my research.

Thanks to my friends, colleagues, department faculty and staffs for making my time at Texas A&M University a great experience and memorable.

Thanks also go to Chevron Thailand Exploration and Production for financial support throughout my study abroad.

Finally, thanks to my family and my fiancée for their encouragement and love.

NOMENCLATURE

Alphabets

f_b	Volumetric Body Force (psi/ft^3)
k	Formation Permeability (md)
p	Pore Pressure (psi)
p_w	Wellbore Pressure (psi)
q	Heat Flux (btu/ft^2)
r	Radial Distance or Radius (ft)
r_w	Wellbore Radius (ft)
t	Time (s)
u	Displacement (ft)
v_f	Velocity of Pore Fluid (ft/s)
A	Cross Area (ft^2)
B	Skempton's Pore Pressure Coefficient
C_b	Formation Bulk Specific Heat Capacity (btu/lbm-°F)
C_f	Pore Fluid Specific Heat Capacity (btu/lbm-°F)
C_m	Formation Matrix Specific Heat Capacity (btu/lbm-°F)
C_0	Cohesion Factor (psi)
E	Elastic Young's Modulus (psi)
G	Elastic Shear Modulus (psi)
K	Elastic Bulk Modulus (psi)

K_f	Elastic Bulk Modulus of Pore Fluid (psi)
K_s'	Effective Elastic Bulk Modulus of Solid Constituent (psi)
T	Temperature (°F)

Greek Symbols

Δr	Small Increment in Radial Direction (ft)
Δt	Small Increment in Time Domain (s)
Δz	Small Increment in Vertical Direction (ft)
ν	Drained Poisson Ratio
ν_u	Undrained Poisson Ratio
ω	Angle of Internal Friction (degree angle)
α	Biot's Constant
ϵ	Linear Elastic Strain
γ	Engineering Shear Strain
σ	Total Normal Elastic Stress (psi)
σ'	Effective Normal Elastic Stress (psi)
τ	Shear Stress (psi)
μ	Viscosity (cp)
ϕ	Formation Porosity
α_m^T	Volumetric Thermal Expansion of Formation Matrix (1/°F)
α_m^{TL}	Linear Thermal Expansion of Formation Matrix (1/°F)
α_f^T	Volumetric Thermal Expansion of Pore Fluid (1/°F)

α_p^T	Volumetric Thermal Expansion of Pore Space (1/°F)
κ^T	Bulk Thermal Conductivity (btu/hr-ft-°F)
ρ_b	Formation Bulk Density (lbm/ft^3)
ρ_m	Formation Matrix Density (lbm/ft^3)
ρ_f	Pore Fluid Density (lbm/ft^3)
η	Crank-Nicholson Time-Weighting Parameter

Matrices and Tensors

$[B]$	Differential of Shape Function Matrix
$[H]$	Shape Function or Interpolation Function Matrix
$[K^e]$	Element Stiffness Matrix
$[K^g]$	Global Stiffness Matrix
$[\hat{P}]$	Nodal Pore Pressure Matrix
$[\hat{T}]$	Nodal Temperature Matrix
$[\hat{u}]$	Nodal Displacement Matrix
$[\sigma]$	Stress Matrix
$\langle\sigma\rangle$	Stress Tensor

Subscript

i	Nodal Index in Radial Direction (Positive rightward from Centerline)
j	Nodal Index in Vertical Direction (Positive Downward)

u	Displacement
P	Pore Pressure
T	Temperature

TABLE OF CONTENTS

LIST OF FIGURES

LIST OF TABLES

CHAPTER I

INTRODUCTION

The drilling process creates disturbances to the original state of formation stress near the wellbore. The alteration of near-wellbore stress can create mechanical stability/instability of the wellbore, depending on whether the wellbore is in or severely out of balance. Mechanical instability of the wellbore wall leads to common drilling problems such as heaving shale and lost circulation. However, mechanical instability may not only lead to problems. Rock instability at the bit/formation interface can benefit bit drilling efficiency. This thesis investigated whether near-wellbore stress changes at the bottom of the hole can be manipulated to enhance the drilling process, specifically by enhancing the rate of penetration of the drill bit.

Leading causes of alterations in the near-wellbore stress are evacuation of the formation and temperature differences between the drilling fluid and the formation. The effects of the wellbore geometry have been thoroughly investigated for more than 50 years, whereas the thermal effects on the wellbore stress only recently gained attention, after an introduction of the thermoporoelasticity theory by Kurashige in 1989.

Many contributing factors control changes in formation temperature. The most prominent cause is a temperature gradient between the drilling fluid and the formation. The formation temperature naturally increases with depth below the surface. The earth geothermal gradient typically varies from 0.2°F/100 ft to 11°F/100 ft based on depth, basin type, and tectonic activities in an area. On the other hand, drilling fluid

temperature downhole largely depends on the surface inlet temperature, fluid thermal properties, heat transfer interaction between the formation and the drilling fluid, and heat generated from drilling activities. The drilling fluid temperature at the surface is typically lower than the formation downhole. Thus, the drilling fluid usually acts as a cooling agent for the formation at the bottom of a hole and the deep part of the annulus. However, the drilling fluid gains heat from a hotter formation deep down in the hole and raises its temperature. When it comes in a contact with the cooler formation higher in the hole, the drilling fluid, which now has a higher temperature than the formation, causes a reversed direction of heat transfer and causes the formation temperature to increase.

This thesis focuses on the change in formation stress near the wellbore where the temperature gradient in the formation near the wellbore is affected by the drilling fluid temperature. The formation stress around the wellbore vicinity is critical to in the success of well drilling and dictates many wellbore behaviors that could have undesirable impacts on a drilling operation. Gonzalez et al. (2004) observed that a wellbore fracture gradient increased from its original formation leak-off test (LOT) when the drilling operation progressed and the wellbore was exposed to a rise in the drilling fluid temperature. Hettema et al. (2004) traced lost-circulation incidents to wells drilled through cooled formations connected to nearby water injection wells, whereas no circulation was lost in offset wells drilled far away from these zones. They concluded that the drilling fluid in the wells that passed through the water-injection zones was cooled by the formation in that region. This caused a reduction in a formation fracture gradient, leading to an unexpected wellbore fracture. Krausmann (2011) observed that

high-temperature/high-pressure (HTHP) wells drilled with water-based fluid, which naturally has lower fluid temperature than oil-based fluid, gave better rates of penetration.

Stress transformations in the formation near the wellbore are known to have considerable impact on drilling operations. This thesis specifically studied whether the thermal impact on the formation stresses at the bottom of the hole impact the rate of penetration of the drill bit. This study required development of a theoretical basis to represent the formation stress change caused by thermal effects at the bit/formation interface. Fulfilling this objective requires a thorough understanding of the relationship between temperature changes and induced formation stress, coupled with a rock-failure model.

1.1 Background and Motivation

An incident that gave rise to this research interest is an observation from an HPHT well drilling operation (Krausmann, 2011). The HTHP wells drilled with water-based fluid offered superior rates of penetration over similar offset wells drilled with oil-based fluid. This finding correlates well with the fact that the water-based fluid experienced lower downhole fluid temperatures than the oil-based fluid. With knowledge of thermal stress, one valid hypothesis is that the thermal effects on formation stress at the bit/formation interface is a key mechanism behind the difference in drilling rates in this HTHP case.

A literature review reveals the impacts of temperature on formation stress and formation failure margin (Wang et al., 1996; Li et al., 1999; Chen and Ewy, 2005; Farahani et al., 2006; Zhai et al., 2009; Wu et al., 2010), usually relating them to aspects of the impacts on wellbore stability and a safe mud-weight window. A cooled formation helps increase a wellbore's resistance to collapse while weakening the fracture resistance. The results are reversed for the case in which a formation is heated by drilling fluid.

Though many published works have explored thermal impacts on formation stress, we did not find any reference on the thermal effects at the bottom of the hole. An explanation may be that many major incidents in drilling operations are related to a wellbore-wall condition more than bottomhole conditions. Nonetheless, one key objective in drilling is a rate of penetration, which directly connects to the strength of the formation at the bit/formation interface.

1.2 Scope and Objective

The objective of this thesis is to develop a numerical model to provide a theoretical basis either supporting or denying the hypothesis that formation cooling at the bottom of the hole helps enhance formation drillability.

The model gives numerical results: thermally induced temperature, thermally induced pore pressure, and thermally induced effective stresses. The impact on rate of penetration is deduced by using appropriate rock failure criteria governing the bit-formation interaction.

The model features three major assumptions that help lessen the solution's complexity and reduce computational effort without sacrificing the validity of the findings. The first assumption is that a solid matrix has lower compressibility than pore fluid. Therefore, a volumetric change of pore fluid dominates a change in pore pressure. The second assumption is that heat conduction governs the heat transfer inside the formation. This assumption is justified by our main application on a shale formation, which has low permeability, so that the effect of fluid flow on heat flux is negligible. Finally, the model assumes that the formation is a linear-elastic porous material with isotropic properties and fully saturated with pore fluid. This assumption leads to a mathematical linear solution, which allows the application of the superposition theory.

1.3 Methodology

This study uses the thermoporoelasticity theory to solve thermal impacts on stresses in the formation. The theory describes the relationships among solid matrix deformation, pore fluid pressure, and formation temperature for an isotropic linear elastic material. Three main governing equations are associated with this thermoporoelasticity theory: the mechanical force balance equation, the pressure diffusivity equation, and the thermal diffusivity equation. With the three assumptions discussed earlier, the effect of a solid matrix deformation is decoupled from the pressure diffusivity equation, and the heat convection term is dismissed from the thermal diffusivity equation.

The finite-element and finite-difference methods are used in this study. The temperature and the pore pressure diffusivity equations are formulated with the finite-difference method to avoid a spurious response in the finite-element solver caused by a small time increment and low diffusivity properties of the formation. The finite-element method is used to formulate the deformation equation, which gives displacement and stress solutions.

This thesis combines two independent numerical modules. The first one is a solver for the stress-state solution caused by evacuation of formation to make a cylindrical vertical hole with a flat circular bottom. This module uses the poroelasticity theory, which is an isothermal form of thermoporoelasticity, as the governing concept with the Fourier-assisted finite-element formulation. The second module is for a thermally induced stress solution from the temperature difference between the drilling fluid and the formation. The latter model applies the partially coupled thermoporoelasticity concept, which decouples a solid-matrix deformation effect from a pore-pressure change and considers only heat conduction inside a formation.

The superposition of the responses from the two modules gives a complete solution of interest. The final step is to transform a complete stress solution at the bottom of the hole into the Drucker-Prager and tensile failure indices to relate the stress state to a likelihood of rock failure. The formation failure indices at the bit/formation interface imply a rate of penetration response, as our objective requires.

1.4 Applications

This study directly improves the understanding of how drilling fluid temperature affects formation drillability. The results are suitable for drilling in shale formations. This fits well with many U.S. gulf coast drilling operations where shale is the dominant formation type. Additionally, a simplification of decoupling the solid-matrix deformation from the pressure-diffusivity equation makes this model suitable for formations that have lower compressibility than the pore fluid. The modeling method should be applicable to other types of formations with similar characteristics as well.

The main areas of application for this study relate to formation strength, an indicator of formation failure, and wellbore stability. The model offers an understanding of stress alteration from thermal effects at the bottom of the hole, which can help a drilling team improve planning. Optimum drill-bit selection, drilling fluid design, and selection of drilling parameters can all be impacted by this research. A theoretical explanation of the HTHP case study will bring awareness of the potential drilling rate benefits of water-based drilling fluid over oil-based drilling fluid. Furthermore, this model presents thermal effects at the wellbore wall along the top boundary of the model. This solution could help an engineer improve a drilling fluid program and design a mud-weight window to avoid unexpected nonproductive incidents such as lost circulation or borehole collapse.

1.5 Sign Convention

A sign for stress in this thesis is compressive positive following a standard of the geomechanic sign convention. However, the finite-element computer codes for the thermoporoelastic solution in this thesis use a tensile positive sign convention to comply with a sign used in the finite-element method for boundary loads.

CHAPTER II

LITERATURE REVIEW

2.1 Rock Mechanics in Drilling

Major factors affecting wellbore stability include rock properties, in-situ stresses, well trajectory, pore pressure, chemical contents in drilling fluid, temperature, mud weight, and time. These factors have been the center of studies of stability since the first examination of stress in the 1950s. In one of the earliest studies, Deily and Durelli (1958) performed a photoelastic analysis using a hollowed cylinder made from the Bakelite Marblette to study bottomhole stresses. Their results revealed that the radial and tangential stresses at the center of a hole are always less than the overburden pressure but are greater at the edge of the hole; the difference in stress level between the center and the edge was 60% in mud drilling and up to 395% in air drilling. They concluded that the effect of higher stresses at the wellbore edge would increase rock strength in the area near the wall at the bottom of the hole (Figure 2.1).

In the normal fault stress regime, the stable drilling direction is always parallel to a direction of the minimum horizontal principal stress. The deviation angle from the vertical to maximize wellbore stability increases when the ratio of the maximum horizontal principal stress to the vertical stress increases (Zhou et al. 1996). In the strike-slip stress regime, the horizontal well is the most stable wellbore, and the best drilling direction for wellbore stability turns more toward the maximum horizontal stress azimuth when the ratio of the maximum horizontal principal stress to the vertical stress

increases. These concepts are useful to evaluate rock compressive failure at the wellbore

wall and to predict a safe mud weight window.

Figure 2.1 – The radial and tangential stresses at the bottom of the hole when drilling
with water from photoelastic analysis (from Deily and Durelli, 1958).

In the normal fault stress regime, the stable drilling direction is always parallel to

a direction of the minimum horizontal principal stress. The deviation angle from the

vertical to maximize wellbore stability increases when the ratio of the maximum

horizontal principal stress to the vertical stress increases (Zhou et al. 1996). In the

strike-slip stress regime, the horizontal well is the most stable wellbore, and the best

drilling direction for wellbore stability turns more toward the maximum horizontal stress

azimuth when the ratio of the maximum horizontal principal stress to the vertical stress

increases. These concepts are useful to evaluate rock compressive failure at the wellbore

wall and to predict a safe mud weight window.

10

A different model, based on the grain-scale discrete-element method (DEM), can be used to evaluate rock failure in formations for three cases: anisotropic stress without mud pressure, anisotropic stress with varying mud pressure, and transient pore-pressure diffusion (Kang et al., 2009). The results of the DEM models agree well with field experience and serve as a good tool in post-failure wellbore-stability analysis. However, the DEM simulator is very computationally expansive.

Finite-element simulation using a fully-coupled 3D poroelastic model has been used to study wellbore geometry and pressure differences in a stress state at the bottom of a hole under anisotropic in-situ stress (Chang et al., 2012). The model assumes isotropic rock properties, water-saturated pores, an isothermal system, and Darcy's pore-space fluid flow. The results show that the maximum principal stress at the bottomhole surface is independent of differential pressure and maximum horizontal in-situ stress but has a reversed relationship with the minimum horizontal in-situ stress. The minimum principal stress rises when the differential pressure increases but decreases when the maximum horizontal in-situ stress increases (Figure 2.2.)
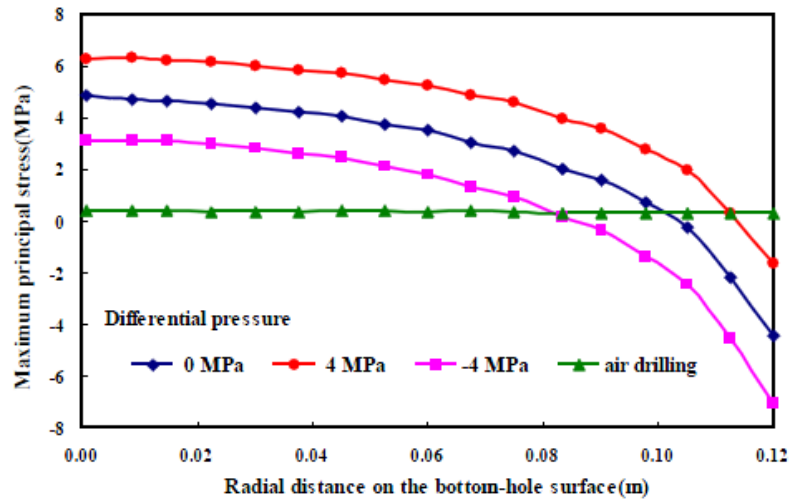
Figure 2.2 – Bottomhole surface maximum principal stresses along a radial
distance from the hole center (from Chang et al., 2012).

2.2 Thermal Effects on Wellbore Stresses

The thermoporoelasticity theory (Kurashige, 1989), a theoretical concept of the
thermoelastic theory for fluid-filled porous materials, fully couples relationships among
pore pressure, formation temperature, and solid matrix deformation. The model
incorporates heat transportation by pore-fluid flow inside the pore space and considers
the difference between the thermal expansibilities of the pore fluid and the solid matrix.
This thermoporoelasticity theory is well known in the industry.

A transient analytical solution (Wang et al., 1996) was derived for a case that had
an isotropic in-situ stress, constant temperature, and constant pore pressure at a wellbore
in low-permeability porous media but only considered conductive heat transfer in the
formation. When the formation was heated, the compressive effective tangential stress
increased and reached the maximum at the wellbore wall. This effect enhanced the

12

fracture gradient but made the wellbore less stable against compression. The cooling effect reduced the tangential stress and had its maximum value inside the formation. This change of the tangential stress elevated borehole instability but also reduced fracture gradient.

An analytical thermoporoelastic solution using the Mohr-Coulomb criterion showed a significant difference between thermoporoelastic and thermoelastic predictions because thermoelastic theory alone does not account for the pore-pressure change from the thermal effect (Li et al., 1999). The thermal effects were more pronounced in a low-permeability formation. Moreover, heating the wellbore increased the instantaneous wellbore shear failure, whereas cooling the wellbore raised a potential of instantaneous wellbore fracturing and could lead to a time-delayed shear failure.

The axisymmetric finite-element method has shown that the thermoelastic effects in a high temperature environment area are pronounced up to 5 times the well's radius. (Falcao, 2001). The effects of heating tend to improve the wellbore stability, and the thermoelastic effect grows with time.

In deepwater drilling, leakoff tests (LOTs) performed under various drilling fluid temperatures have shown an increase in the formation fracture resistance. Gonzalez et al. (2004) showed a strong correlation between LOT data and drilling fluid temperature: higher temperature conditions raise the effective fracture gradient, whereas lower temperatures reduce the effective fracture gradient. Thus, temperature profiles of drilling fluids in the wellbore help establish an idea of how to optimize drilling parameters such that the thermal impacts on the wellbore are favorable to the operations' objectives.

13

An analytical stress solution for the thermoporoelastic effects at the wellbore wall for wells with injection and production activities in the Laplace domain decoupled pore pressure from temperature (Chen and Ewy, 2004). The approach derives its complete solution from the superposition of three separate analytical solutions: hydraulic induced stress, thermal induced stress, and geometry induced stress (Figure 2.3).
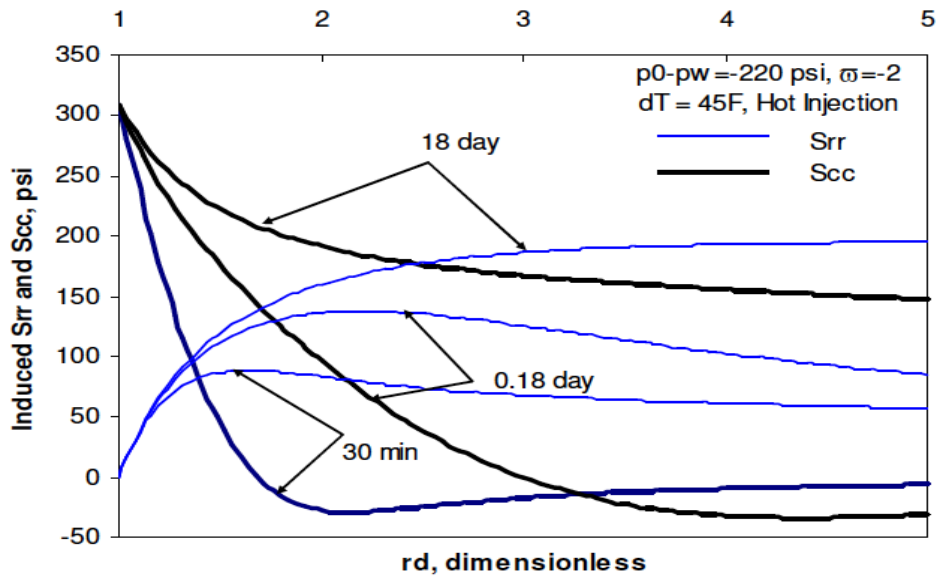
Figure 2.3 – Induced radial and tangential stresses for a hot injection
Swell for k = 1md and T_w-T_f = -45°F (from Chen and Ewy, 2004).

Downhole pressure data during the lost-circulation incidents in wells drilled through cooled formations have revealed significant reduction in the wellbore breakdown pressure, whereas offset wells located further away have given full returns. Hettema et al.'s (2004) thermoelastic model results showed much stronger effects than

their real case, possibly because the model did not include the thermo-poro effect, which caused a reduction in pore pressure in addition to the contraction of the rock matrix.

Cooling formations results in a more stable wellbore but makes the formation more vulnerable to fracture (Farahani et al., 2006; Zhai et al. 2009). Wellbore heating leads to the opposite results, in that it increases fracture resistance but caused the wellbore to be less stable (Figure 2.4).
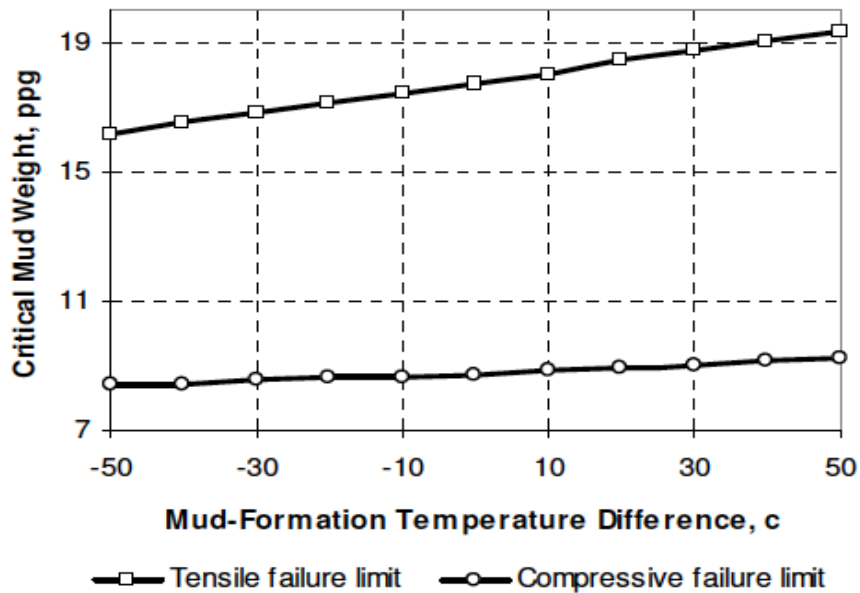
Figure 2.4 – Effects of temperature on critical mud weight selection
for a vertical wellbore (from Farahani et al., 2006).

Farahani et al.'s calculations for high-permeability formations included heat convection but decoupled rock-matrix deformation from the pressure-diffusivity equation. They solved the coupled problem of temperature and pore pressure with the

finite-difference method and substituted the solution into an integral analytical solution of thermoporoelastic stresses, using the tensile and Drucker-Prager failure criteria to evaluate impacts on rock stability at the wellbore wall.

Zhai et al. (2009) confirmed those findings for low-permeability formations with superposition of three separate solutions—stresses induced by a pore-pressure gradient, stresses induced by a temperature gradient, and stresses induced by an in-situ boundary—in shale formations. Their work showed that the thermally induced poro-elastic stress imposes large effects on low-mobility formations, especially at the early time, whereas pressure differential plays an important role in high-mobility formations (Figure 2.5).
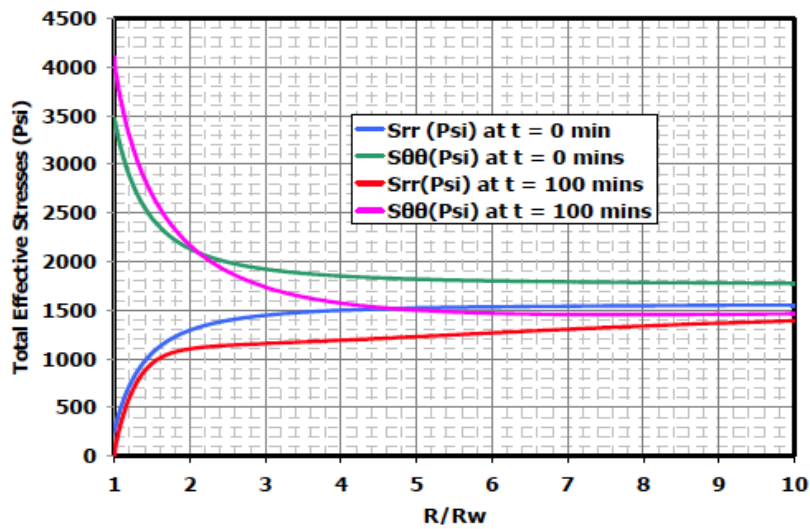
Figure 2.5 – Total effective stresses at the wellbore wall for
T_w-T_f = 57°F at 100 minutes (from Zhai et al., 2009).

Furthermore, cool-water injection causes formation damage that induces stress variation and a discontinuous pore pressure (Lee and Ghassemi, 2010). This pore-pressure discontinuity impacts the total stress around the wellbore, and distributed shear and tensile failures propagate into the reservoir as time increases.

However, the influences of temperature on mechanical properties of the shale are nonlinear and depend on confining pressure, temperature, and loading orientation (Masri et al. 2009). Figure 2.6 shows deviatoric stresses at failures in which a loading direction is perpendicular to the sample's bedding plane at different temperatures.
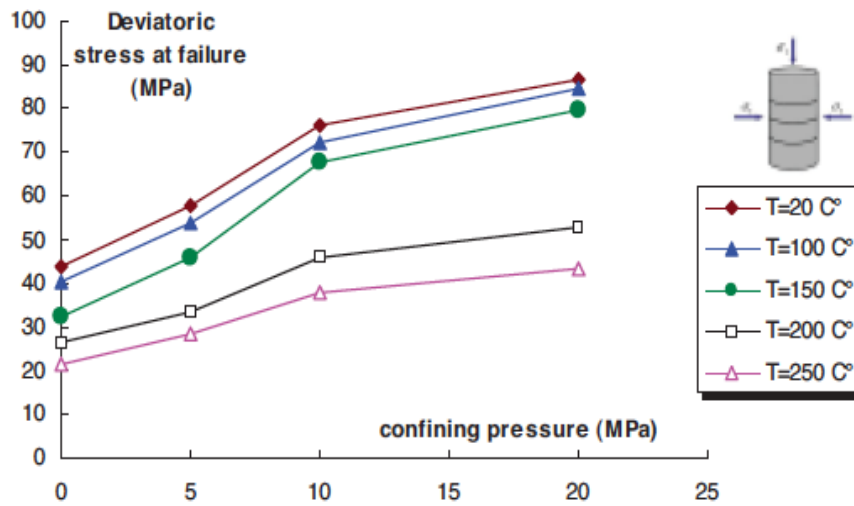
Figure 2.6 – Experimental results of deviatoric stresses at failure
under various controlled temperatures (from Masri et al., 2009).

Most assumptions as late as 2010 underpredicted drilling-fluid temperature, especially in directional wells. Nguyen et al. (2010) developed a model that enhances

predictions and revealed that the heat transfer at the wellbore wall causes noticeable effects on the formation and drilling fluid temperatures.

Cooling the wellbore reduces the local radial and tangential stresses in the near-wellbore region with nonisotropic in-situ stresses. Although the temperature change induced by fluid diffusion is small and negligible in low-permeability formations, the thermal impact on the tangential stress is significant and time independent (Wu et al., 2010 and 2011). This tangential stress reduction causes the wellbore fracture resistance to decrease.

On the other hand, heating a formation leads to increases in pore pressure and tangential stress toward compression Tao and Ghassemi (2010). As exposure time increases, the peak of the induced pore pressure is reduced and moves away from the wellbore, and the magnitude of the induced tangential stress decreased and changed its sign at some point (Figure 2.7). This tensile effect diminishes at late time owing to the thermal and hydraulic diffusions.

Because of different permeability and bulk modulus between shale and granite, a thermoporoelastic solution shows that their induced stress at the wellbore wall behaves differently. The induced stress for granite (Figure 2.8) reveals that heating increases the effective tangential stress and reduces the effective radial stress; thus, potentials of compressive failure and radial spalling at the wellbore are increased. Cooling causes reverse effects, which are reduction of the effective tangential stress and increase of the effective radial stress. The results on wellbore stability are enhancement of hydraulic fracturing, and prevention of the radial spalling.
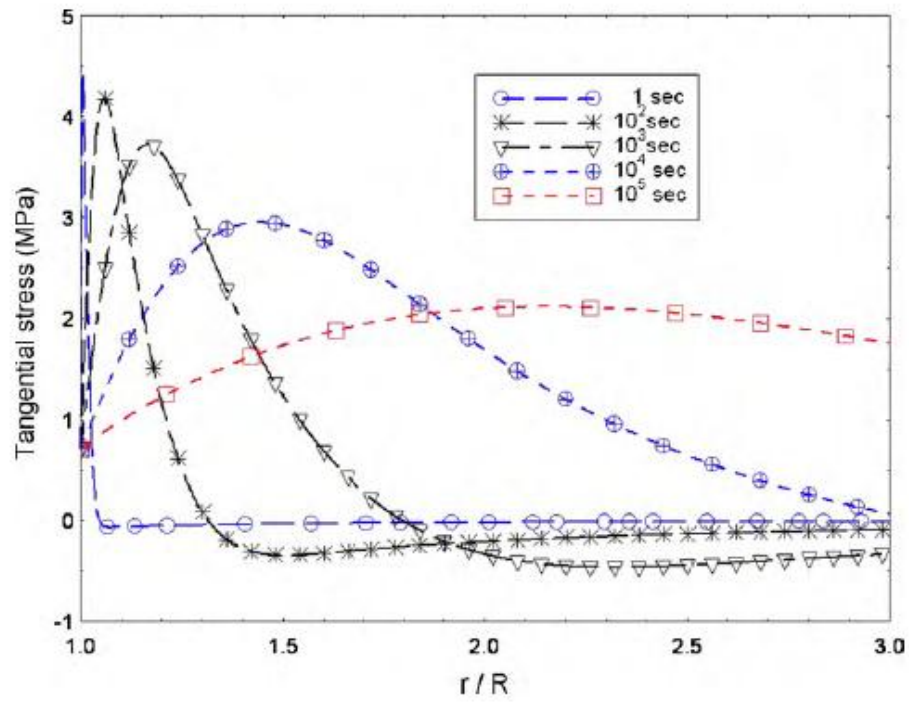
Figure 2.7 – Heating induced tangential stress for shale (from Tao and Ghassemi, 2010).
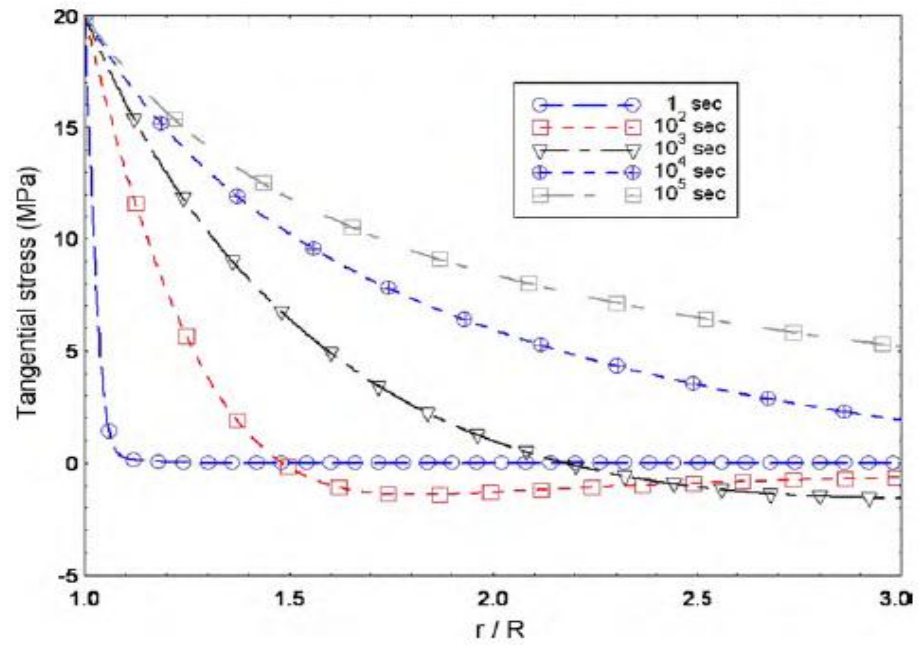
Figure 2.8 – Heating induced tangential stress for
granite (from Tao and Ghassemi, 2010).

19

In chemically active formations, heating and/or lower mud salinity lead to increase in pore pressure, making the total radial and tangential stresses more compressive, and cooling and/or higher mud salinity have the opposite effects, decreasing pore pressure and increasing the total radial and total tangential stresses (Diek et al. 2011). A case with a lower fluid diffusivity (permeability-fluid viscosity ratio) leads to larger effects of thermal and chemical loading (Figures 2.9 and 2.10)
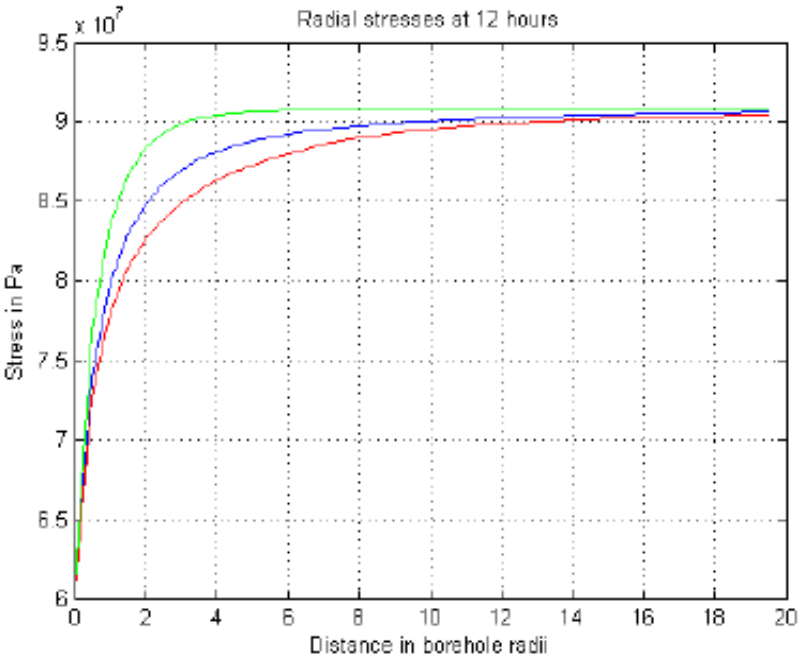
Figure 2.9 - Total radial stresses along radial distance from the wellbore wall for isothermal, heating, and cooling cases (from Diek et al., 2011).
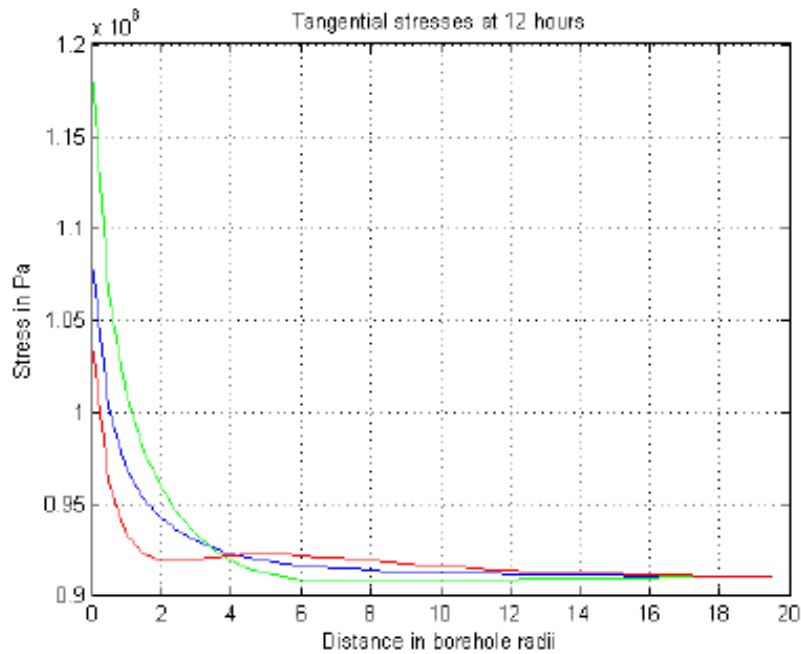
Figure 2.10 - Total tangential stresses along radial distance from the wellbore
wall for isothermal, heating, and cooling cases (from Diek et al., 2011).

2.3 Rock Failure and Bit-Rock Drilling Mechanisms

When Paul and Gangal (1969) observed a splitting–type failure of rock underneath the point of a bit tooth, they identified a limitation of the classical Flamant's solution in predicting a stress solution. Their observation implied large tension stress, whereas the solution from Flamant's model shows only compression in the rock. Paul and Gangal (1969) proposed a new geometry of a stress boundary created by a bit tooth (Figure 2.11) and solved the stress solution using the finite-element method. Their results show the presence of tensile stresses directly underneath the bit (Figure 2.12).
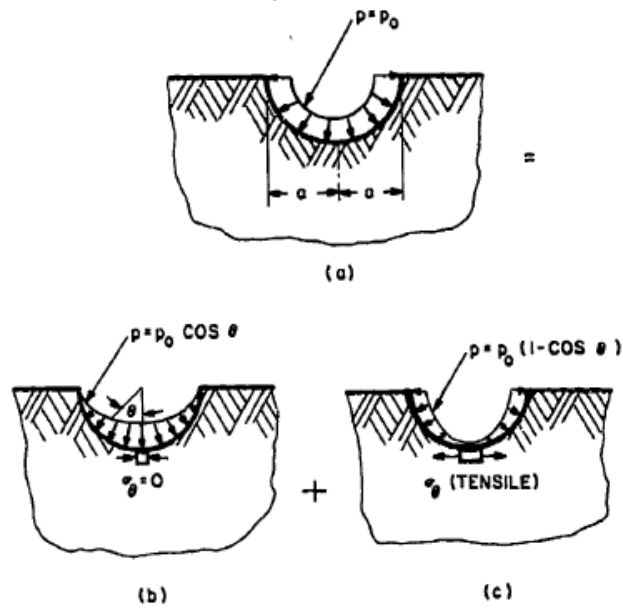
Figure 2.11 – (a) Stress boundary condition in Paual and Grangal's model; (b) Flamant's boundary condition; (c) Difference between (a) and (b). (From Paul and Gangal, 1969)
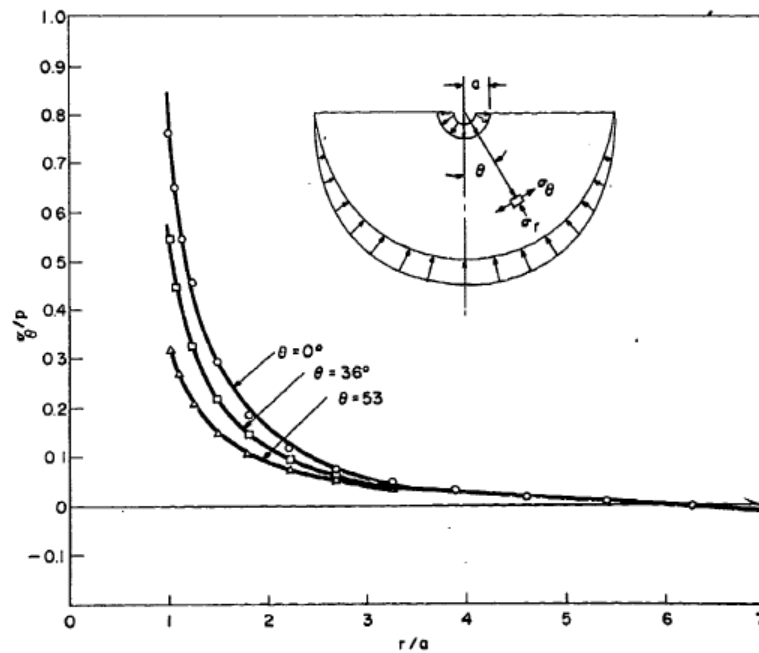
Figure 2.12 – Tensile stresses under the bit tooth (from Paul and Gangal, 1969).

Zhao and Roegiers (1995) proposed an analytical method for predicting drilling performance and estimating rock mass fracture properties, focusing on the bit-tooth indentation. They found that the elastic model agrees with the drilling performance data at low confined pressures, whereas the elasto-plastic model fits the data at high confined pressures. Moreover, they found that the contact stresses on the formation are independent from confined pressures.

Sun (2001) introduced a new interaction model of rock/bit interaction for the rotary tri-cone bit. The model assumes four stages of bit tooth attacking the rock surface—initial contact, indentation, gouging, and bit departure—and accounts for the loading history affecting rock fracture process. Sun's mixed-mode fracture development was based on strain energy (proposed by Sih in 1991) and describes a crack developing under the influence of tensile and shear stresses.

Both shear and tensile failures concentrate at the bottom of a drill hole in the normal stress regime, whereas both failures locate mainly along the sides of a drill hole in the tectonic stress regime (Zhang and Roegiers, 2005). Modeling shear and tensile failure modes from indentation in two in-situ stress regimes (normal and tectonic) has shown that more weight on bit would be required to make a hole in a tectonic stress regime area, and failure potential is higher in a dual-porosity medium than in a single-porosity one.

Nygaard and Hareland (2007) developed a rock-strength log to be used with ROP models to predict drilling time, bit wear, and optimum drilling parameters without

accounting for geological variability. Their correlation centered on rate of penetration and unconfined compressive strength of the rock.

Using polyaxial compressive-strength test-results and the modified Drucker-Prager criterion gives more accurate failure predictions than the Drucker-Prager criterion and triaxial results (Gadde and Rusnak 2008). Models of laboratory tests showed that the conventional Drucker-Prager criterion overestimates failure.

Tangential (torque) and vertical forces (thrust) are very dynamic contributors to the cutter/rock mechanism, and the thrust forces clearly increase with the cutting depth. Bilgesu et al. (2008) developed a FRAC 3D model that contained a velocity boundary condition representing a constant rate of penetration and a rotational boundary representing a constant bit rotation. The ultra-deep single-cutter drilling simulation (UDS) set up in their laboratory was used to calibrate and validate the FRAC 3D model. The cutter moved through the rock until failure occurred, and the stress levels on the cutter were dropped. Then the cutter started to stress the next element, causing the stresses to rise again until the rock failed. This stress cycle was repeated in rock cutting tests for both sandstone and shale.

Intermediate principal stress has a noticeable impact on rock strength: under the same mean stress, polyaxial compressive strengths are lower than triaxial shear strengths (Figure 2.13) and this effect is more pronounced at a higher σ_2/σ_3 ratio (Thosuwan et al., 2009). Furthermore, shear failure dominates at a low σ_2/σ_3 ratio, whereas splitting tensile fracture is more evident at a high σ_2/σ_3 ratio.
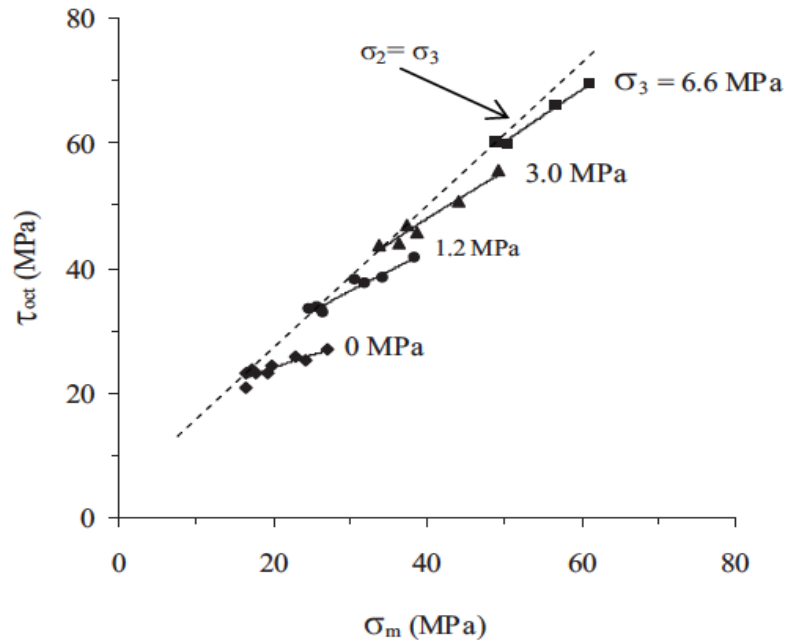
Figure 2.13 – Octahedral shear stress as a function of mean stress from polyaxial tests of sandstone samples (from Thosuwan et al., 2009).

Both tensile and shear rock failures occur inside the rock ahead of and below the cutter face, so the confining stress and mud pressure need to be increased when weight-on-bit increases to maintain a constant depth-of-cut (Block and Jin, 2009). Chip-like cuttings, which are predominant in a state of brittle failure, are found in a low weight-on-bit and low confining pressure situations. Ribbon-like cuttings, which are predominant in a state of ductile failure, are found in a high weight-on-bit and high confining pressure situation.

Among popular failure criteria—the Mohr-Coulomb, the modified Lade, and two versions of the Drucker-Prager—the Mohr-Coulomb and the inscribed Drucker-Prager failure criteria are conservative by predicting higher wellbore collapse pressures in

25

sandstone than other criteria (Nawrocki, 2010). Nawrocki found that the circumscribed Drucker-Prager criteria, on the other hand, provided optimistic predictions. The linear model overestimated critical well pressure comparing to nonlinear one.

2.4 Fourier-Assisted Finite-Element Method

Wang and Wong (1987) presented an application of the Fourier-assisted finite-element method in evaluating a coring operation for a model that had anisotropic in-situ stresses at the far-field boundaries. They developed a two-dimensional axisymmetric system at the coring location to solve for a three-dimensional displacement solution inside the core sample. Their work described a scheme to implement the Fourier series with the finite-element method; since constant-boundary stresses in Cartesian coordinates can be transformed into the Fourier series boundary stresses in the cylindrical coordinates, they attained a reduction from three to two dimensions, using a superposition on the solution of each Fourier harmonic complete solution of the problem.

CHAPTER III

FUNDAMENTAL CONCEPTS IN GEOMECHANICS

Most materials possess abilities to withstand external loading forces. The result is a material deformation which depends on a direction and a magnitude of the force imposed on the material. The deformation can be classified into elasticity, plasticity, and failure (fall apart) based on loads and material properties. Most rocks found in drilling operation behave like nonlinear elastic materials or elastic-plastic materials, which require a complex rock constitutive model. Many researchers have conducted their studies under the linear-elastic rock model because of its simplicity. Though the linear elastic model presents some errors in describing rock behaviors, it offers good preliminary results that, in many cases, are sufficient to represent problems of interest.

The linear elasticity theory describes a material that has linear relationships between external stresses and corresponding deformations acting on the body. When the external stress disappears, the material recovers its original shape. The linear elastic behavior usually occurs when rocks experience a small load. As the load increases, it tends to become nonlinear elastic or plastic.

The poroelasticity theory was developed for isothermal porous media by incorporating the effective stress and pore pressure concepts into the elasticity model. The poroelasticity theory describes coupled effects between stress and strain in solid matrix and pore pressure diffusion. Because rocks are porous, this theory has been used

to study their hydro-mechanical interaction and found to give reasonable results. In this thesis, the rocks were assumed to be fully saturated with a single-phase fluid.

Effects of temperature in elastic material are obtained by the thermoelasticity theory, which includes the thermal strain into the constitutive stress-strain relation of elasticity theory. The thermoelasticity model predicts thermal responses of an elastic material in the presence of a temperature gradient or a change in temperature from the material's original state.

A more complicated model governing the thermal and pore pressure effects in porous media is the thermoporoelasticity theory. That model gives fully coupled relationships among displacement/stress, pore pressure, and temperature. The thermoporoelasticity theory will be presented in Chapter 4. The poroelasticity and thermoelasticity theories will be introduced in this chapter without details.

3.1 Stress and Strain

The key concepts of geomechanics are stress, strain, and their relationship. The stress defines load acting on the body and the strain defines a deformation according to the load applied. The direction of stress is conceptual and based on the plane of interest, which could be imaginary or a real plane. The magnitude of stress varies from one plane to another and can be found using the concept of stress transformation in space.

3.1.1 Definitions of Stress and Strain

In general, stress is defined as a unit force acting on an area which could be either a physical plane or an imaginary plane. Stress is a vector that possesses a magnitude and a direction. For geomechanic problems, a positive stress represents compression, whereas negative stress represents tension.

There are two types of stress: normal stress, and shear stress. Normal stress is defined as a unit force acting normal to a plane, and shear stress is unit force acting parallel to a plane (Figure 3.1).
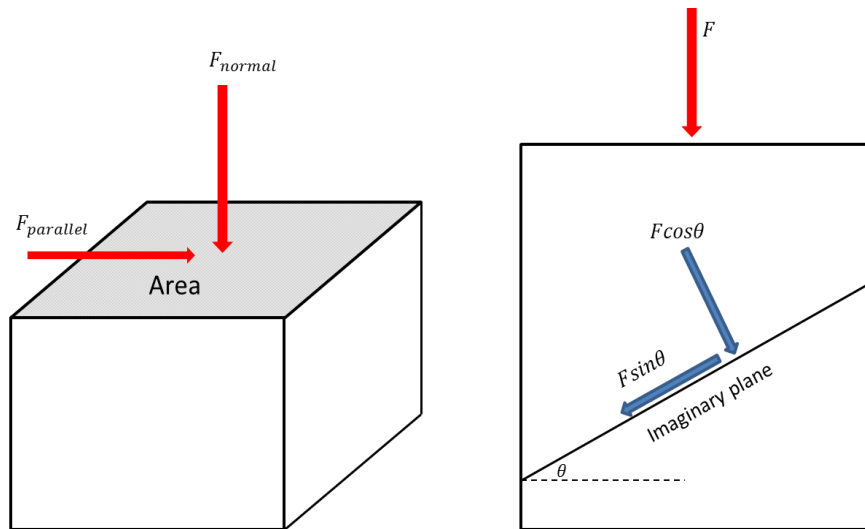
Figure 3.1 – Diagram shows definitions of normal stress
and shear stress in arbitrary plane.

Normal Stress:

$$\sigma = \frac{F_{\text{normal}}}{\text{Area}} = \frac{F\cos\theta}{\text{Area}} \qquad (3.1)$$

Shear Stress:

$$\tau = \frac{F_{\text{parallel}}}{\text{Area}} = \frac{F \sin\theta}{\text{Area}} \tag{3.2}$$

Strain is defined as a ratio of a deformation in terms of displacement when a body is subjected to external loads. Strain carries the same sign and direction as the stress that associates with it. Thus, in this thesis, positive strain means compressive deformation and negative strain means tensile deformation. In a small deformation, which is generally valid for rock deformations found in drilling operations, strain is expressed by

$$\epsilon = \frac{\Delta l}{l} \tag{3.3}$$

3.1.2 Stress and Strain Components in Three Dimensions

In the three dimensions, nine different components of stress represent a stress state. The nine stress components in the Cartesian coordinates are shown in Figure 3.2, and all stresses are presented in positive directions (compressive).
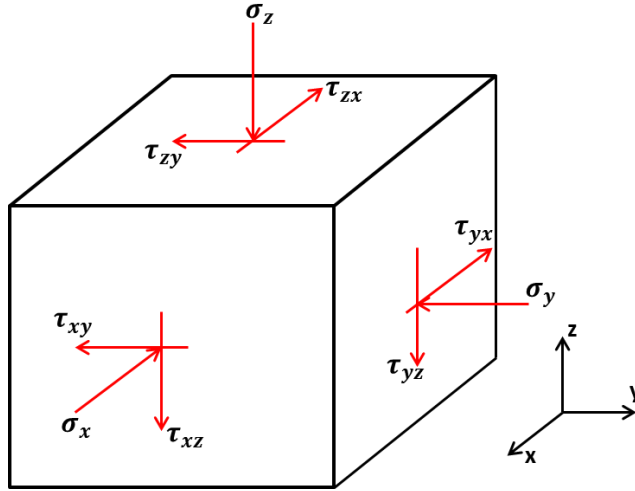
Figure 3.2 – Positive stress components in the 3-dimensional Cartesian coordinates.

For elements in the equilibrium state, nine different stress components in three dimensions reduce to six independent components. The derivation can be found in most geomechanics textbooks. This stress component simplification leads to a stress tensor or a stress matrix with the six independent components as shown in Eq. 3.4.

$$\langle \sigma \rangle = \begin{bmatrix} \sigma_x & \tau_{xy} & \tau_{xz} \\ \tau_{xy} & \sigma_y & \tau_{yz} \\ \tau_{xz} & \tau_{yz} & \sigma_z \end{bmatrix} \quad or \quad [\sigma] = \begin{bmatrix} \sigma_x \\ \sigma_y \\ \sigma_z \\ \tau_{xy} \\ \tau_{yz} \\ \tau_{xz} \end{bmatrix} \tag{3.4}$$

Similar to the stress components, a three-dimensional strain state under the equilibrium condition can be presented as

$$\langle \epsilon \rangle = \begin{bmatrix} \epsilon_x & \gamma_{xy} & \gamma_{xz} \\ \gamma_{xy} & \epsilon_y & \gamma_{yz} \\ \gamma_{xz} & \gamma_{yz} & \epsilon_z \end{bmatrix} \quad or \quad [\sigma] = \begin{bmatrix} \epsilon_x \\ \epsilon_y \\ \epsilon_z \\ \gamma_{xy} \\ \gamma_{yz} \\ \gamma_{xz} \end{bmatrix} \tag{3.5}$$

The trace of the strain tensor is known as a volumetric strain, which represents a ratio of a volume change to the original volume. By this definition, the volumetric strain is

$$\epsilon_{vol} = \frac{\Delta \epsilon_{vol}}{\epsilon_{0,vol}} = \epsilon_x + \epsilon_y + \epsilon_z \tag{3.6}$$

A description of a strain state as defined by Eq. 3.3 at a point within a 3D infinitesimal body is described by six strain components.

$$\epsilon_x = \frac{\partial u_x}{\partial x} \tag{3.7}$$

$$\epsilon_y = \frac{\partial u_y}{\partial y} \tag{3.8}$$

$$\epsilon_z = \frac{\partial u_z}{\partial z} \tag{3.9}$$

$$\gamma_{xy} = 2\epsilon_{xy} = \frac{\partial u_x}{\partial y} + \frac{\partial u_y}{\partial x} \tag{3.10}$$

$$\gamma_{yz} = 2\epsilon_{yz} = \frac{\partial u_y}{\partial z} + \frac{\partial u_z}{\partial y} \tag{3.11}$$

$$\gamma_{xz} = 2\epsilon_{xz} = \frac{\partial u_x}{\partial z} + \frac{\partial u_z}{\partial x} \tag{3.12}$$

Eqs. 3.7 to 3.9 are normal strain components governing a change of an element volume due to the hydrostatic stress, whereas the shear strains in Eqs. 3.10 to 3.12 result in a shape change due to the deviatoric stress.

In well drilling, it is convenient to use the cylindrical coordinates instead of the Cartesian system. The six components of strain defined in the cylindrical coordinates similar to Eqs. 3.7 to 3.12 can be found in most geomechanics textbooks.

3.1.3 Coordinates Transformation of Stress and Strain

When dealing with a geomechanics problem, an engineer usually comes across a stress or a strain transformation from one axis to another. This transformation is derived from a force balance; therefore, both stress and area transformations have to be considered in the formula.
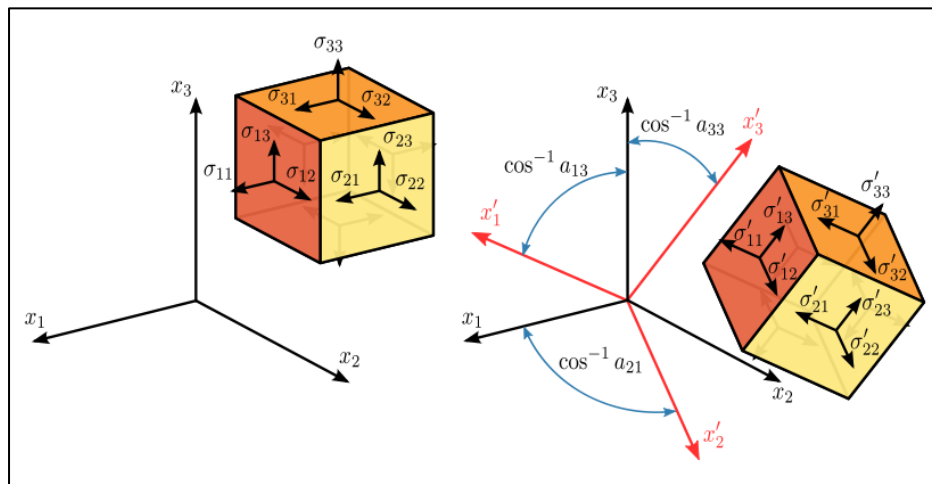
Figure 3.3 – Stress transformation in 3-dimensions from
$x_1 - x_2 - x_3$ axes to $x'_1 - x'_2 - x'_3$ axes.

Figure.3.3 represents a stress transformation in a 3D space. The transformation formula from x_1-x_2-x_3 coordinates to x'_1-x'_2-x'_3 coordinates is presented in Eq. 3.13, which can be derived by using the area transformation and Cauchy's transformation law.

$$\langle \sigma' \rangle = [T]\langle \sigma \rangle[T]^T \tag{3.13}$$

where

$$\langle \sigma' \rangle = \begin{bmatrix} \sigma'_{11} & \sigma'_{12} & \sigma'_{13} \\ \sigma'_{12} & \sigma'_{22} & \sigma'_{23} \\ \sigma'_{13} & \sigma'_{23} & \sigma'_{33} \end{bmatrix} \qquad (3.14)$$

$$[T] = \begin{bmatrix} cos(a_{11}) & cos(a_{12}) & cos(a_{31}) \\ cos(a_{21}) & cos(a_{22}) & cos(a_{23}) \\ cos(a_{31}) & cos(a_{32}) & cos(a_{33}) \end{bmatrix} \qquad (3.15)$$

The transformation in space for strain can be achieved in a similar manner as Eq. 3.13 by using the same transformation matrix, Eq. 3.15, and replacing the stress tensor, Eq. 3.14, with the strain tensor.

For a special case of stress in two dimensions, the use of a Mohr's circle provides a graphical way to transform stresses into other orientations.

3.1.4 Principal Stresses and Principal Strains

For certain orientations of a coordinates system, the transformation of stresses presents only the normal stresses (shear stresses are zero). If this condition is met, the normal stresses are referred to as principal stresses. The three principal stresses in 3D models are the maximum, intermediate, and minimum principal stresses following the order of their magnitudes. In this thesis, the maximum principal stress represents the highest compressive stress.

An advantage of principal stresses is to help avoid confusion in expressing a stress state. The stress-transformation concept allows one stress state to be described in many different way based on an orientation of a selected coordinates system. Referring a stress state with principal stresses eliminate this problem.

An example of the principal stresses and the principal orientation of a 2D stress state is presented in Figure 3.4. Assuming that stresses σ_1 and σ_2 are acting on the body as shown, the planes perpendicular to those stresses give zero shear stresses. Thus, σ_1 and σ_2 are the principal stresses and are represented on a Mohr's circle on the σ axis. At an arbitrary angle, θ, from the σ_1-plane (perpendicular to the direction of σ_1), stress transformation gives nonzero shear stresses; therefore, the transformed normal stresses are not the principal stresses.
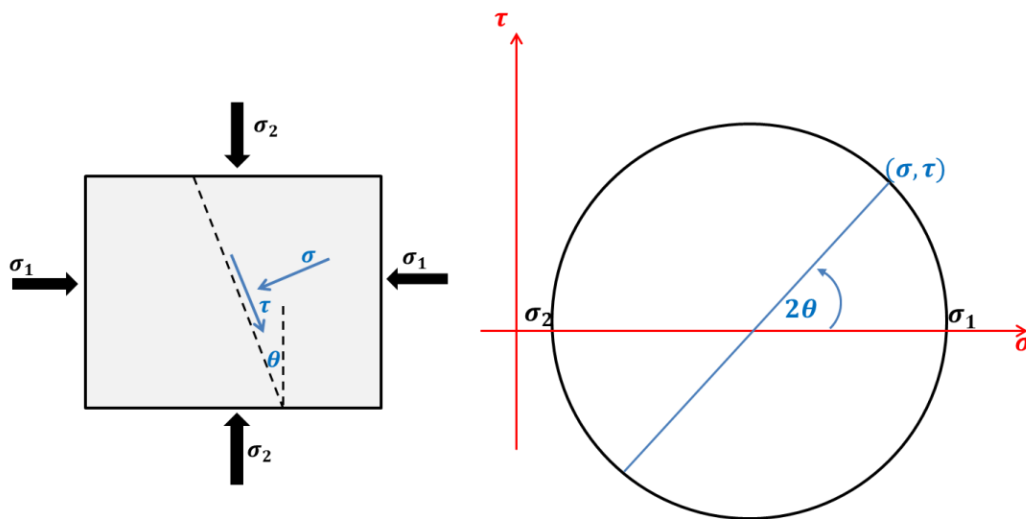
Figure 3.4 – Principal stresses in two dimensions and their representation on a Mohr's circle.

To solve for principal stresses in a 3D stress state, the stress is presented in the form of a stress tensor, $\langle\sigma\rangle$, as given in Eq. 3.4. The principle stresses can be found from the solutions of a cubic equation:

$$\sigma^3 - I_1\sigma^2 - I_2\sigma - I_3 = 0 \tag{3.16}$$

where

$$I_1 = \sigma_x + \sigma_y + \sigma_z$$

$$I_2 = \tau_{xy}^2 + \tau_{xz}^2 + \tau_{yz}^2 - \sigma_x\sigma_y - \sigma_x\sigma_z - \sigma_y\sigma_z \tag{3.17}$$

$$I_3 = \sigma_x\sigma_y\sigma_z + 2\tau_{xy}\tau_{yz}\tau_{xz} - \sigma_x\tau_{yz}^2 - \sigma_y\tau_{xz}^2 - \sigma_z\tau_{xy}^2$$

Eq. 3.16 gives three real roots, which are principal stresses. They are presented by σ_1, σ_2 and σ_3 where $\sigma_1 > \sigma_2 > \sigma_3$. The three solutions from Eq. 3.16 are sometimes referred to as the eigenvalues of the stress tensor. I_1, I_2 and I_3 are known as stress invariants and are independent of coordinate axes.

Principal strains are similar to principal stress. The method to solve for principal strains is analogous to principal stresses as shown in Eqs. 3.16 and 3.17.

3.1.5 Average Normal Stress and Deviatoric Stress

A stress state can be decomposed into two independent stress modes, average normal stress and deviatoric stress, based on their effects on the element body. The average normal stress causes a change in element volume under uniform compression or extension. The deviatoric stress causes a shape change or distortion on an element body.

The average normal stress is defined as

$$\sigma_m = \frac{1}{3}(\sigma_x + \sigma_y + \sigma_z) \tag{3.18}$$

The decomposition of the stress tensor into average normal stress and deviatoric stress is shown below:

$$\begin{bmatrix} \sigma_x & \tau_{xy} & \tau_{xz} \\ \tau_{xy} & \sigma_y & \tau_{yz} \\ \tau_{xz} & \tau_{yz} & \sigma_z \end{bmatrix} = \begin{bmatrix} \sigma_m & 0 & 0 \\ 0 & \sigma_m & 0 \\ 0 & 0 & \sigma_m \end{bmatrix} + \begin{bmatrix} (\sigma_x - \sigma_m) & \tau_{xy} & \tau_{xz} \\ \tau_{xy} & (\sigma_y - \sigma_m) & \tau_{yz} \\ \tau_{xz} & \tau_{yz} & (\sigma_z - \sigma_m) \end{bmatrix} \quad (3.19)$$

Deviatoric stress is the second term on the right-hand side. Similar to the stress invariants, the deviatoric stress has the same invariants properties, which are J_1, J_2, and J_3.

$$J_1 = 0$$

$$J_2 = \frac{1}{6}[(\sigma_1 - \sigma_2)^2 + (\sigma_2 - \sigma_3)^2 + (\sigma_1 - \sigma_3)^2] \quad (3.20)$$

$$J_3 = I_3 + \frac{1}{3}I_1 I_2 + \frac{2}{27}I_1^3$$

By splitting stress into these two components, it benefits an analysis of compressive failure. Many shear failure criteria refer to the average normal stress as confining stress, and the second deviatoric invariant as the shear or deviatoric stress that causes failure.

3.2 Theory of Linear Elasticity

The theory of elasticity governs material deformation in which there are linear relationships between applied stresses and resulting strains. This type of response is usually found when small loads are applied on rocks.

Considering a case in which a sample experiencing equal loads is applied at both its ends. Following the elasticity theory, resulting strains corresponding to applied stresses are linear and plotted in Figure 3.5. Note that positive stresses and strains in Figure 3.5 represent compression.

A linear relationship between normal stress and normal strain as shown in Figure 3.5 is governed by Hooke's law of deformation:

$$\sigma_y = E\epsilon_y \tag{3.21}$$

The slope in Figure 3.5 or coefficient E is known as the Young's modulus or the modulus of elasticity, which is the crucial material property in a rock-mechanic study. Young's modulus represents a material resistance to deformation under stress. With a similar load condition, materials with higher Young's modulus experience less deformation.

Another result of applied stress is transverse strain, which may occur in the sample as seen in Figure 3.5. The ratio of transverse strain to axial strain is described by Poisson's ratio, which is defined as a negative ratio of transverse strain to axial strain.

$$\nu = -\frac{\epsilon_x}{\epsilon_y} \tag{3.22}$$

The negative sign in Eq. 3.22 indicates that the transversal effect produces the transverse strain, which has an opposite compressive-tensile sign to the axial strain.

Similar to Eq. 3.21, the relationship between shear stress and shear strain in the linear elasticity theory can be described as

$$\tau = G\gamma \tag{3.23}$$

where τ is the engineering shear stress, G is shear modulus, and γ is the shear strain.

The shear modulus G is related to the Young's modulus E by

$$G = \frac{E}{2(1 + \nu)} \tag{3.24}$$
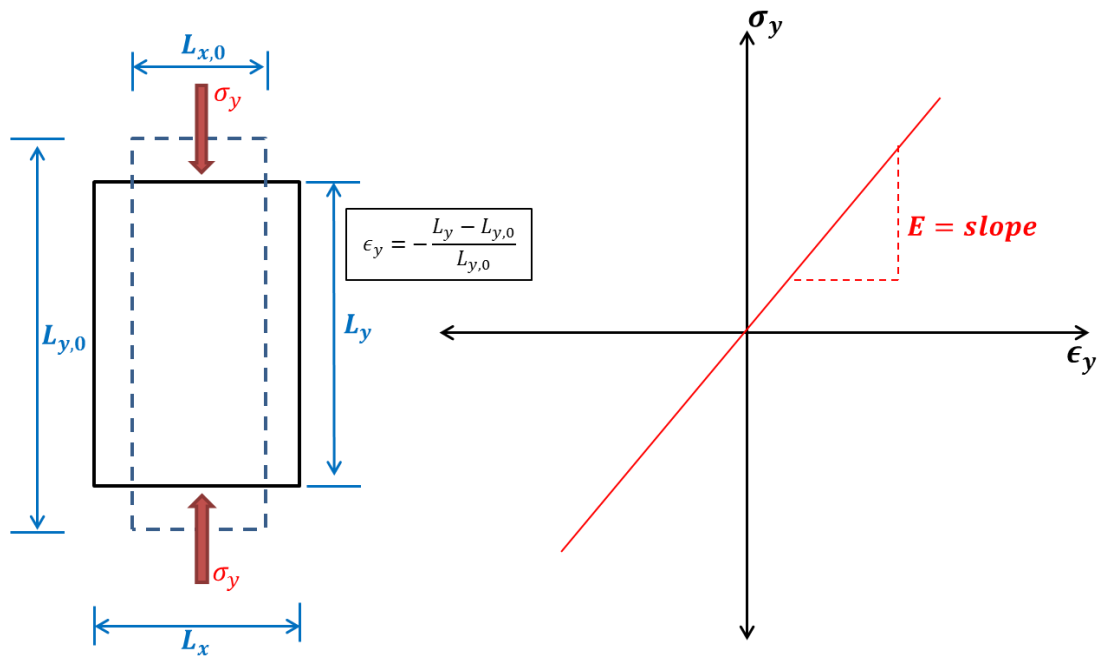
Figure 3.5 – Unconfined stress-strain plot and its diagram shows
stress-strain directions of linear elastic materials under vertical loads.

The relation of stress and strain given in Eq. 3.21 is valid only for an element under one-dimensional loading. The more general relations between stresses and strains under polyaxial loading can be presented in term of matrices as given in Eq. 3.25:

$$\begin{bmatrix} \epsilon_x \\ \epsilon_y \\ \epsilon_z \\ \gamma_{xy} \\ \gamma_{yz} \\ \gamma_{xz} \end{bmatrix} = \frac{1}{E} \begin{bmatrix} 1 & -\nu & -\nu & 0 & 0 & 0 \\ -\nu & 1 & -\nu & 0 & 0 & 0 \\ -\nu & -\nu & 1 & 0 & 0 & 0 \\ 0 & 0 & 0 & 2(1+\nu) & 0 & 0 \\ 0 & 0 & 0 & 0 & 2(1+\nu) & 0 \\ 0 & 0 & 0 & 0 & 0 & 2(1+\nu) \end{bmatrix} \begin{bmatrix} \sigma_x \\ \sigma_y \\ \sigma_z \\ \tau_{xy} \\ \tau_{yz} \\ \tau_{xz} \end{bmatrix} \qquad (3.25)$$

Eq. 3.25 can be re-stated in an alternative form expressing stresses as functions of strains.

$$\begin{bmatrix} \sigma_x \\ \sigma_y \\ \sigma_z \\ \tau_{xy} \\ \tau_{yz} \\ \tau_{xz} \end{bmatrix} = A \begin{bmatrix} 1-v & v & v & 0 & 0 & 0 \\ v & 1-v & -v & 0 & 0 & 0 \\ v & v & 1-v & 0 & 0 & 0 \\ 0 & 0 & 0 & \dfrac{(1-2v)}{2} & 0 & 0 \\ 0 & 0 & 0 & 0 & \dfrac{(1-2v)}{2} & 0 \\ 0 & 0 & 0 & 0 & 0 & \dfrac{(1-2v)}{2} \end{bmatrix} \begin{bmatrix} \epsilon_x \\ \epsilon_y \\ \epsilon_z \\ \gamma_{xy} \\ \gamma_{yz} \\ \gamma_{xz} \end{bmatrix} \tag{3.26}$$

where

$$A = \frac{E}{(1+v)(1-2v)}$$

3.3 Theory of Poroelasticity

The elasticity theory treats materials of interest as if they are homogeneous. Because rocks are porous materials, the elasticity theory does not well describe rocks' behaviors especially rock failure phenomena. To represent true physics of porous media such as rocks, the elastic model needs to incorporate the pore-fluid, pressure-flow, and effective-stress concepts as presented by Tarzaghi (1943).

The concept of effective stress can be explained using a two-spring diagram (Figure 3.6). When total stress is applied to porous material, pore pressure and stress in the solid rock matrix, known as effective stress, help support this loading. When pore pressure is known, the effective stress can be found using Eq. 3.27.
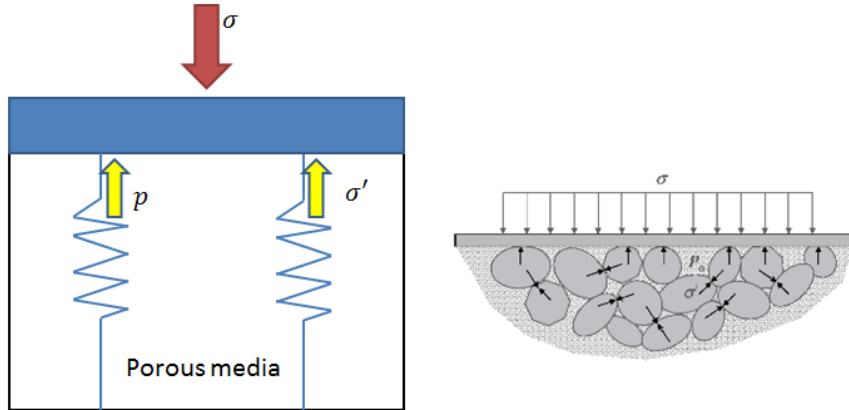
Figure 3.6 – Two-spring diagram representing the effective stress concept in porous media.

$$\sigma' = \sigma - \alpha p \qquad (3.27)$$

where σ' is effective stress, σ is total stress, α is the Biot's constant, and p is pore pressure.

Fluid inside the pore space can flow from one pore to another under the influence of pore pressure, which is governed by the pressure diffusivity equation and Darcy's law. Moreover, the solid matrix deformation corresponding to the magnitude of the effective stress causes a pore-volume change, which subsequently, leads to a pore-pressure change. This pore-pressure alteration then affects the magnitude of effective stress.

The physics of porous media is a coupled interaction between deformation under stress and pore fluid flow. The governing equations for fluid-saturated poroelastic materials are the pressure diffusivity equation, incorporating the deformation effect (Eq. 3.28), and the force balance law, incorporating the effective stress concept (Eq. 3.29).

$$\frac{\partial p}{\partial t} = \frac{2G(v_u - v)}{\alpha^2(1 - 2v)(1 - 2v_u)}\left[\frac{k}{\mu}\nabla^2 p + \alpha\frac{\partial \epsilon_{kk}}{\partial t}\right] \tag{3.28}$$

$$Gu_{i,jj} + \frac{G}{1 - 2v}u_{j,ij} + \alpha p_{,i} = 0 \tag{3.29}$$

3.4 Theory of Thermoelasticity

A temperature change produces thermal strain in a material body; cooling leads to contraction, heating leads to expansion. If the thermal deformation is restricted, a temperature change will result in a thermal stress.

A material property controlling degrees of thermal stress and thermal strain is the coefficient of linear/volumetric thermal expansion, which is commonly assumed to be independent of temperature. By using the coefficient of linear thermal expansion, thermal strain and thermal stress are presented in Eqs. 3.30 and 3.31.

$$\epsilon_{thermal} = -\alpha_m^{TL}\Delta T \tag{3.30}$$

$$\sigma_{thermal} = -E\epsilon_{thermal} = E\alpha_m^{TL}\Delta T \tag{3.31}$$

The constitutive relation for thermoelasticity theory can be obtained by incorporating thermal stress/strain into the constitutive relation of elasticity theory. The thermoelastic constitutive relation in terms of stresses as functions of strains is

$$\sigma_{ij} = 2G\left(\epsilon_{ij} + \frac{v}{1 - 2v}\epsilon_{kk}\delta_{ij}\right) + \frac{2G(1 + v)\alpha_m^{TL}}{(1 - 2v)}\Delta T\delta_{ij} \tag{3.32}$$

3.5 Rock Failure Criteria

Rocks fail when they cannot withstand large loads that exceed the strength of the rock. The failure process could undergo a plastic deformation such as in ductile materials, or show an instant destruction (break into pieces) after their yield limit is reached, such as in brittle materials. In this thesis, rock failure is assumed to be the latter mode, in which bonds between rock grains fall apart when the applied stresses reach a certain rock limit.

The two major failure modes in rocks are shear or compressive failure and tensile failure. The shear failure occurs when rock matrix experiences excessive compressive stresses; the tensile failure occurs when rock matrix experiences excessive tensile stresses.

At the wellbore wall, the shear failure mode describes the wellbore collapse, and the tensile failure mode describes the wellbore fracture. Failure criteria in both tensile and shear modes are used to predict mud-weight windows for drilling operations. At the bottom of the hole where a drill bit breaks the rocks, both drag and tooth bits result in a combined rock failure mechanism at the bit/formation interface (Paul and Gangal, 1969; Block and Jin, 2009). This implies that the compressive and tensile failure criteria need to be considered to predict drillability of the bottomhole formation.

3.5.1 Shear Failure Criterion: Drucker-Prager Criterion

The Drucker-Prager failure criterion was used to evaluate rock compressive stability/failure in this thesis. This failure criterion is an extended version of the Von

Mises criterion. Both criteria consider effects from all the principal stresses, which are the maximum, intermediate, and minimum effective principal stresses, unlike the Mohr-Coulomb criterion, which considers only the maximum and minimum effective principal stresses. In addition to the second deviatoric invariant used in the Von Mises criterion, the Drucker-Prager criterion incorporates the first invariant into the model.

The Drucker-Prager failure criterion has the form of

$$\sqrt{J_2'} = A + BI_1' \tag{3.33}$$

where J_2' is the second deviatoric invariant of the effective stress, which can be found by substituting the effective stresses in Eq. 3.20, and I_1' is the first invariant of the effective stress or the mean effective stress, which can be found by substituting the effective stress into Eq. 3.17.

The two versions of the Drucker-Prager criteria are the inscribed and circumscribed Drucker-Prager criteria (Nawrocki, 2010). The differences are in the definitions of Parameters A and B.

The inscribed Drucker-Prager criterion:

$$A = \frac{2\sqrt{3}C_0\cos(\omega)}{3 - \sin(\omega)} ; \qquad B = \frac{2\sqrt{3}\sin(\omega)}{3 - \sin(\omega)} \tag{3.34}$$

The circumscribed Drucker-Prager criterion:

$$A = \frac{2\sqrt{3}C_0\cos(\omega)}{3 + \sin(\omega)} ; \qquad B = \frac{2\sqrt{3}\sin(\omega)}{3 + \sin(\omega)} \tag{3.35}$$

where C_0 is the cohesion factor, and ω is the internal friction angle.

The difference between the inscribed and circumscribed Drucker-Prager is their characteristic shape plotted on a π-plane as shown in Figure 3.7 (from Nawrocki, 2010).

44

In this thesis, the inscribed Drucker-Prager criterion was used to evaluate rock shear failure.
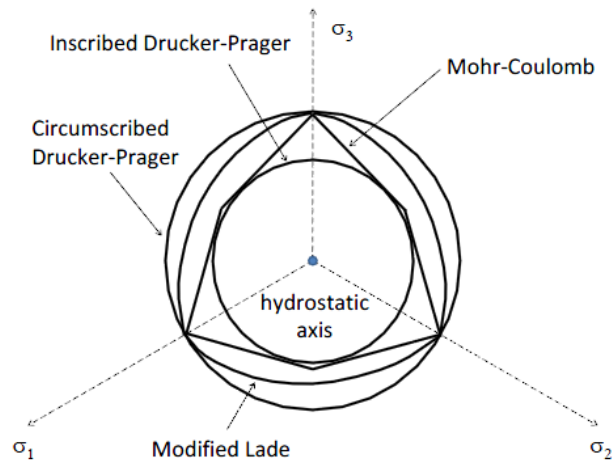
Figure 3.7 – Characteristic shapes of some rock failure criteria on a π-plane (from Nawrocki, 2010).

It is more convenient to rearrange the Drucker-Prager failure criterion in Eq. 3.33 to a form of failure index as presented in Eq. 3.36.

$$FI_{DP} = \frac{2\sqrt{3}C_0\cos(\omega)}{3 - \sin(\omega)} + \frac{2\sqrt{3}\sin(\omega)}{3 - \sin(\omega)}I_1' - \sqrt{J_2'} \tag{3.36}$$

The first term on the right-hand side of Eq. 3.36 represents the rock unconfined compressive strength. The second term refers to the effect of the confining stresses, which help increase rock compressive strength. The third term serves as a destructive stress, causing the shear failure.

By the definition of the Drucker-Prager failure index in Eq. 3.36, the FI_{DP} represents a margin of a stress before the rock will fail under compression (or

shear). The higher FI_{DP} means the more stable of the rock against shear failure, whereas negative FI_{DP} refers to the condition in which rocks fail.

3.5.2 Tensile Failure Criterion

Rocks fail in tensile mode, which is characterized as a pull-apart or split failure, when the rocks undergo excessive tensile stress beyond its limit. In theory, the tensile failure occurs when the effective tensile stress across any plane exceeds a rock tensile strength. The tensile failure in rocks occurs when the condition in Eq. 3.37 is met.

$$\sigma_3' \leq T_0 \qquad (3.37)$$

where σ_3' is the minimum principal stress (compressive positive), and T_0 is the rock tensile strength which is always zero or less than zero (always in tension).

CHAPTER IV

THEORY OF THERMOPOROELASTICITY

A concept of the thermoporoelasticity describes behaviors of porous media that experience temperature and pore-pressure variations. The thermoporoelasticity model was derived from Biot's theory of poroelasticity for fluid-saturated porous media, which was extended to cover temperature differential effects by Kurashige in 1989. In addition to thermal effects from a difference between the thermal expansibility of the pore fluid and solid matrix, Kurashige's model includes heat transportation by fluid flowing through pore spaces, which is caused by the thermally-induced pressure gradient. Kurashige's scheme was slightly improved by Li (1998), whose derivation is a basis of the thermoporoelastic theory presented in this thesis. The objective of this research was to develop a model to study the thermoporoelastic effects on the near-wellbore formation, especially at the bit/formation interface. The origin of the temperature gradient in the formation is the temperature difference between the drilling fluid and formation.

4.1 Governing Conservation Laws

In the context of the thermoporoelasticity theory for fluid-saturated formations, the model couples solid matrix deformation, pore-fluid flow inside pore spaces, and heat transfer through the bulk formation. Three basic conservation laws govern these behaviors:

1. Mechanical equilibrium or linear momentum conservation

2. Mass conservation

3. Energy conservation

4.1.1 Mechanical Equilibrium Equation

Assuming an infinitesimal porous element in a quasi-static condition, equations describing this equilibrium state in 3D Cartesian coordinates are

$$\frac{\partial \sigma_x}{\partial x} + \frac{\partial \tau_{xy}}{\partial y} + \frac{\partial \tau_{xz}}{\partial z} + f_{b_x} = 0 \tag{4.1}$$

$$\frac{\partial \tau_{xy}}{\partial x} + \frac{\partial \sigma_y}{\partial y} + \frac{\partial \tau_{yz}}{\partial z} + f_{b_y} = 0 \tag{4.2}$$

$$\frac{\partial \tau_{xz}}{\partial x} + \frac{\partial \tau_{yz}}{\partial y} + \frac{\partial \sigma_z}{\partial z} + f_{b_z} = 0 \tag{4.3}$$

The body force is negligible because the volume of any infinitesimal element is small enough that the body force is insignificant. By using the Einstein's notation or the tensor notation, Eqs. 4.1 to 4.3 reduce to

$$\nabla \cdot \langle \sigma \rangle = 0 \quad or \quad \sigma_{ij,j} = 0 \tag{4.4}$$

4.1.2 Mass Conservation Law

The law of mass conservation states that a mass of an isolated system (closed to all matter and energy) remains constant over time. Considering an infinitesimal porous sample with saturated pore fluid flowing inside, a mass of solid rock matrix can be assumed relatively constant to an activity of the flowing pore fluid. Thus, the mass

conservation equation for this porous system can be presented in the form of a fluid mass conservation.

$$\frac{\partial m_f}{\partial t} + \nabla \cdot (\rho_f \overrightarrow{v_f}) = 0 \tag{4.5}$$

Darcy's law describes a relationship of a flowing fluid velocity and a differential pressure across a flow medium. For a fully-saturated formation that has isotropic hydraulic properties, Darcy's law simplifies to

$$\overrightarrow{v_f} = -\frac{k}{\mu} \nabla p \tag{4.6}$$

By substituting Eq. 4.6 into Eq. 4.5 and assuming that pore fluid density is constant across a flow medium, Eq. 4.5 becomes

$$\frac{\partial m_f}{\partial t} = \rho_f \frac{k}{\mu} \nabla^2 p \tag{4.7}$$

4.1.3 Energy Conservation Law

Similar to the concept of mass conservation, the law of energy conservation implies that a total among of energy in an isolated system remains constant over time. To pursue interactions inside porous media with flowing pore fluid, we need to construct an energy conservation relation in a solid phase and a fluid phase separately. Temperatures of the solid matrix and pore fluid are related by a heat-convection process at the contact area between the solid matrix and the pore fluid. In some simplified cases in which a thermal interaction between the solid matrix and pore fluid rapidly reaches equilibrium state, it is reasonable to assume that the local thermal equilibrium is reached.

If this assumption is valid and the model accounts for a heat accumulation, bulk heat conduction, and fluid heat convection, the energy conservation for infinitesimal porous media that has isotropic thermal properties can be represented by

$$\rho_b C_b \frac{\partial T}{\partial t} = \kappa^T \nabla^2 T - \rho_f C_f \nabla \cdot (\vec{v_f} T_f) \tag{4.8}$$

The first term on the right-hand side of Eq. 4.8 represents conductive heat transfer through the bulk material (pore fluid and solid matrix). The second term on the right-hand side represents a convective heat transfer by the means of pore-fluid flow through pore spaces.

Because determining the convective heat coefficient between the solid matrix and pore fluid is difficult, we can assume that the mean temperature of the pore fluid and solid matrix are equal. This assumption allows a replacement of the bulk temperature for the pore fluid and solid matrix temperatures ($T = T_m = T_f$). With this assumption, Eq. 4.8 becomes

$$\frac{\partial T}{\partial t} = \frac{\kappa^T \nabla^2 T}{\rho_b C_b} + \frac{\rho_f C_f}{\rho_b C_b} \nabla \cdot (\frac{k}{\mu} \nabla p T) \tag{4.9}$$

4.2 Thermoporoelastic Constitutive Relations

Porous media in the thermoporoelastic model are composed of the solid matrix and fluid-saturated pore space. Their volumes and shapes are altered by effective stresses, pore pressure, and bulk temperature. To govern this phenomenon, we need a model that is capable of describing how the volume of the solid rock matrix and the pore space is affected by the changes of pore pressure and bulk temperature.

A volumetric change of the solid rock matrix for linear elastic materials can be described by Hooke's law incorporating the effective stress concept and a thermoelastic stress.

$$\Delta\epsilon_x = \frac{\Delta\sigma_x}{2G(1+v)} - \frac{v\Delta\sigma_y}{2G(1+v)} - \frac{v\Delta\sigma_z}{2G(1+v)} - B'\Delta p - \alpha_m^{TL}\Delta T \tag{4.10a}$$

$$\Delta\epsilon_y = \frac{\Delta\sigma_y}{2G(1+v)} - \frac{v\Delta\sigma_x}{2G(1+v)} - \frac{v\Delta\sigma_z}{2G(1+v)} - B'\Delta p - \alpha_m^{TL}\Delta T \tag{4.10b}$$

$$\Delta\epsilon_z = \frac{\Delta\sigma_z}{2G(1+v)} - \frac{v\Delta\sigma_y}{2G(1+v)} - \frac{v\Delta\sigma_x}{2G(1+v)} - B'\Delta p - \alpha_m^{TL}\Delta T \tag{4.10c}$$

$$\Delta\epsilon_{xy} = \frac{1}{2G}\Delta\tau_{xy} \tag{4.10d}$$

$$\Delta\epsilon_{yz} = \frac{1}{2G}\Delta\tau_{yz} \tag{4.10e}$$

$$\Delta\epsilon_{xz} = \frac{1}{2G}\Delta\tau_{xz} \tag{4.10f}$$

A volumetric change of pore space on the same material can be described as a function of changes in normal stresses, pore pressure, and temperature.

$$\Delta\phi = -B'\Delta(\sigma_x + \sigma_y + \sigma_z) + D\Delta p + \alpha_p^T\Delta T \tag{4.11}$$

The elastic coefficients B' and D in Eqs. 4.10 and 4.11 are defined as

$$B' = \frac{3(v_u - v)}{2GB(1+v)(1+v_u)} \tag{4.12}$$

$$D = \frac{1}{B}\left(\frac{1}{K} - \frac{1}{K_s'}\right) - \frac{\phi}{K_f} \tag{4.13}$$

Note that the definitions of B and K are

$$B = \frac{3(v_u - v)}{\alpha(1 - 2v)(1 + v_u)} \tag{4.14}$$

$$K = \frac{2G(1 + v)}{3(1 - 2v)} \tag{4.15}$$

A volumetric thermal expansion of the solid matrix was used instead of a linear thermal expansion. If we assume that the pore volume expands with its shape remaining similar to a shape of the solid matrix, the volumetric thermal expansion of pore space, α_p^T, may be related to the volumetric thermal expansion of the solid matrix, α_m^T, via porosity as

$$\alpha_p^T = \phi \alpha_m^T \tag{4.16}$$

By incorporating Eqs. 4.12 to 4.16 into Eqs. 4.10 and 4.11, the constitutive equations of the thermoporoelastic element in the Einstein's notation become

$$\epsilon_{ij} = \frac{1}{2G}\left(\sigma_{ij} - \frac{v}{1 + v}\sigma_{kk}\delta_{ij}\right) - \frac{\alpha(1 - 2v)}{2G(1 + v)}\Delta p\delta_{ij} - \frac{\alpha_m^T}{3}\Delta T\delta_{ij} \tag{4.17}$$

$$\Delta\phi = -\frac{\alpha(1 - 2v)}{2G(1 + v)}\Delta\sigma_{ij}\delta_{ij} + \frac{1}{B}\left(\frac{1}{K} - \frac{1}{K_s'}\right)\Delta p - \frac{\phi}{k_f}\Delta p + \phi\alpha_m^T\Delta T \tag{4.18}$$

It is more practical to express Eq. 4.10 in terms of stresses instead of strains, and then transform them to Eq. 4.19.

$$\Delta\sigma_x = \frac{2G}{1 - 2v}\left[(1 - v)\epsilon_x + v\epsilon_y + v\epsilon_z\right] + \alpha\Delta p + \frac{2G(1 + v)\alpha_m^T}{3(1 - 2v)}\Delta T \tag{4.19a}$$

$$\Delta\sigma_y = \frac{2G}{1 - 2v}\left[(1 - v)\epsilon_y + v\epsilon_x + v\epsilon_z\right] + \alpha\Delta p + \frac{2G(1 + v)\alpha_m^T}{3(1 - 2v)}\Delta T \tag{4.19b}$$

$$\Delta\sigma_z = \frac{2G}{1 - 2v}\left[(1 - v)\epsilon_z + v\epsilon_y + v\epsilon_x\right] + \alpha\Delta p + \frac{2G(1 + v)\alpha_m^T}{3(1 - 2v)}\Delta T \tag{4.19c}$$

$$\Delta \tau_{xy} = 2G\epsilon_{xy} \tag{4.19d}$$

$$\Delta \tau_{xz} = 2G\epsilon_{xz} \tag{4.19e}$$

$$\Delta \tau_{yz} = 2G\epsilon_{yz} \tag{4.19f}$$

Similar to the derivation of strain equations in term of stresses, Eq. 4.19 can be presented in Einstein's notation form as given in Eq. 4.20.

$$\sigma_{ij} = 2G\left(\epsilon_{ij} + \frac{\nu}{1-2\nu}\epsilon_{kk}\delta_{ij}\right) + \alpha p\delta_{ij} + \frac{2G(1+\nu)\alpha_m^T}{3(1-2\nu)}\Delta T\delta_{ij} \tag{4.20}$$

For later derivation, Eq. 4.20 was used to define a new parameter, σ_{kk}, known as volumetric strain, which is equivalent to the first invariant given in Eq. 3.17.

$$\sigma_{kk} = \sigma_x + \sigma_y + \sigma_z = \frac{2G(1+\nu)}{(1-2\nu)}\epsilon_{kk} + 3\alpha p + \frac{2G(1+\nu)\alpha_m^T}{(1-2\nu)}\Delta T \tag{4.21}$$

Note that when the thermoporoelastic solutions derived from the original state where $p_0 = 0$ psi, $T_0 = T_0\,°F$ and $\sigma_0 = 0$ psi, Δp and $\Delta \sigma_{ij}$ become absolute pore pressure and absolute stresses. The ΔT remains a temperature change from the original equilibrium temperature, T_0.

Assuming a porous element that has a pore fluid mass per unit volume described by

$$m_f = \rho_f \phi \tag{4.22}$$

a small variation of a pore fluid mass per unit volume in Eq. 4.22 is

$$dm_f = \rho_f(d\phi) + \phi(d\rho_f) \tag{4.23}$$

A small change of pore fluid density due to pore pressure and temperature variations can be expressed as

$$dp_f = \left(\frac{d\rho_f}{p}\right)\bigg|_T dp + \left(\frac{d\rho_f}{T}\right)\bigg|_p d(\Delta T) \qquad (4.24)$$

By definition, the right-hand side terms in Eq. 4.24 are

$$\left(\frac{d\rho_f}{p}\right)\bigg|_T = \frac{\rho_f}{K_f} \qquad (4.25)$$

$$\left(\frac{d\rho_f}{T}\right)\bigg|_p = -\rho_f \alpha_f^T \qquad (4.26)$$

Substituting Eq. 4.25 and 4.26 into Eq. 4.24, we get

$$d\rho_f = \frac{\rho_f}{K_f} dp - \rho_f \alpha_f^T d(\Delta T) \qquad (4.27)$$

The first term on the right-hand side of Eq. 4.27 describes the effect of a pore-pressure change on a pore-fluid density when temperature is constant. When pore pressure increases, pore fluid volume is compressed, and this leads to an increase in pore-fluid density. The second term on the right-hand side shows the effect of a temperature variation on a pore-fluid density when pore pressure is constant. An increase in temperature causes pore-fluid volume to expand; thus, it makes the system less dense. This reverse impact of the temperature change on the pore fluid density is reflected in Eq. 4.27 with the negative sign.

If we substitute Eq. 4.27 into Eq. 4.23, a relation for a small variation of a fluid mass per unit volume becomes

$$dm_f = \rho_f \left[d\phi + \frac{\phi dp}{K_f} - \phi \alpha_f^T d(\Delta T) \right] \qquad (4.28)$$

To express Eq. 4.28 in terms of rock properties, the constitutive relation of a pore volume change as described by Eq. 4.18 is substituted into the term $d\phi$ in Eq. 4.28 to give Eq. 4.29 below.

$$dm_f = \rho_f \left[-\frac{\alpha(1-2v)}{2G(1+v)} d(\sigma_{ij}\delta_{ij}) + \frac{1}{B}\left(\frac{1}{K} - \frac{1}{K_s'}\right) dp + \phi(\alpha_m^T - \alpha_f^T)d(\Delta T) \right] \qquad (4.29)$$

Considering coefficient of the term dp in Eq. 4.29, which can be simplified by the definitions of K and K_s to give

$$\frac{1}{B}\left(\frac{1}{K} - \frac{1}{K_s'}\right) = \frac{9(v_u - v)}{2GB^2(1+v)(1+v_u)} = \frac{3\alpha(1-2v)}{2GB} \qquad (4.30)$$

By substituting Eq. 4.30 into Eq. 4.29 and replacing $\sigma_{ij}\delta_{ij}$ with σ_{kk} as defined in Eq. 4.21, we get Eq. 4.29 in its most practical form, which is

$$dm_f = \rho_f \left[\frac{\alpha(1-2v)}{2G(1+v)}\left(-d\sigma_{kk} + \frac{3}{B}dp\right) + \phi(\alpha_m^T - \alpha_f^T)d(\Delta T) \right] \qquad (4.31)$$

Note that some authors have defined fluid content per unit volume as $\zeta = \Delta m_f / \rho_f$ and preferred to present Eq. 4.31 in terms of this new parameter. The outcome is Eq. 4.32.

$$\zeta = \left[\frac{\alpha(1-2v)}{2G(1+v)}\left(-d\sigma_{kk} + \frac{3}{B}dp\right) + \phi(\alpha_m^T - \alpha_f^T)d(\Delta T) \right] \qquad (4.32)$$

4.3 Thermoporoelastic Field Equations

All the balance laws and the constitutive relations of the thermoporoelasticity theory are combined to yield three basic governing equations in terms of the fundamental parameters: displacements, pressure, and temperature. These equations are

then converted from the fundamental units system to the field units system (see the nomenclature section for the field units for each parameter).

4.3.1 Deformation Field Equation

For a small deformation in a linear-elastic material, the constitutive strain-displacement relationships from Eqs. 3.7 to 3.12 were applied to Hooke's law in Eq. 4.19. Then we substituted this constitutive relation into Eq. 4.4, the mechanical equilibrium equation in Cartesian coordinates. We finally got the 3D equilibrium equations that are presented in terms of displacements instead of stresses in Eqs. 4.33 to 4.35:

$$\frac{2G(1-v)}{(1-2v)}\frac{\partial^2 u_x}{\partial x^2} + \frac{2Gv}{(1-2v)}\frac{\partial^2 u_y}{\partial x \partial y} + \frac{2Gv}{(1-2v)}\frac{\partial^2 u_z}{\partial x \partial z}$$

$$+ G\left(\frac{\partial^2 u_x}{\partial y^2} + \frac{\partial^2 u_y}{\partial y \partial x} + \frac{\partial^2 u_x}{\partial z^2} + \frac{\partial^2 u_z}{\partial z \partial x}\right) + \alpha\frac{\partial p}{\partial x} \tag{4.33}$$

$$+ \frac{2G(1+v)\alpha_m^T}{3(1-2v)}\frac{\partial \Delta T}{\partial x} = 0$$

$$\frac{2G(1-v)}{(1-2v)}\frac{\partial^2 u_y}{\partial y^2} + \frac{2Gv}{(1-2v)}\frac{\partial^2 u_x}{\partial y \partial x} + \frac{2Gv}{(1-2v)}\frac{\partial^2 u_z}{\partial y \partial z}$$

$$+ G\left(\frac{\partial^2 u_x}{\partial x \partial y} + \frac{\partial^2 u_y}{\partial x^2} + \frac{\partial^2 u_y}{\partial z^2} + \frac{\partial^2 u_z}{\partial z \partial y}\right) + \alpha\frac{\partial p}{\partial y} \tag{4.34}$$

$$+ \frac{2G(1+v)\alpha_m^T}{3(1-2v)}\frac{\partial \Delta T}{\partial y} = 0$$

$$\frac{2G(1-v)}{(1-2v)}\frac{\partial^2 u_z}{\partial z^2} + \frac{2Gv}{(1-2v)}\frac{\partial^2 u_x}{\partial z\partial x} + \frac{2Gv}{(1-2v)}\frac{\partial^2 u_y}{\partial z\partial y}$$

$$+ G\left(\frac{\partial^2 u_x}{\partial x\partial z} + \frac{\partial^2 u_z}{\partial x^2} + \frac{\partial^2 u_y}{\partial y\partial z} + \frac{\partial^2 u_z}{\partial y^2}\right) + \alpha\frac{\partial p}{\partial z} \qquad (4.35)$$

$$+ \frac{2G(1+v)\alpha_m^T}{3(1-2v)}\frac{\partial\Delta T}{\partial z} = 0$$

In the form of Einstein's notation, Eqs. 4.33 to 4.35 can be reduced to

$$Gu_{i,jj} + \frac{G}{1-2v}u_{j,ij} + \alpha p_{,i} + \frac{2G\alpha_m^T(1+v)}{3(1-2v)}\Delta T_{,i} = 0 \qquad (4.36)$$

4.3.2 Pore Fluid Diffusivity Field Equation

From a small fluid mass variation presented by Eq. 4.31 and the total stress in terms of the first invariant presented in Eq. 4.21, we differentiated them with respect to time and get

$$\frac{\partial m_f}{\partial t} = \rho_f\left[\frac{\alpha(1-2v)}{2G(1+v)}\left(-\frac{\partial\sigma_{kk}}{\partial t} + \frac{3}{B}\frac{\partial p}{\partial t}\right) + \phi\left(\alpha_m^T - \alpha_f^T\right)\frac{\partial(\Delta T)}{\partial t}\right] \qquad (4.37)$$

$$\frac{\partial\sigma_{kk}}{\partial t} = \frac{2G(1+v)}{(1-2v)}\frac{\partial\epsilon_{kk}}{\partial t} + 3\alpha\frac{\partial p}{\partial t} + \frac{2G(1+v)\alpha_m^T}{(1-2v)}\frac{\partial(\Delta T)}{\partial t} \qquad (4.38)$$

By substituting Eq. 4.38 into the term in Eq. 4.37, it becomes

$$\frac{\partial m_f}{\partial t} = \rho_f\left[-\alpha\frac{\partial\epsilon_{kk}}{\partial t} + \frac{3\alpha(1-2v)(1-B\alpha)}{2G(1+v)B}\frac{\partial p}{\partial t} + (\phi\alpha_m^T - \phi\alpha_f^T\right.$$
$$\left. - \alpha\alpha_m^T)\frac{\partial(\Delta T)}{\partial t}\right] \qquad (4.39)$$

By applying Eq. 4.14 into Eq. 4.39, the term B vanishes and Eq. 4.39 becomes

$$\frac{\partial m_f}{\partial t} = \rho_f \left[-\alpha \frac{\partial \epsilon_{kk}}{\partial t} + \frac{\alpha^2(1-2v)(1-2v_u)}{2G(v_u-v)} \frac{\partial p}{\partial t} + (\phi \alpha_m^T - \phi \alpha_f^T \right.$$

$$\left. - \alpha \alpha_m^T) \frac{\partial(\Delta T)}{\partial t} \right] \tag{4.40}$$

Finally, we substituted Eq. 4.40 into the mass balance equation, Eq. 4.7, and rearranged to get the fluid diffusion relation in terms of the pressure/time differential, which is

$$\frac{\partial p}{\partial t} = M \left[\frac{k}{\mu} \nabla^2 p + \alpha \frac{\partial \epsilon_{kk}}{\partial t} + \left(\alpha \alpha_m^T + \phi \alpha_f^T - \phi \alpha_m^T \right) \frac{\partial(\Delta T)}{\partial t} \right] \tag{4.41}$$

where

$$M = \frac{2G(v_u - v)}{\alpha^2(1-2v)(1-2v_u)} \tag{4.42}$$

By definition, we may refer to $\epsilon_{kk} = \epsilon_x + \epsilon_y + \epsilon_z$ as the volumetric strain, ϵ_{vol}. To allow Eq. 4.41 to take the field units, a conversion coefficient was introduced into Eq. 4.41.

$$\frac{\partial p}{\partial t} = M \left[7.3266 \times 10^{-8} \frac{k}{\mu} \nabla^2 p + \alpha \frac{\partial \epsilon_{vol}}{\partial t} + \left(\alpha \alpha_m^T + \phi \alpha_f^T - \phi \alpha_m^T \right) \frac{\partial(\Delta T)}{\partial t} \right] \tag{4.43}$$

4.3.3 Thermal Diffusivity Field Equation

We rewrote Eq. 4.9 with Einstein's notation for a formation with thermal properties in Eq. 4.44:

$$\frac{\partial T}{\partial t} = \frac{\kappa^T}{\rho_b C_b} T_{,ii} + \frac{k \rho_f C_f}{\mu \rho_b C_b} \left(T p_{,i} \right)_{,i} \tag{4.44}$$

By nature, Eq. 4.44 is presented in field parameters, which are temperature and pore pressure; thus, no further modification is required. However, the conversion coefficients were applied to allow Eq. 4.44 to take the field units. The result is Eq. 4.45:

$$\frac{\partial T}{\partial t} = \frac{\kappa^T}{3600\rho_b C_b}\nabla^2 T + 7.3266 \times 10^{-8}\frac{k\rho_f C_f}{\mu\rho_b C_b}[(\nabla T)\cdot(\nabla p) + T\nabla^2 p] \tag{4.45}$$

4.4 Physical Interpretations and Applications

From the previous derivation of the thermoporoelasticity theory, displacements, pore pressure, and temperature were coupled with one another through Eqs. 4.36, 4.43, and 4.45. Additionally, the coupling of pressure terms in thermal diffusion causes the solution to involve a nonlinear partial differential equation.

The complexity of the fully coupled relation in thermoporoelasticity theory usually requires some assumptions to simplify the relationships by decoupling or neglecting some trivial terms from the equations. Validity of these simplifications is based on conditions of a problem such as what phenomenon is negligible, or how accurate the solution needs to be.

It is important to have a clear physical interpretation of each term in the three governing equations. This understanding will help provide a logical decision of what assumptions and simplifications can be made while the solution is still feasible for the given problem.

First, we refer to the deformation equation which is re-stated below:

$$Gu_{i,jj} + \frac{G}{1-2\nu}u_{j,ij} + \alpha p_{,i} + \frac{2G\alpha_m^T(1+\nu)}{3(1-2\nu)}\Delta T_{,i} = 0 \qquad (4.36)$$

The first two terms on the left-hand side of Eq. 4.46 are the compressive

effective stresses in the solid matrix that arise from shape and volume deformations of

the bulk. The third term is the equivalent stress from the pore pressure. The fourth term

represents the compressive thermal stress caused by a restriction in shape change when

thermal strain takes place. To comply with the mechanical equilibrium law, the

summation of all stresses must yield the balance shown in Eq. 4.36.

In the thermal diffusivity equation as being repeated again below,

$$\frac{\partial T}{\partial t} = \frac{\kappa^T}{\rho_b C_b}T_{,ii} + \frac{k\rho_f C_f}{\mu \rho_b C_b}\left(Tp_{,i}\right)_{,i} \qquad (4.44)$$

The first term on the right-hand side of Eq. 4.44 is the heat conduction through

the bulk body (solid and fluid). With the assumption that solid matrix is always at

thermal equilibrium with pore fluid (matrix and pore-fluid temperature are equal), we

can represent both the solid matrix and the pore-fluid temperatures by the bulk

temperature. The second term on the right-hand side corresponds to the heat convection

in which fluid flows through the porous medium and transports heat flux along with it.

Combining the conduction and the convection effects results in the local temperature

represented by the term on the left-hand side.

In many cases where formations have low permeability such as tight sand and

shale, the conduction effect dominates the convection. Thus, the convection term on the

right-hand side can be omitted. One major consequence of this reduction is that the

thermal-diffusivity equation becomes mathematically linear. The linear equation is much

less expansive to solve either analytically or numerically. On the other hand, for high-permeability formations in which heat convection is dominant, we may consider disregard the conduction term in Eq. 4.44.

For the pressure diffusivity equation shown again below,

$$\frac{\partial p}{\partial t} = M \left[\frac{k}{\mu} \nabla^2 p + \alpha \frac{\partial \epsilon_{kk}}{\partial t} + \left(\alpha \alpha_m^T + \phi \alpha_f^T - \phi \alpha_m^T \right) \frac{\partial (\Delta T)}{\partial t} \right] \tag{4.41}$$

The first term in the right-hand side of Eq. 4.41 is the pressure diffusion in formation under the Darcy's law. The second term is a change of pore volume as a result of solid matrix deformation. The last term on the right-hand side is a pore-pressure change because the temperature induces volumetric changes of pore fluid and solid matrix.

CHAPTER V

NUMERICAL MODEL

This thesis developed a model to study the effect of the temperature difference between the drilling fluid and formation. The goal was to clarify whether the thermal effect on formation stress is a main factor leading to a rate of penetration difference in high-temperature/high-pressure (HTHP) well drilling incidents.

By assuming linear-elastic formation properties, the stress solution from the model presents a mathematical linearity. As a result, the stress solution can be separated into two components (Eq. 5.1). The first component is the stress state of formation evacuation under an isothermal condition. The second component is the induced stress from temperature gradients in formations of the same geometry. In this thesis, these two stress components are solved separately, and then are superpositioned to yield the complete thermoporoelastic stress solution. The first module solves the stress-state solution of the formation evacuation using the 2D-axisymmetric Fourier-assisted finite-element method. The second module solves the thermally induced stresses solution using the combined axisymmetric finite-difference/finite-element method.

$$\sigma_{\text{total}} = \sigma_{\text{evacuation}} + \Delta\sigma_{\text{thermal}} \tag{5.1}$$

The geometry of the model (for both modules) is shown in Figure 5.1. It is 2D axisymmetric with a 9-node square finite-element. In this thesis, the top boundary extends 10 wellbore radii above the bottomhole datum; the bottom boundary extends 10

wellbore radii below the bottomhole datum; the radial boundary extends 20 wellbore radii from the wellbore wall; the inner boundary is the wellbore center. The model aims to predict the temperature effects at the bottomhole region on formation drillability. With the top boundary extended to cover the wellbore wall region, the model also provides a stress solution at the wellbore wall.
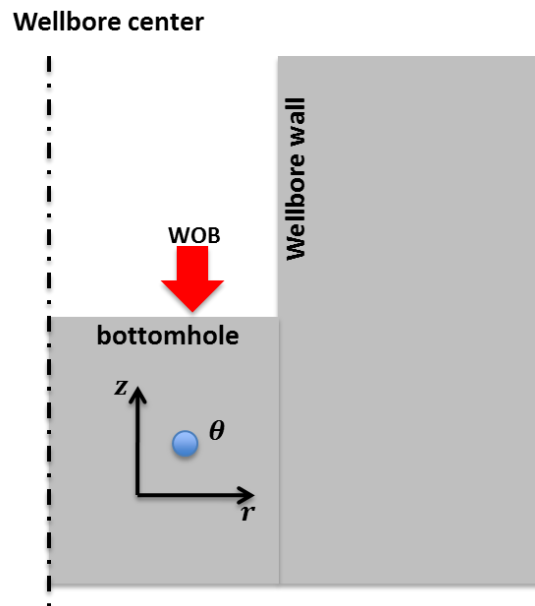
Figure 5.1 – Model geometry represents bottomhole and wellbore-wall location. The boundaries are selected to extend 10's wellbore radii above and below bottomhole and 20's wellbore radii away from the wellbore wall.

A constant downward stress as a weight-on-bit (WOB) is applied at the bottom of the hole to produce the stress state when the drill bit is attacking the formation. The WOB is required because the model attempts to evaluate the thermal effects on the rock drillability in a form of failure likelihood at the bit/formation interface. The downward

load in this model is only a simplified method to evaluate a rock failure under a vertical load. The load components and characteristics do not perfectly reproduce the real stress components created by the real drill bit.

Details of the derivation of the numerical formulations for the stress-state solution of the formation evacuation, and the thermally induced stress solution are presented in Appendix A and Appendix B.

5.1 Assumptions and Simplifications

Some assumptions and simplifications are applied to the model to reduce the complexity and computational effort with a minimal effect on the validity of the solution for the problem of interest. The setting of the model is in a shale formation, which is the dominant formation type in most US gulf coast drilling operations. Major assumptions and simplifications of this model are listed below:

1. The formation is a linear-elastic material with isotropic properties. Pore space is fully saturated with a single-phase fluid (the model assumes liquid).

2. The solid matrix has a lower compressibility than the pore fluid; therefore, the pore pressure change from solid matrix deformation is negligible in the pressure-diffusivity equation.

3. Heat conduction is the dominant heat transfer process because of the low-permeability of shale formations. As a result, the heat convection term is omitted from the thermal-diffusivity equation.

4. Pore fluid flows under Darcy's law.

5. The wellbore is impermeable (as if it has a filter cake); thus, the wellbore pressure and formation pressure along the wellbore/formation boundaries are disconnected.

6. The thermal interactions between the solid matrix and the pore fluid are always at equilibrium state; therefore, the pore-fluid temperature and solid-matrix temperature are always equal.

7. Well geometry is vertical.

8. The model is capable of anisotropic in-situ stress. However, cases provided in this thesis have isotropic in-situ stress boundaries.

9. The rock-breaking stress from the bit-cutter/tooth on the bottomhole formation is assumed to be a pure 8,000-psi vertical stress. [A validation of WOB stress: WOB serves as a destructive stress; therefore, its magnitude needs to be higher than the maximum in-situ stress. In the work of Zhang and Roegiers (2005), the model assumed bit-cutter/tooth load of 40% higher than the magnitude of the maximum in-situ stress. In this thesis, the maximum in-situ stress is a 7,000-psi overburden; thus, 8,000 psi of bit-cutter/tooth load is reasonable for a low-bit-load case.]

Figure 5.2 shows simplification of the thermoporoelasticity theory under the effects of assumptions in the first three bullets.

With the assumptions stated above, the finding of this model best fits for shale formation with low solid-matrix compressibility (high solid-matrix stiffness).
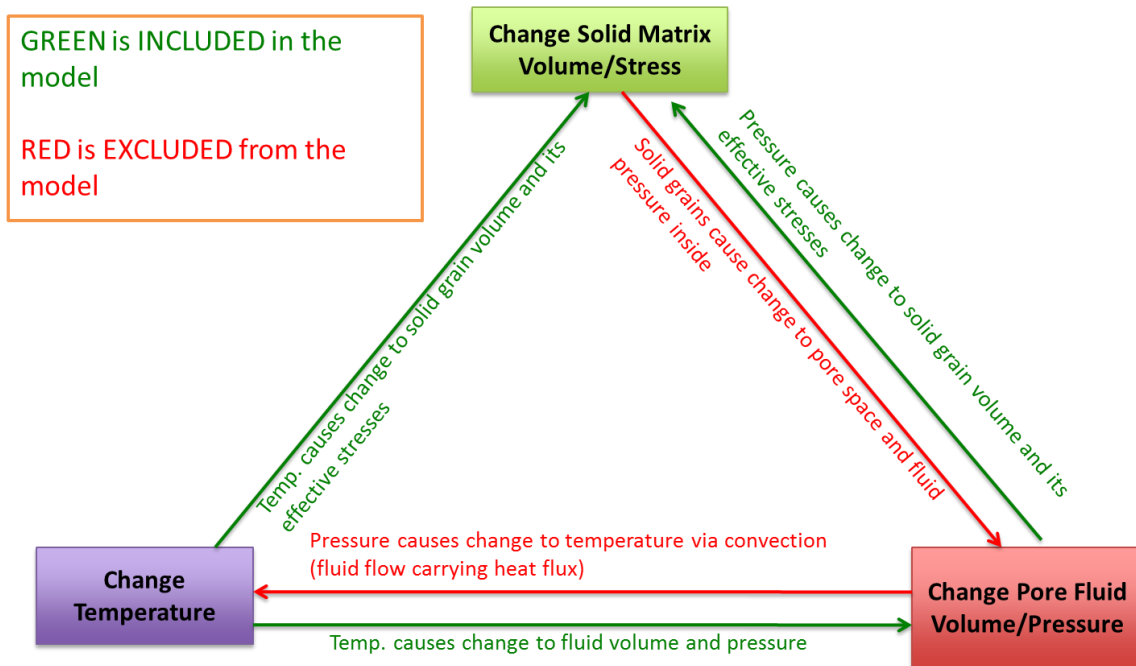
Figure 5.2 – Diagram of simplified thermoporoelasticity theory used in the model developed by this thesis. The effects of solid-matrix deformation in pore-pressure change and heat convection in temperature diffusion are neglected.

5.2 Module 1: Formation Evacuation with Weight-on-Bit

The first module provides a poroelastic stress state when the formation is evacuated to make a vertical hole (the first stress component in the right-hand side of Eq. 5.1). The model assumes a balanced drilling operation to eliminate the effect of the pressure difference between wellbore and formation from the stress solution. With the assumptions in Bullets 1 and 2 in Section 5.1, the pressure diffusion in this module is disregarded. Low permeability prevents any fluid flow, and solid matrix deformation has no effect on pore pressure; therefore, the pore pressure remains constant. As a result, this module takes uncoupled poroelastic relations (Eqs. 5.2 and 5.3) as the governing equations.

$$Gu_{i,jj} + \frac{G}{1-2v}u_{j,ij} = 0 \tag{5.2}$$

$$\frac{\partial p}{\partial t} = 0 \quad or \quad p = p_f \tag{5.3}$$

The nature of this numerical solution is 3D. Figure 5.3 shows the boundary stresses in the Cartesian coordinates and the cylindrical coordinates, which are interchangeable via the stress transformation presented in Eq. 3.13. The in-situ principal stresses, which are the maximum horizontal stress, the minimum horizontal stress, and the vertical stress, are constant in the Cartesian coordinates. When the problem is solved using cylindrical coordinates, the cylindrical boundary stresses, which are functions of the constant in-situ principal stress, have the cosine Fourier-series forms as shown in Eqs. 5.4 to 5.6.
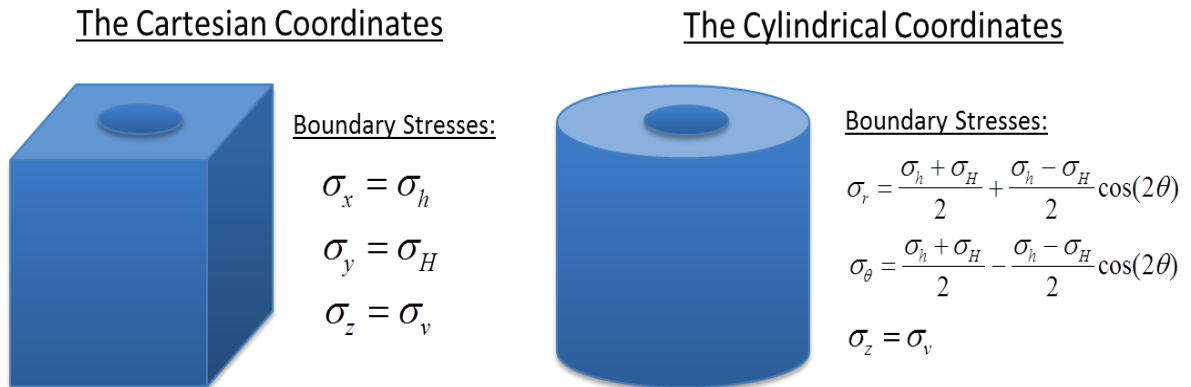
Figure 5.3 – Boundary stresses in the Cartesian coordinates and the cylindrical coordinates. In the Cartesian system, the boundary stresses are constant. When transformed to the cylindrical system, boundary stresses can be described in the Fourier-series form which allows an application of Fourier-Assisted Finite-Element technique.

$$S_r = \frac{S_H + S_h}{2} + \frac{S_H - S_h}{2}\cos(2\theta) \tag{5.4}$$

$$S_\theta = \frac{S_H + S_h}{2} - \frac{S_H - S_h}{2}\cos(2\theta) \tag{5.5}$$

$$S_z = \sigma_v \tag{5.6}$$

where θ is the counter-clockwise angle from the direction of the minimum horizontal stress, S_H is the maximum horizontal stress, S_h is the minimum horizontal stress, and S_v is the vertical stress or overburden.

With the boundary stresses in the Fourier-series form, the application of the Fourier-assisted finite-element technique becomes valid. The benefit of the Fourier-assisted finite-element method is a dimension reduction from the 3D geometry to the 2D axisymmetric geometry while the displacement and stress solutions remain in 3D. Moreover, the complete solutions can be solved by the superposition of the solution from each Fourier harmonic, which are the zero and second harmonics.

The point-load WOB of 8,000 psi is applied in the downward-vertical direction at 0.6 wellbore radii from the well center. This stress is assumed to affect the formation vertical stress at the bit/formation interface only, while radial and tangential stresses at the same location remain unaffected. Although this vertical bit load is ideal, the concept is simple and able to provide a quick look at rock failure under the bit load.

5.2.1 Numerical Equations

This module uses the cylindrical coordinates system; thus, the boundary stresses in Eqs. 5.4 to 5.6, which contain the zero-cosine and second-cosine Fourier harmonic

terms, are used. The *n*-harmonic numerical formulation of the deformation equation given in Eq. A-53 reduces to two harmonic numerical equations, which are

$$[K_{u,0}^g][\hat{\bar{u}}_n] + [K_{pu,0}^g][\widehat{\bar{P}_0}] = [F_{ex,0}] \tag{5.7}$$

$$[K_{u,2}^g][\hat{\bar{u}}_n] + [K_{pu,2}^g][\widehat{\bar{P}_2}] = [F_{ex,2}] \tag{5.8}$$

With the assumptions given in Section 5.1, this module has constant pore pressure throughout the domain. This causes the terms $[K_{pu,0}^g][\widehat{\bar{P}_0}]$ and $[K_{pu,2}^g][\widehat{\bar{P}_2}]$ to give zero; as a result, Eqs. 5.7 and 5.8 become

$$[K_{u,0}^g][\hat{\bar{u}}_n] = [F_{ex,0}] \tag{5.9}$$

$$[K_{u,2}^g][\hat{\bar{u}}_n] = [F_{ex,2}] \tag{5.10}$$

where $[K_{u,0}^g]$ and $[K_{u,2}^g]$ are defined in Eq. A-54.

5.2.2 Boundary Conditions

Figure 5.4 shows the boundary conditions used in the models for the solutions of the zero-cosine harmonic and second-cosine harmonic components as given in Eqs. 5.4 to 5.6. The figure also presents the methodology of the superposition to solve the complete solution in the Module 1.

For the zero-cosine harmonic component, the boundary conditions used in this model are listed below:

- Wellbore wall boundary: Constant wellbore pressure (equal to formation pore pressure)

- Wellbore bottomhole boundary: Constant wellbore pressure with 8,000-psi WOB at 0.6 wellbore radii from well center

- Top boundary: Overburden stress

- Radial far-field boundary: S_1 for the radial and tangential stresses

- Bottom boundary: Overburden stress

- Well center: Zero radial displacement
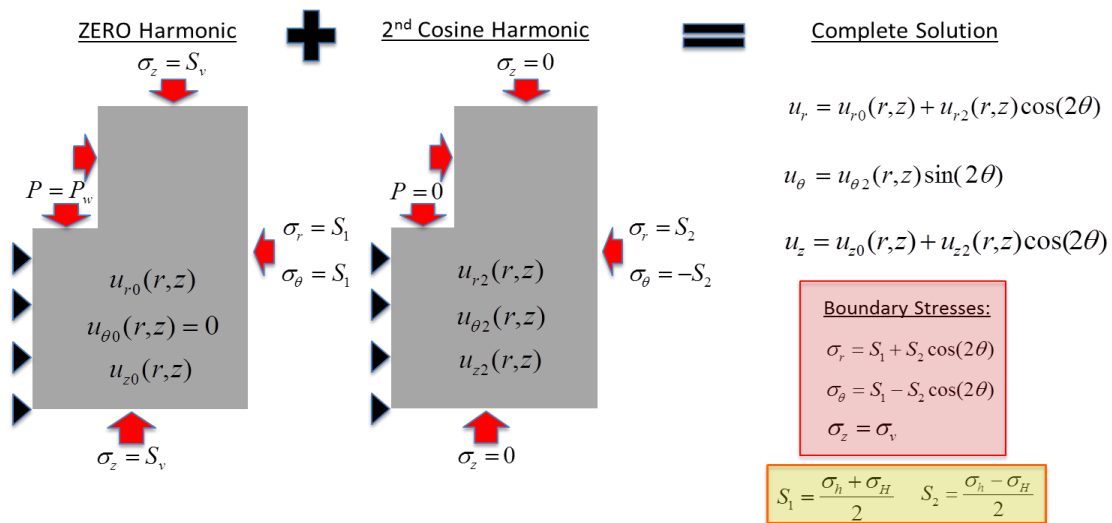
Figure 5.4 – Diagram explains superposition technique to solve the Fourier-series boundary stresses problem in 2D axisymmetric geometry. The solution of each harmonic is solved separately and then combined to give the complete stress-state solution.

For the second-cosine-harmonic component, the boundary conditions used in this model are listed below:

- Wellbore wall boundary: Zero pressure

- Wellbore bottomhole boundary: Zero pressure

- Top boundary: Zero stress

- Radial far-field boundary: S_2 for the radial stress, and $-S_2$ for the tangential stress

- Bottom boundary: Zero stress

- Well center: Zero radial displacement

5.3 Module 2: Thermal-Induced Stress

This second module focuses on the stresses that are induced in shale by the temperature gradient in the formation as a result of the drilling-fluid temperature. The model incorporates the partially coupled thermoporoelasticity relations as shown in Figure 5.2, which decouples the matrix deformation effect on pore pressure alteration and neglects the convective heat transfer in porous media following the assumptions in Section 5.1. Similar to Module 1, the model in Module 2 is solved under a balanced drilling condition to remove any induced effects of pressure difference between wellbore and formation. The partially coupled thermoporoelastic governing equations, which are derived from Eqs. 4.43, 4.45, and 4.36, are

$$\frac{\partial T}{\partial t} = \frac{\kappa^T}{3600\rho_b C_b} \nabla^2 T \tag{5.12}$$

$$\frac{\partial p}{\partial t} = M\left[7.3266 \times 10^{-8}\frac{k}{\mu}\nabla^2 p + \left(\alpha\alpha_m^T + \phi\alpha_f^T - \phi\alpha_m^T\right)\frac{\partial(\Delta T)}{\partial t}\right] \tag{5.11}$$

$$Gu_{i,jj} + \frac{G}{1-2v}u_{j,ij} + \alpha p_{,i} + \frac{2G\alpha_m^T(1+v)}{3(1-2v)}\Delta T_{,i} = 0 \tag{5.13}$$

where M is defined in Eq. 4.42.

Because Module 2 solves for the induced effect, the model is 2D axisymmetric by nature. The temperature and pore pressure vary in the radial direction, but have no gradient in the tangential direction (at the same radial distance from the wellbore). This leads to the stress and deformation solutions having the same characteristics, which make axisymmetric geometry valid for this problem.

5.3.1 Numerical Equations

As presented in Appendix A, the numerical formulations for Eqs. 5.11 to 5.13 are given in Eqs. 5.14 to 5.16 respectively.

$$[K_T^g][\hat{T}^{t+1}] = [R_T^g][\hat{T}^t] \tag{5.14}$$

$$[K_P^g][\hat{P}^{t+1}] + [K_{Tp}^g][\hat{T}^{t+1}] = [R_p^g][\hat{P}^t] + [R_{Tp}^g][\hat{T}^t] \tag{5.15}$$

$$[K_u^g][\hat{u}] - [K_{pu}^g][\hat{P}] - [K_{Tu}^g][\hat{T}] = [F_u^g] \tag{5.16}$$

Eqs. 5.14 and 5.15, temperature diffusion and pore-pressure diffusion respectively, are formulated with the finite-difference method. The deformation equation, Eq. 5.16, is formulated with the finite-element method.

To account for the decoupling simplification, Eqs. 5.14 to 5.16 are solved separately and in order. Eq. 5.14 solves the induced temperature solution, which is substituted into Eq. 5.15 to give the induced pore pressure. Finally, both solutions are substituted into Eq. 5.16 and solved for induced displacement.

5.3.2 Boundary Conditions

To investigate the induced effect from the previous equilibrium state, the boundary conditions in this module are fixed constant at zero. Choices of wellbore-formation boundary are permeable and impermeable boundaries. The permeable boundary is an extreme case in which the wellbore has no restriction in fluid flowing across the boundary. This scenario is likely in high permeable formations with no filter cake. The result is that the formation pressure along the wellbore boundary is always equal to the pressure inside the well. The impermeable formation is the other extreme case in which the wellbore fully restricts the fluid communication between wellbore and formation. The impermeable wellbore condition may occur when drilling in impermeable formations, or drilling under effective filter cake, or drilling with oil-based drilling fluid in shale. The result is that the formation pressure along the wellbore boundary varies with time, effects of temperature, and formation properties. In this thesis, the impermeable case is assumed.

The boundary conditions used in this model are listed below:

- Wellbore wall boundary: Zero differential pressure (balanced drilling)
- Wellbore bottomhole boundary: Zero differential pressure (balanced drilling)
- Top boundary: Zero vertical induced displacement
- Radial far-field boundary: Zero radial induced displacement
- Bottom boundary: Zero vertical induced displacement
- Well center: Zero radial induced displacement

5.4 Thermoporoelastic Stress Solution

To model the thermoporoelastic stress state of the problem, the stress solutions from Module 1 and Module 2 are obtained separately and combined using superposition. The fundamental solutions given by the numerical model is the displacement solution. The effective stress solution at each integration point is acquired using the displacement solution with Eq. 5.17.

$$[\sigma'] = [C][B_u][u] \tag{5.17}$$

where $[B_u]$ is defined in Eq. C-47.

In this thesis, stress solution in forms of effective principal stresses is more meaningful for formation failure evaluation than a stress state presented in standard orthogonal coordinates such as the cylindrical coordinates. Therefore, the resultant stress state given by Eq. 5.17 is transformed into three effective principal stresses following the method discussed in Section 3.1.4.

Because no shear stress occurs in the near-wellbore wall-stress state, the radial, tangential, and vertical stress solutions are already in the principal direction. There are concentrated shear stress in r-z direction at the bottomhole corner whose effect extend cover most of the near-bottomhole region. Therefore, the stress state at the bottomhole area needs to be transformed into the principal directions.

5.5 Evaluation of Thermal Effects on Rock Drillability

As discussed in the Section 3.5, rock drillability is a function of a rock-compressive failure index under WOB load and a tensile strength in the direction of bit

rotation. The model separately investigates the bottomhole stress state with the inscribed Drucker-Prager failure index and the tensile failure criterion in the tangential direction.

The model for evaluating a potential of rock compressive failure due to bit-drilling activity carries a similar concept to the polyaxial test in a laboratory as shown in Figure 5.5. The vertical WOB serves as a destructive force trying to break the rock while the intermediate and minimum principal stresses are confining stresses giving rock resistance to fail. In this rock failure model, the WOB is a constant point-load stress, whereas the confining stresses are altered by temperature. With less Drucker-Prager failure index, the rock has more potential to failure under compression.
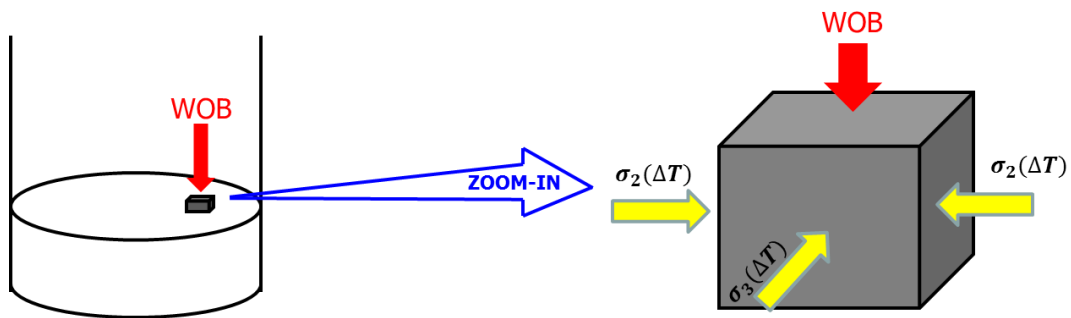
Figure 5.5 – The diagram shows model to evaluate a rock compressive failure which is similar to the concept of polyaxial test. The WOB is a force acting to break the rock. The intermediate and minimum principal stresses are confining stresses. The WOB is held constant while the confining stresses are temperature-dependent.

To evaluate rock failure in tensile mode, the model considers the tangential-tensile failure index, which is changed with temperature. The rock has more potential to failure in tension when the model presents less tensile failure index.

Figure 5.6 shows the methodology used in this model to give a pure thermal-induced effect on rock drillability. The failure index of the non-isothermal cases is a function of the effective principal stresses solved from combined Module 1 and Module 2. The failure index of the base case—the isothermal case—is a function of the effective principal stresses solved from Module 1 alone. Because both cases have the same inputs except the temperature, the difference between failure indices of two cases in Figure 5.5 gives the sole induced effects of temperature on the rock-failure index.
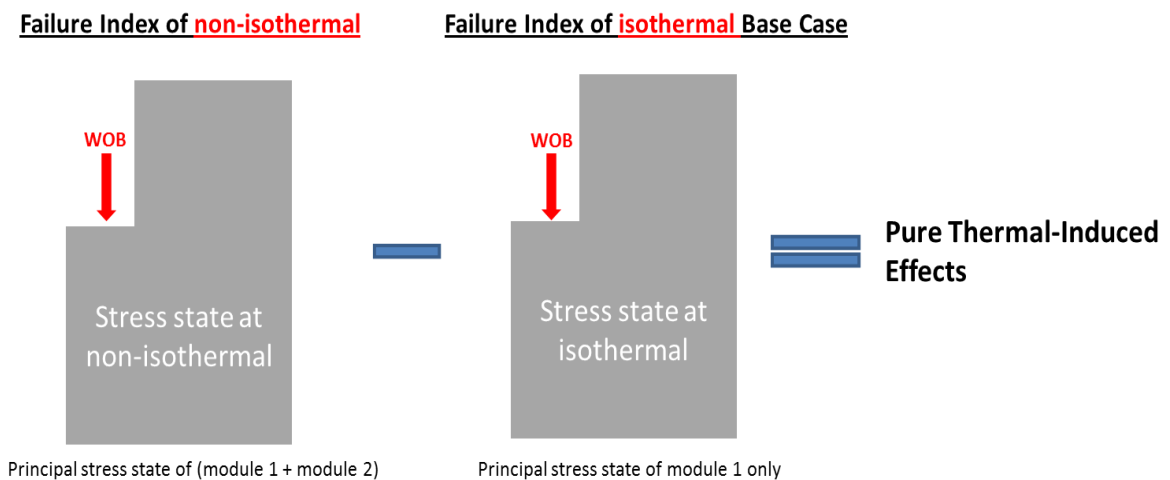
Figure 5.6 – Diagram presents methodology for evaluating pure thermal-induced effects.

CHAPTER VI

MODEL VALIDATIONS

Limited work has been done at the bottom of the hole; therefore, the comparison is only valid for stress solutions at the wellbore wall. This thesis compares solutions at the wellbore wall solved by our model with the known analytical solutions and/or results published in literature. The stress result at the bottom of the hole is presumed to have the same accuracy and reliability as the response at the wellbore wall.

The model validation is separated into two parts: validation for the stress state caused by formation evacuation under isothermal conditions, and validation for the partially coupled thermoporoelastic stress solution. The first validation is to justify the solution of Module 1, and the second validation is for the solution of Module 2.

The stress-state solution at the wellbore wall of Module 1 agreed perfectly with the uncoupled-poroelastic analytical solution. The partially coupled thermoporoelastic stress solution at the wellbore wall, which combined the stress-solutions of Modules 1 and 2, was compared to the analytical solution published by Zhai et al (2009) and presented similar stress responses. Moreover, the conclusions of thermal effects on wellbore stability from this thesis were compared to conclusions published in many literatures on the same topic and were found to coincide.

6.1 Validation of the Formation Evacuation Model

The stress-state solution in the cylindrical coordinates produced by Module 1 was compared to the analytical wellbore-wall stress solution given in Eqs. 6.1 to 6.6 (Zhai et al, 2009).

$$\sigma_r(r,\theta) = \frac{\sigma_x + \sigma_y}{2}\left(1 - \frac{R_w^2}{r^2}\right) + \frac{\sigma_x - \sigma_y}{2}\left(1 + 3\frac{R_w^4}{r^4} - 4\frac{R_w^2}{r^2}\right)\cos(2\theta)$$
$$+ \tau_{xy}\left(1 + 3\frac{R_w^4}{r^4} - 4\frac{R_w^2}{r^2}\right)\sin(2\theta) + P_w\frac{R_w^2}{r^2} \tag{6.1}$$

$$\sigma_\theta(r,\theta) = \frac{\sigma_x + \sigma_y}{2}\left(1 + \frac{R_w^2}{r^2}\right) - \frac{\sigma_x - \sigma_y}{2}\left(1 + 3\frac{R_w^4}{r^4}\right)\cos(2\theta)$$
$$- \tau_{xy}\left(1 + 3\frac{R_w^4}{r^4}\right)\sin(2\theta) - P_w\frac{R_w^2}{r^2} \tag{6.2}$$

$$\sigma_z(r,\theta) = \sigma_v - v\left[2(\sigma_x - \sigma_y)\frac{R_w^2}{r^2}\cos(2\theta) + 4\tau_{xy}\frac{R_w^2}{r^2}\sin(2\theta)\right] \tag{6.3}$$

$$\tau_{r\theta}(r,\theta) = \left[\frac{\sigma_y - \sigma_x}{2}\sin(2\theta) + \tau_{xy}\cos(2\theta)\right]\left(1 - 3\frac{R_w^4}{r^4} + 2\frac{R_w^2}{r^2}\right) \tag{6.4}$$

$$\tau_{\theta z}(r,\theta) = \left(-\tau_{xz}\sin\theta + \tau_{yz}\cos\theta\right)\left(1 + \frac{R_w^2}{r^2}\right) \tag{6.5}$$

$$\tau_{rz}(r,\theta) = \left(\tau_{xy}\cos\theta + \tau_{yz}\sin\theta\right)\left(1 - \frac{R_w^2}{r^2}\right) \tag{6.6}$$

The input parameters given in Table 6.1 were used as a test case in the model and the analytical solutions. This case represents the balanced-drilling scenario in a formation with isotropic in-situ stress and isothermal conditions (drilling fluid temperature equal to formation temperature).

The stress-state solution including the effective radial stress, the effective tangential stress, and the effective vertical stress, solved by Module 1 from this thesis flawlessly matched the analytical solution (Figure 6.1).

Table 6.1 – Input parameters for validation of stress-state
solution due to formation evacuation (Module 1).

Parameters	Abb.		Units
Maximum Horizontal Stress	Sx =	5000	psi
Minimum Horizontal Stress	Sy =	5000	psi
Vertical Stress	Sv =	7000	psi
Pore Pressure	Pw =	2500	psi
Angle from Minimum Horizontal Stress	AZI =	0	degrees Angle
Possion's Ratio	v =	0.25	
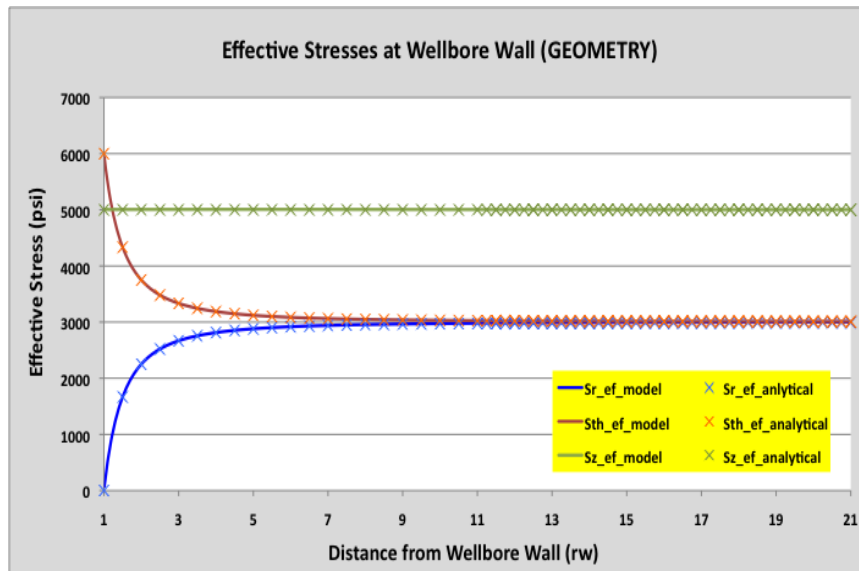
Figure 6.1 – Stress-state solutions at the wellbore-wall from Module 1 and the analytical
solutions. The plot presents exact match of solutions and confirms validation of stress
solution due to formation evacuation given by module 1.

6.2 Validation of Thermoporoelastic Model

The stress solution under the thermal effect solved by this thesis (combined

solution of Modules 1 and 2) was compared to the published stress solution in the

formation-heating case of Zhai et al. (2009). The input parameters for the test case are given in Table 6.2. Zhai et al.'s solution is the partially coupled thermoporoelastic stress state that is solved in 1D, whereas this thesis uses a 2D model which has much fewer nodes to compromise computational requirements. Therefore, minor differences are present in the comparison of the two solutions.

Figure 6.2 shows the effective radial and tangential stresses at the wellbore wall under the formation-heating effect for 100 minutes, and the isothermal condition. The left plot is generated using the stress solution in this thesis, and the right plot is the stress solution published by Zhai et al. (2009). The two plots show good agreement and similar characteristics.
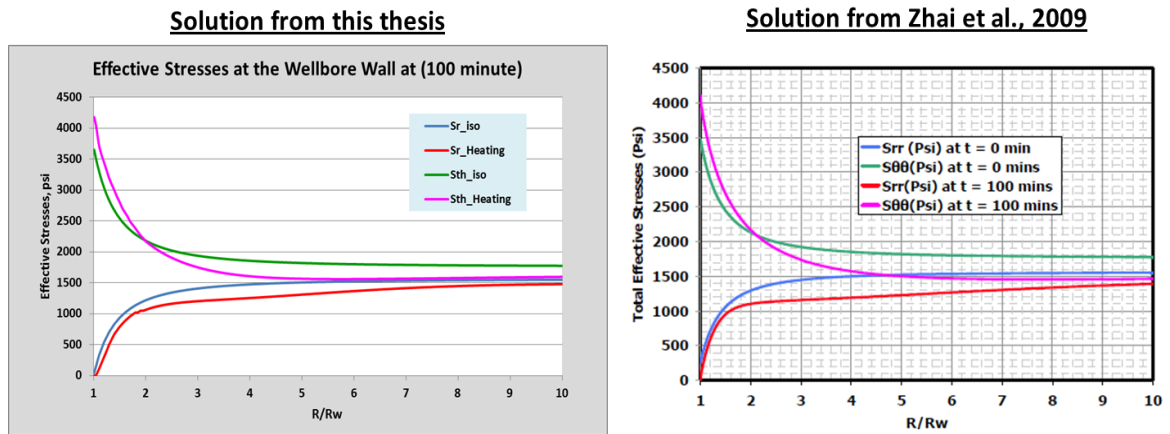
Figure 6.2 – Partially coupled thermoporoelastic stress solutions in radial and tangential direction of the test case in Table 6.2. Left plot is from this thesis (combined Module 1 and 2 solutions). Right plot is from Zhai et al. (2009). Both plots show similar response of thermoporoelastic stress. Minor differences at near-wellbore solutions are from different numerical method and different in element size.

Table 6.2 - Input parameters for validation of
the partially coupled thermoporoelastic stress-state solution.

Parameters	Abb.		Units
Undrained Poisson's Ratio	ν_u	0.33	
Drained Poisson's Ratio	ν	0.25	
Maximum Horizontal In-situ Stress	S_H	4100	psi
Minimum Horizontal In-situ Stress	S_h	3900	psi
Vertical In-situ Stress	S_v	5000	psi
Formatoin Pressure	P_f	2340	psi
Young's Modulus of Formation	E	1.00E+06	psi
Formation Porosity	ϕ	0.25	
Formation Fluid Mobility	α	7.66E-08	darcy/cp
Formation Thermal Diffusion	k_T	9.50E-04	m2/s
Volumetric Expansion of Solid	$\alpha_{T,s}$	2.70E-05	1/F
Volumertirc Expansion of Pore Fluid	$\alpha_{T,f}$	2.78E-04	1/F
Formation Temperature	T_f	75	F
Wellbore Temperature	T_w	132	F

Following the literature review, formation heating exposes the wellbore wall to compressive failure (wellbore collapse), but increases wellbore fracture resistance. Formation cooling gives the opposite results. Figure 6.3 shows the Drucker-Prager failure indices at the wellbore wall solved by this thesis. The Drucker-Prager failure index (Section 3.4.1) represents the rock compressive failure, which implies wellbore collapse potential. In Figure 6.3, three cases using input parameters from Table 6.2 are presented: isothermal (blue), heating for 10 hours (red), and cooling for 10 hours (green). From Figure 6.3, heating reduces the failure index at the near-wellbore region; this raises the wellbore collapse potential (more likely to fail under compressive mode).

Conversely, the cooling increases the failure index at the near-wellbore region; this helps prevent wellbore collapse. These same conclusions were reached by all reviewed literature investigating thermal effects at the wellbore wall.
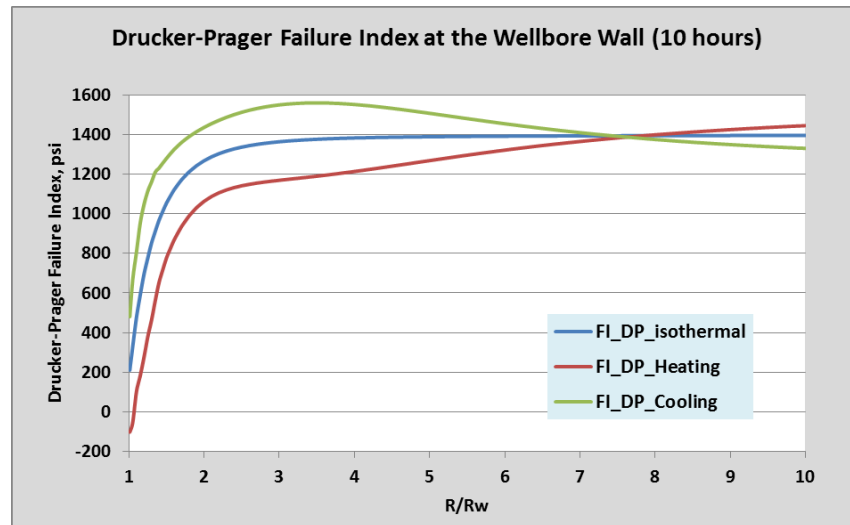
Figure 6.3 – Drucker-Prager failure indices at the wellbore wall from this thesis using the test case in Table 6.2 but at 10 hours: heating increases wellbore collapse potential; cooling reduces wellbore collapse potential.

For fracture failure, Figure 6.4 shows the effective tangential stresses at the wellbore wall. The cases are again isothermal (blue), heating for 10 hours (red), and cooling for 10 hours (green). The heating helps increase wellbore fracture resistance, whereas the cooling poses the opposite effect. Again, the same conclusions were published in the literature.

Effective Tangential Stresses at the Wellbore Wall (10 hours)
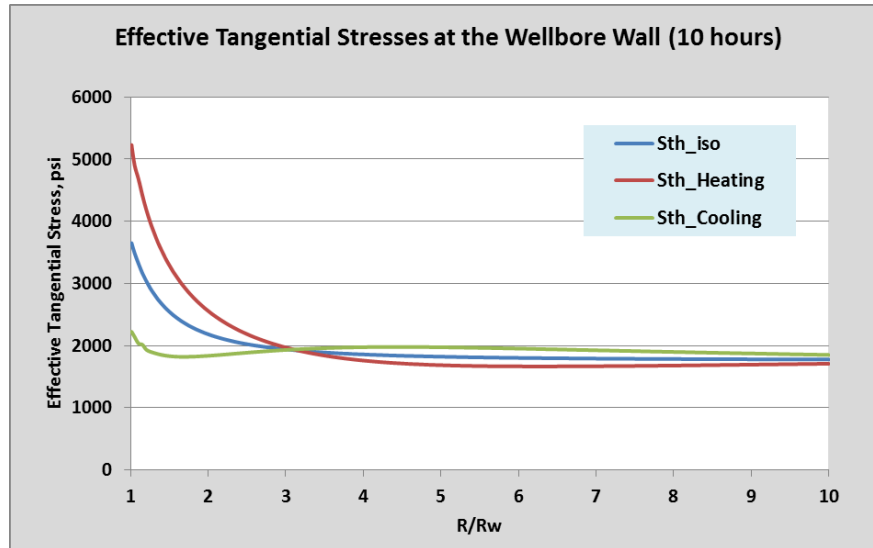
Figure 6.4 – Effective tangential stresses which represent tensile failure indices at the wellbore wall from this thesis using the test case in Table 6.2 but at 10 hours: heating increases wellbore fracture resistance; cooling reduces it.

CHAPTER VII

RESULTS AND DISCUSSIONS

Thermal effects on bottomhole rock drillability were investigated using the Drucker-Prager failure index and the tensile failure index. The first failure index represents the likelihood of rock failure under the compressive mode as a result of a vertical bit load. The latter failure index represents the likelihood of rock failure under the tensile mode in the tangential direction as a result of a bit rotation. Because the scope of this thesis was to study the thermal effects on the rock drillability, the Drucker-Prager and tensile failure indices are the main interests.

The input parameters for shale formation were selected from the works of Lee and Ghassemi (2009), Zhai et al. (2009), and Nguyen et al. (2010). The heating case had a drilling-fluid temperature that was 50°F higher than the formation temperature; the cooling case had a drilling-fluid temperature that was 50°F lower than formation temperature. Table 7.1 shows the input parameters of three cases in this simulation: base case, reduced solid matrix thermal expansion, and increased formation permeability.

Three types of plots were used to present the solutions at the bottomhole area: 2D contour, line plot along the near-bottomhole surface in radial direction, and line plot below the bottomhole in the vertical direction. The definitions and interpretations of each plot are presented in Figure 7.1.

Table 7.1 – Input parameters for numerical simulation of thermoporoelastic model.

Pressure and Temperature MAIN VARIABLES		Base Case	Case 1	Case 2
Original Formation Temperature [F]	Tf0 =	200	200	200
Original Formation Pore Pressure [psi]	Pf0 =	2000	2000	2000
Wellbore Temperature [F]	Tw =	150 or 250	150 or 250	150 or 250
Wellbore Pressure [psi]	Pw =	2000	2000	2000
Stress and Rock Failure Variables				
Maximum Horizontal Stress (psi)	SH =	5000	5000	5000
Minimum Horizontal Stress (psi)	Sh =	5000	5000	5000
Vertical Stress (psi)	Sv =	7000	7000	7000
Point-Load Weight-on-Bit (psi)	WOB =	8000	8000	8000
Rock Cohesion Factor (psi)	C0 =	500	500	500
Rock Friction Angle (degrees Angle)	ω =	30	30	30
Global and FEM/FDM Dimensions				
Wellbore Radius [ft]	rw =	1	1	1
Well Depth [rw]	z_rw_well =	10	10	10
Depth of Investigation Below Bottomhole [rw]	z_rw_investigate =	10	10	10
Depth of Investigation From Wellbore [rw]	r_rw_investigate =	20	20	20
Element Size in z-Direction [rw]	esize_z_rw =	0.1	0.1	0.1
Element Size in r-Direction [rw]	esize_r_rw =	0.1	0.1	0.1
FEM/FDM Simulatoin Parameters				
Time Increment [sec]	dt =	2	2	2
Crank-Nicholson Time Ratio	θ =	0.5	0.5	0.5
Boundary Types				
Pressure Boundary at Wellbore Wall	P_well_boundary =	impermeable	impermeable	impermeable
P and T at Top Boundary	TP_top_boundary =	zero-flux	zero-flux	zero-flux
Thermal Properties				
Formation Bulk Thermal Conductivity [btu/hr-ft-F]	k_thermal =	1.9	1.9	1.9
Formation Bulk Density [lbm/ft3]	D_bulk =	142.12	142.12	142.12
Formation Bulk Specific Heat Capacity [btu/lbm-F]	C_Bulk =	0.2	0.2	0.2
Convective Heat Transfer Coefficient [btu/hr-F]	h =	0	0	0
Geomechanic Properties				
Young Modulus of Rock [psi]	E =	1.00E+06	1.00E+06	1.00E+06
Drained Poisson Ratio	V =	0.25	0.25	0.25
Undrain Poisson Ratio	Vu =	0.33	0.33	0.33
Biot Constant	alpha =	1	1	1
Thermal Expansion Properties				
Solid Matrix Thermal Expansion [1/F]	alpha_Tm =	2.70E-05	1.00E-05	2.70E-05
Pore Fluid Thermal Expansion [1/F]	alpha_Tf =	2.80E-04	2.80E-04	2.80E-04
Fluid Flow Properties				
Formation Permeability [md]	k_f =	0.0001	0.0001	10
Formation Porosity	phi =	0.2	0.2	0.2
Pore Fluid Viscosity [cp]	mu =	1	1	1
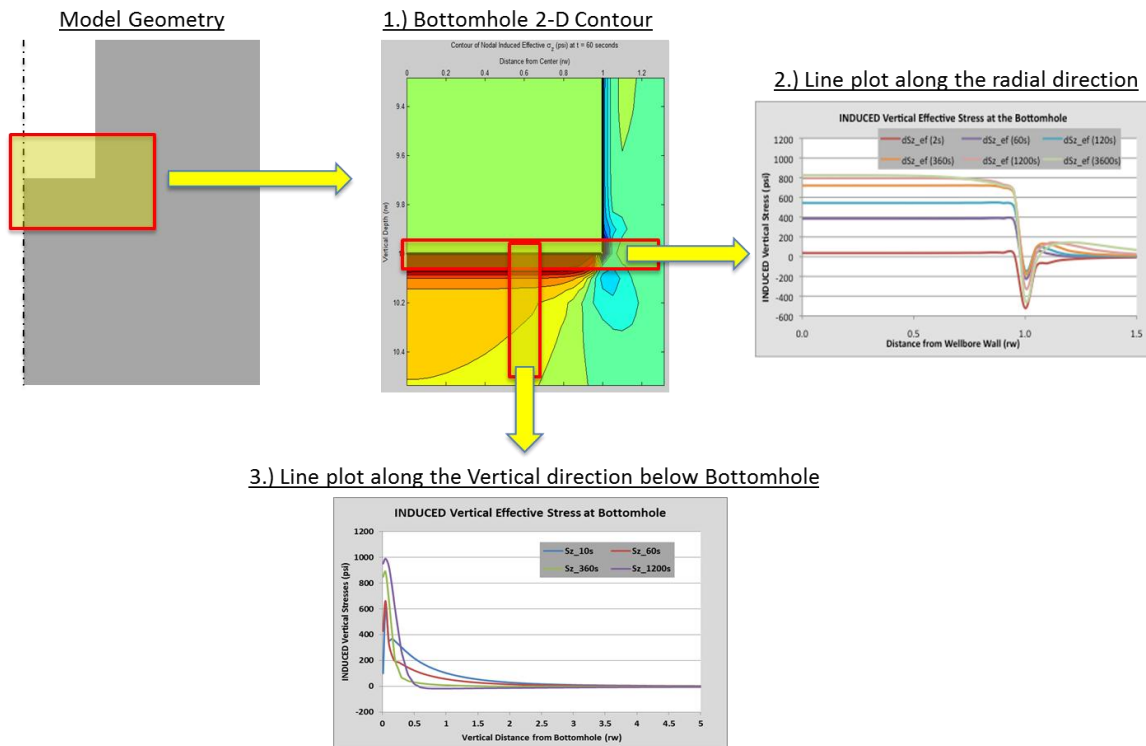
Figure 7.1 – Three types of solution plots used in this section and their definition: 1.) a contour plot shows results at the bottomhole area, 2.) a line plot shows results near the bottomhole surface along the radial direction starting from well center to 1.5's wellbore radii, 3.) a line plot shows results below the bottomhole datum.

7.1 Formation Cooling and Heating

The base case investigated the 50°F formation cooling and 50°F formation heating cases. The rock-breaking activity at the bit/formation interface was dynamic. The exposure time of the formation to drilling fluid before breaking by a drill bit was short. Therefore, the exposure time of 10 seconds (equivalent to ROP of about 20 ft/hr) was selected to examine the effects of drilling fluid temperatures on rock drillability.

Figure 7.2(a) shows of heat conduction at 10 seconds for the formation-heating and formation-cooling cases on the induced temperature inside the formation below the

bottom of the hole. The induced temperatures caused pore pressure to increase in the heating case and to decrease in the cooling case. Figure 7.2(b) shows the induced pore pressure inside the formation below the bottom of the hole at 10 seconds. Figure 7.3(a) and 7.3(b) are the 2D contours of the induced temperature and the induced pore pressure at 10 seconds for the formation-cooling cases. The travel distances and magnitudes of the induced pore pressure largely depend on formation properties such as formation permeability, thermal conductivity, and the pore-fluid thermal expansion.

(a)

(b)
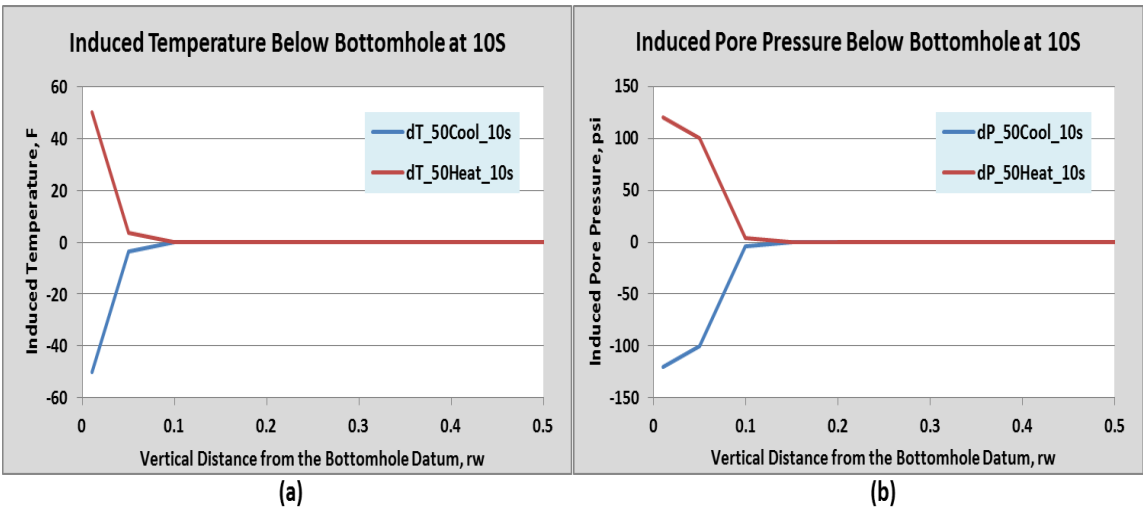
Figure 7.2 – Line plots of solutions below the bottomhole datum for 50°F cooling and 50°F heating case at 10 seconds. (a) Induced temperature below bottomhole. (b) Induced pore pressure below bottomhole.
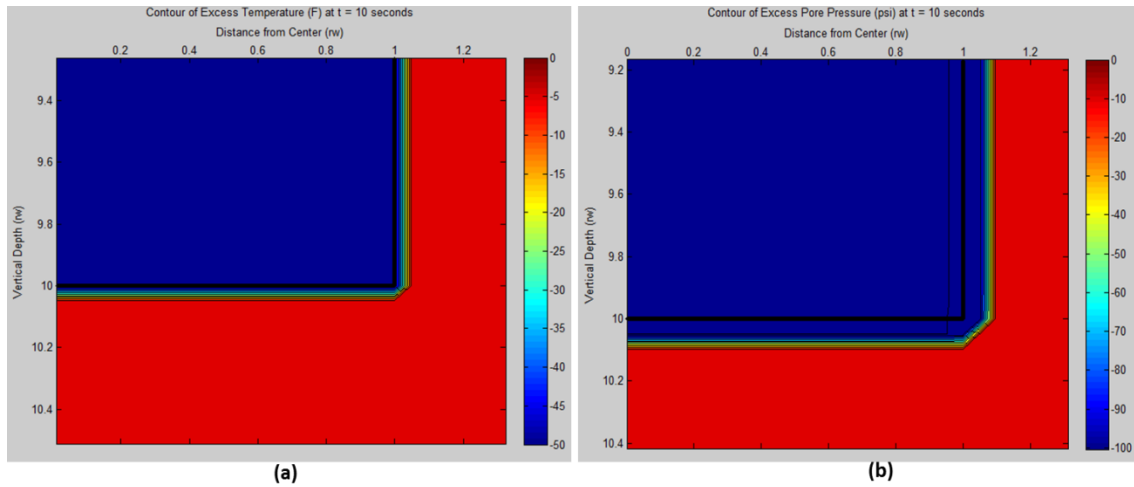
Figure 7.3 – Two-dimensional contours for 50°F-cooling case at 10 seconds.
(a) Contour of induced temperature at the bottomhole area. (b) Contour of induced pore pressure at the bottomhole area.

The induced temperature and pore pressure from the temperature difference between the drilling fluid and the formation led to changes of the bottomhole stress state. The effects of the induced temperature and pore pressure on formation effective stresses were opposite. In the cooling case, a reduction of the formation temperatures caused the effective stress to reduce (become less compressive), whereas a reduction of the pore pressure caused the effective stress to increase (become more compressive). Major factors affecting which effect will be dominant are wellbore boundary conditions, thermal expansion of the solid matrix, and thermal expansion of the pore fluid. Moreover, as will be shown later, the thermal effect is also time-dependent.

Figure 7.4 shows the thermoporoelastic stresses on the cylindrical axes near the bottomhole surface along the radial direction from the well center for the 50°F formation cooling and 50°F formation heating cases at 10 seconds. The induced temperature and

pore pressure in cooling case caused reductions of effective stresses in the radial and tangential directions, whereas the vertical effective stress increased. The rise in vertical effective stress on formation cooling must balance with the pore pressure drop, while the wellbore pressure remains constant. Moreover, there was no displacement constraint at the wellbore wall boundary (the formation was free to expand into wellbore); therefore, no thermal stress in vertical direction occurred at the wellbore boundary. The heating case resulted in the opposite effects. Note that the vertical stress peak at 0.6 wellbore radii (rw) was from the load of WOB, and high concentrated stresses developed at the well corner, which is also found in the work of Deily and Durelli (1958).
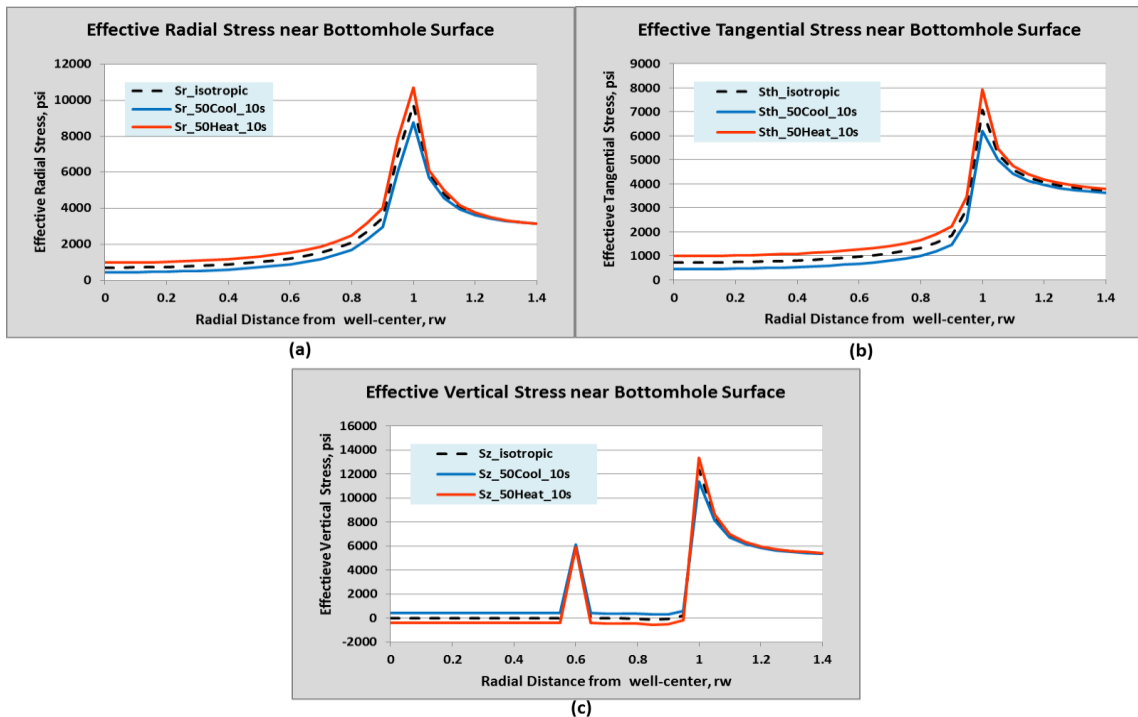
Figure 7.4 – Line plots for thermoporoelastic stress solutions near the bottomhole surface of 50°F-cooling and 50°F-heating cases at 10 seconds. (a) Effective radial stresses. (b) Effective tangential stresses. (c) Effective vertical stresses.

For completion, the thermoporoelastic stresses in Figure 7.4 were transformed into the principal directions and presented in Figure 7.5. Note that the principal directions are different from the cylindrical-axes directions, reflecting the development of shear stress at the bottomhole corner.
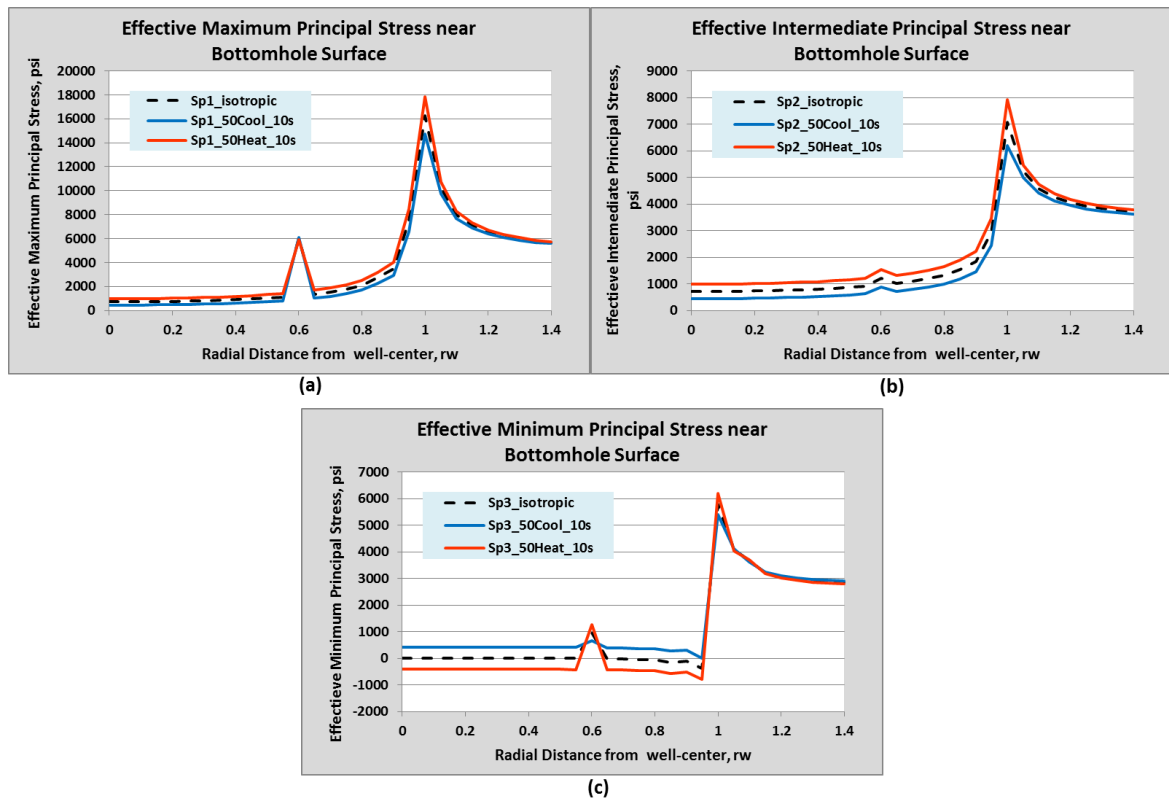
Figure 7.5 – Line plots for thermoporoelastic stress solutions near the bottomhole surface of 50°F -cooling and 50°F -heating cases at 10 seconds. (a) Effective maximum principal stresses. (b) Effective intermediate principal stresses. (c) Effective minimum principal stresses.

To investigate the thermal effect on the bottomhole-rock drillability, the Drucker-Prager failure index and the tensile failure index in tangential direction were studied.

The rock-breaking mechanisms at the bit/formation interface are governed by both rock compressive failure and rock tensile failure. The Drucker-Prager failure index relates to the likelihood of rock failure in the compressive mode, whereas the tensile failure index relates to rock failure potential in tension. More failure indices indicate less possibility of failures or less rock drillability.

Figure 7.6 and 7.7 show the Drucker-Prager failure indices and the tangential tensile failure indices near the bottomhole surface for the 50°F formation-cooling and 50°F formation-heating cases respectively at 10 seconds. Rock breaking in this model occurred at 0.6 rw from the well center, which was the location of the vertical WOB load.

In Figure 7.6, the formation cooling led to a reduction of the Drucker-Prager failure index below the bit tooth (0.6 rw from well center). This indicates that the *formation-cooling makes rock below the bit tooth becomes more drillable* (more potential to fail under compressive load). In this particular input parameters, the 50°F formation-cooling causes the Drucker-Prager failure index of the rock below the bit tooth to decrease from -355 psi to -707 psi, which means the rock is twice drillable in 50°F formation-cooling comparing to isothermal case. Conversely, the heating effect caused the Drucker-Prager failure index to increase; thus, rock below the bit tooth was less drillable (less potential to fail under compressive load).

In Figure 7.7, the formation cooling reduced the tangential tensile failure indices across the whole bottomhole area. This implies that the bottomhole rocks have more failure potential in tension, or the bottomhole rocks are more drillable in the direction of

bit rotation under formation-cooling conditions. On the other hand, formation-heating increases the tangential tensile-failure index; therefore, heating leads to less drillable rocks at the bottom of the hole. This same conclusion is also valid for the tensile failure in the radial direction since the effective stress in the radial and tangential directions have the same response to the temperature as shown in Figure 7.4(a) and 7.4(b).
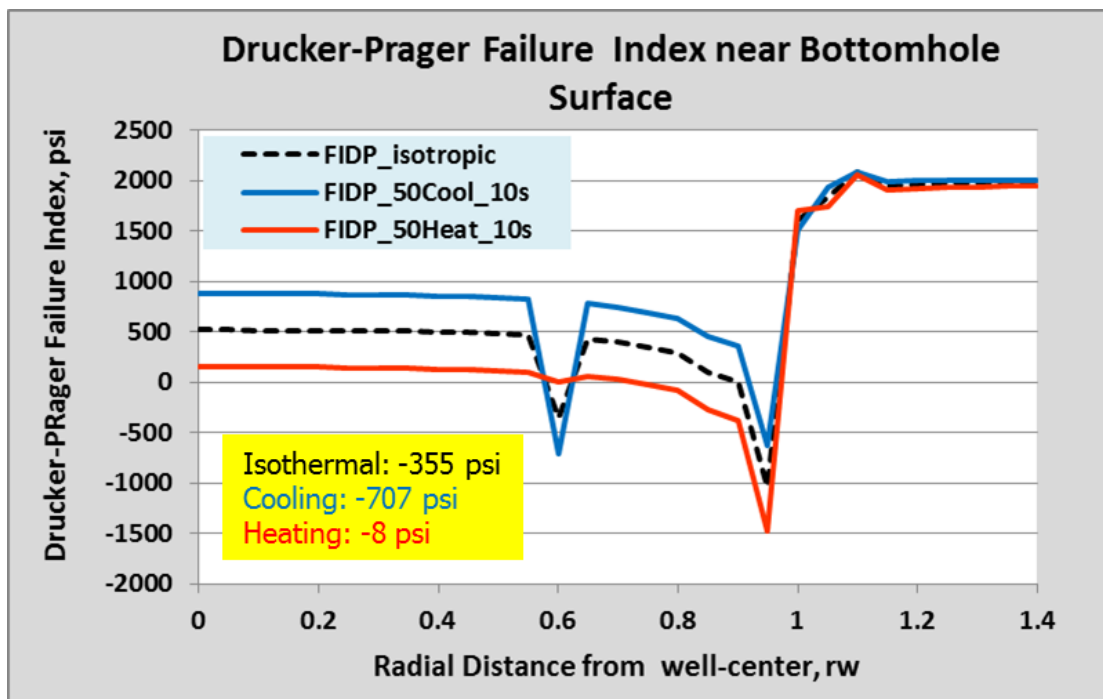
Figure 7.6 – Drucker-Prager failure indices near the bottomhole surface at 10 seconds. The failure indices imply potential of compressive rock failure. Vertical WOB is applied at 0.6 rw from well center. The formation-cooling helps increase rock drillability in compressive-failure mode at the formation below the WOB load, whereas formation-heating provides opposite impact.
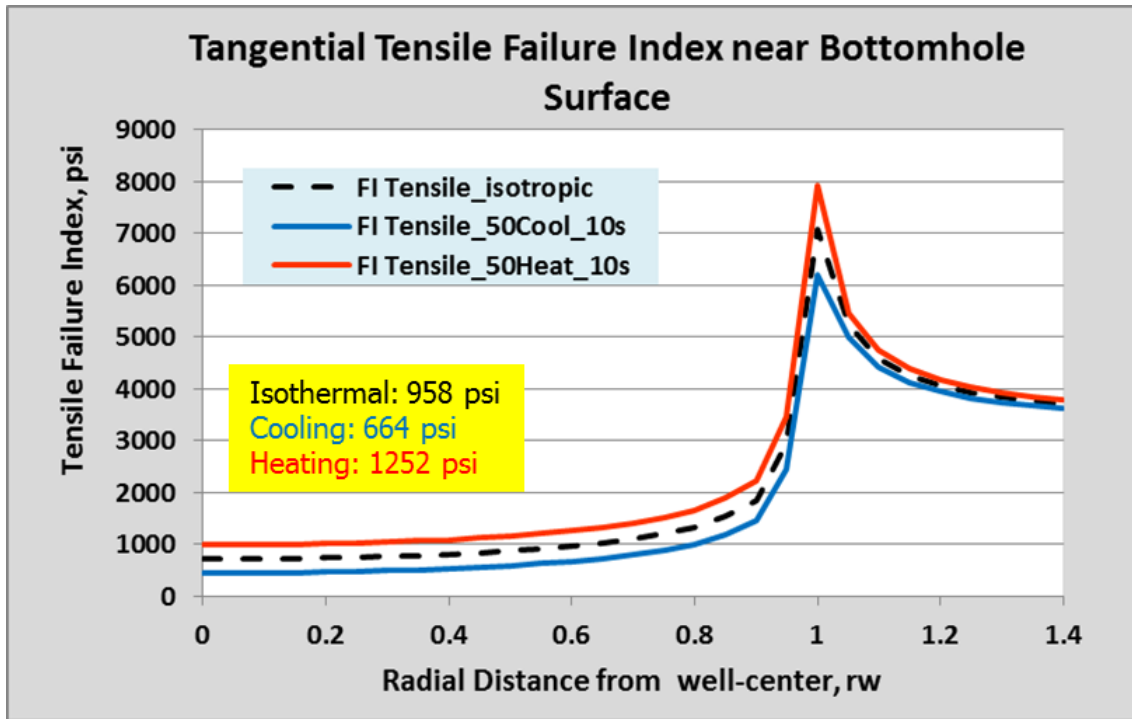
Figure 7.7 – Tangential tensile failure indices near the bottomhole surface at 10 seconds. The failure indices imply potential of tensile rock failure. The formation-cooling helps increase rock drillability in tensile-failure mode. The formation-heating gives opposite effects.

7.2 Impacts of Exposure Time on Thermal Effects

Figures 7.8(a) and 7.8(b) show induced temperatures and induced pore pressures at various exposure times of 50°F formation cooling using base-case parameters. The induced effects traveled into the formation as exposure time increased. The impermeable wellbore and low permeability caused the peaks of induced pore pressure to occur right below the bottomhole surface (at zero distance below bottom of the hole) and slowed the diffusion of the induced effect into the formation.
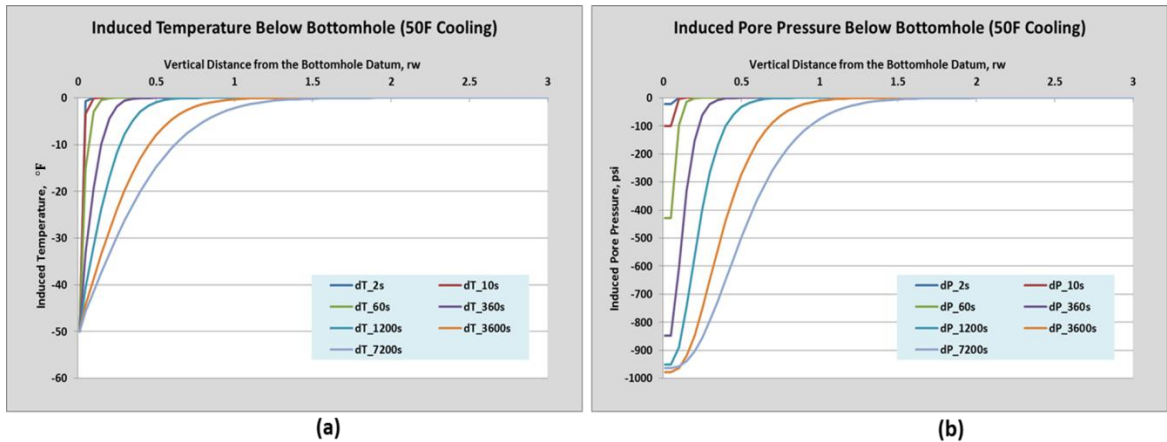
Figure 7.8 – Line plots below the bottomhole surface for 50°F formation cooling at various exposure times. (a) Induced temperature. (b) Induced pore pressure.

The Drucker-Prager and tangential tensile failure indices at various exposure times are presented in Figures 7.9 and 7.10. Figure 7.9 shows that the cooling effect on rock drillability below the bit tooth (0.6 rw) was time-dependent as the Drucker-Prager failure index below the bit tooth slowly increased with exposure time. The same trend was found in the tangential tensile failure index. At very late time, the tensile failure index continued to increase such that it rose over the isotropic case. These findings reveal that the cooling effect that helps promote rock drillability loses its effectiveness with time as the pore pressure decreases, causing effective stresses to increase. As a result, rock strength increases with time.
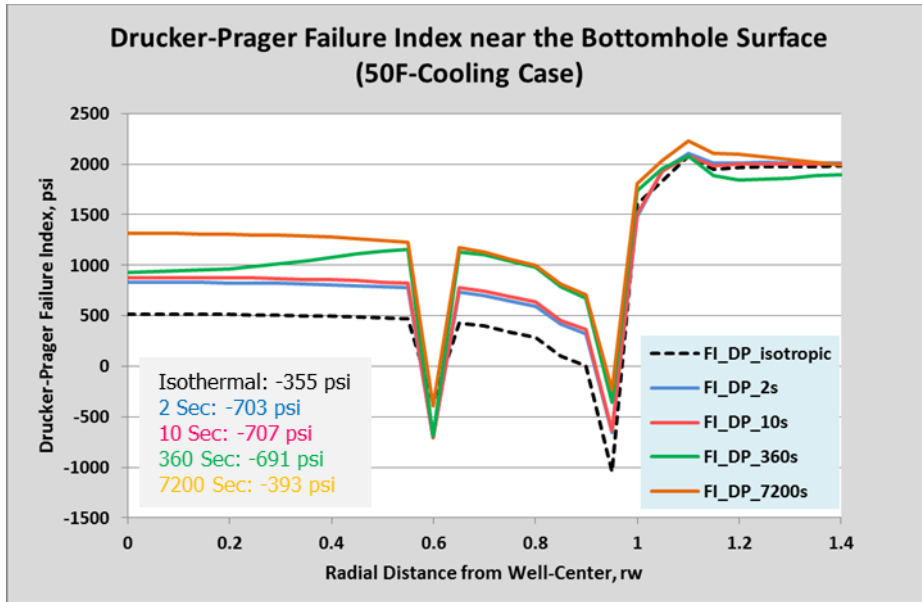
Figure 7.9 – Drucker-Prager failure indices near the bottomhole surface for 50°F cooling case at various exposure times. The formation-cooling effects on rock compressive strength diminish slowly with exposure time.
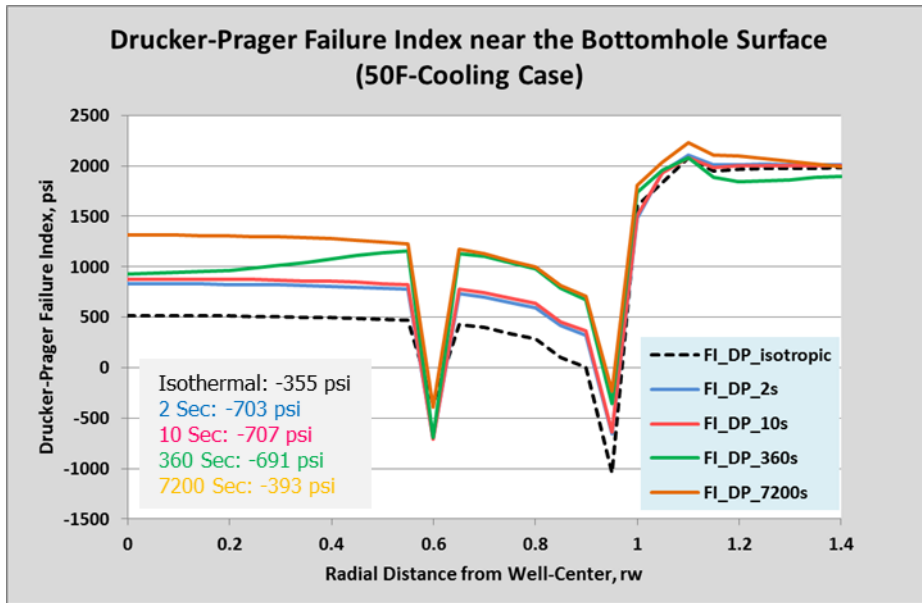
Figure 7.10 – Tangential tensile failure indices near the bottomhole surface for 50°F cooling case at various exposure times. The formation-cooling effects on rock tensile strength diminish slowly with exposure time.

7.3 Impacts of Formation Properties on Thermal Effects

This section reviews impacts on the thermoporoelastic effect in relation to formation properties, solid matrix thermal expansion and formation permeability. The input parameters representing these different cases are given in Table 7.1: Case 1 for reduced solid matrix thermal expansion and Case 2 for increased formation permeability. Their results are compared with the base case.

Figures 7.11, 7.12, and 7.13 show the Drucker-Prager failure indices right below the bit tooth (at 0.6 rw) of different input parameters for 50°F formation-cooling at 10 seconds, 360 seconds, and 1200 seconds. These figures show that the failure index is formation-properties dependent and each has different sensitivity to the exposure time.

At early time (10 seconds and 360 seconds), Case 1 of the reduced solid thermal expansion gave a smaller cooling effect that increases rock drillability than the base-case or Case 2 of the increased permeability. Having less solid matrix thermal expansion as in Case 1, the thermal stress in the solid matrix was less responsive to the temperature decrease, whereas the reduced pore pressure remained the same. This led to higher effective stresses than in the base case. As a result, the rock was stronger in terms of compressive strength (or less compressively drillable) in formations that have low solid matrix thermal expansion.
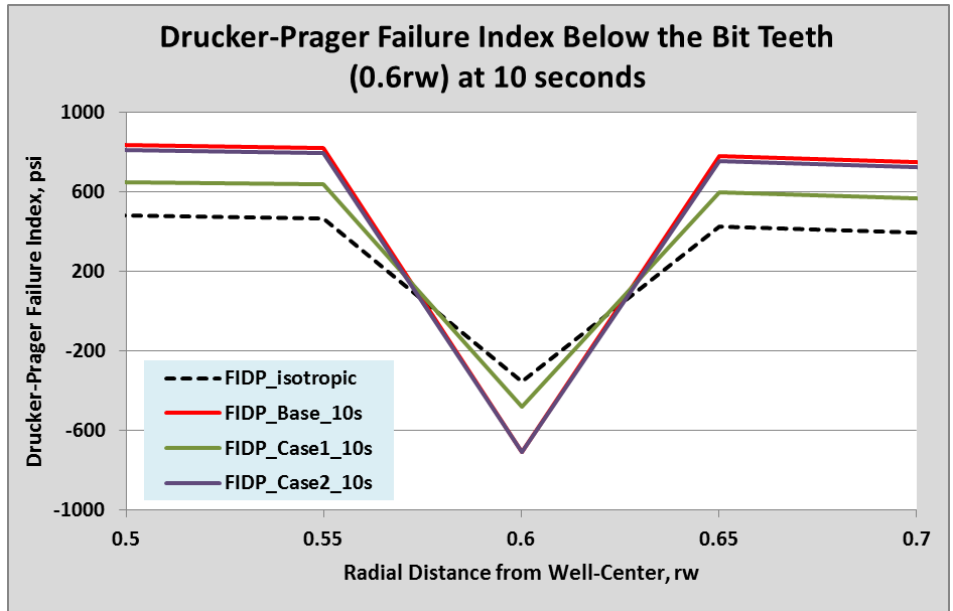
Figure 7.11 – Drucker-Prager failure indices below the bit tooth at 10 seconds for 50°F cooling. Case 1 represents reduced solid matrix thermal expansion. Case 2 is increased permeability. Case 1 presents less formation-cooling effect than base case.
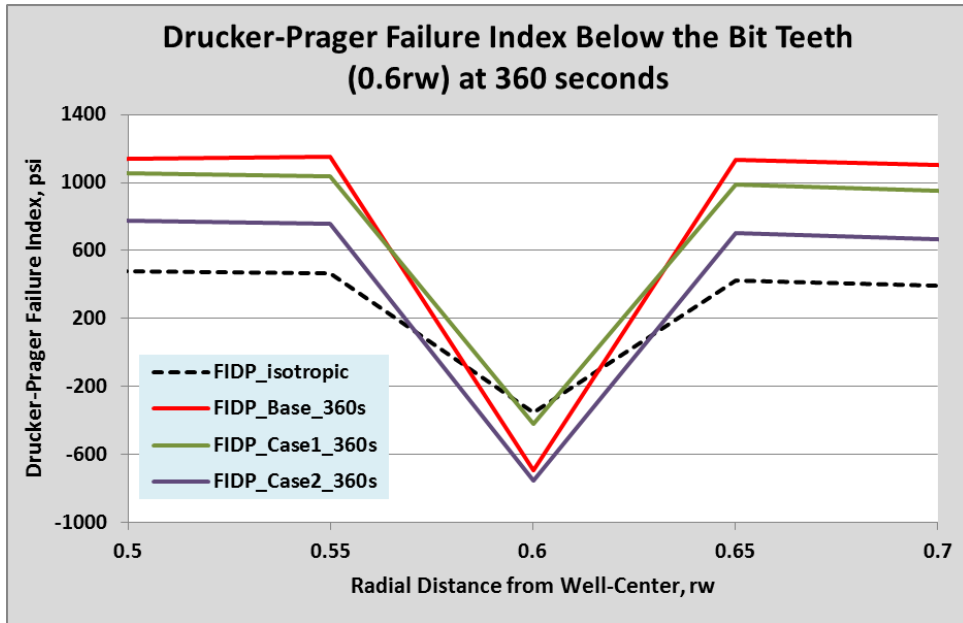
Figure 7.12 – Drucker-Prager failure indices below the bit tooth at 360 seconds for 50°F cooling. Case 1 represents reduced solid matrix thermal expansion. Case 2 is increased permeability. Case 1 and base case present diminish thermal effect with time. Case 2 presents less sensitivity of formation-cooling effect to exposure time.
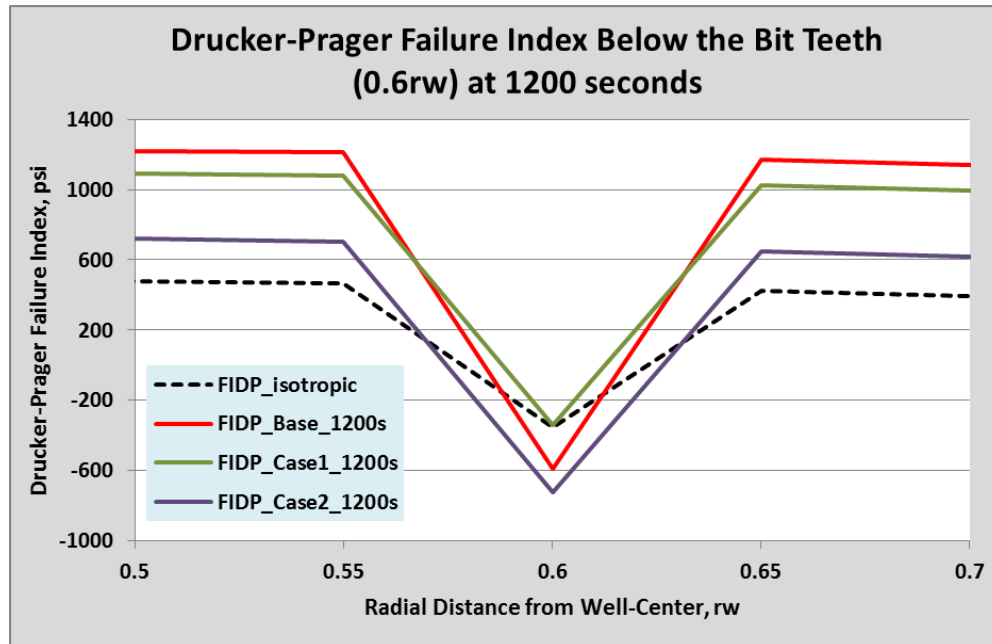
Figure 7.13 – Drucker-Prager failure indices below the bit tooth at 1200 seconds
for 50°F cooling. Case 1 represents further reduced solid matrix thermal expansion from
360 second. Case 2 is increased permeability. Case 1 and base case present further
diminish thermal effect with time rom 360 seconds. Case 2 presents no change of
thermal effect from 10 seconds and 360 seconds.

As exposure time increased from Figure 7.11 to 7.13, the base case and Case 1 of
the reduced solid matrix thermal expansion had less cooling effect to promote rock
drillability, whereas the cooling thermal effect in Case 2 of the increased permeability
was nearly independent of exposure time. As mentioned earlier, an increase of the near-
bottomhole failure indices (less rock drillability) in the base case was the result of near-
bottomhole pore pressure decreasing with time under the cooling effect, as shown in
Figure 7.8(b). This pore-pressure reduction led to an increase of effective stresses;
therefore, rock compressive strength or the Drucker-Prager failure index increased. With
higher formation permeability in Case 2, the constant pore pressure from the far-field

98

boundary could travel faster through the formation and help minimize the near-bottomhole pore pressure reduction from the cooling effect. Figure 7.14 presents the induced pore pressures in low-permeability (base case) and high-permeability (Case 2) formations. Figure 7.14 shows that the reduction of pore pressure in the high-permeability formation was much smaller than in low-permeability formation. At late time, induced pore pressure in the high-permeability case remained relatively constant, whereas it continued to increase in the low-permeability case.
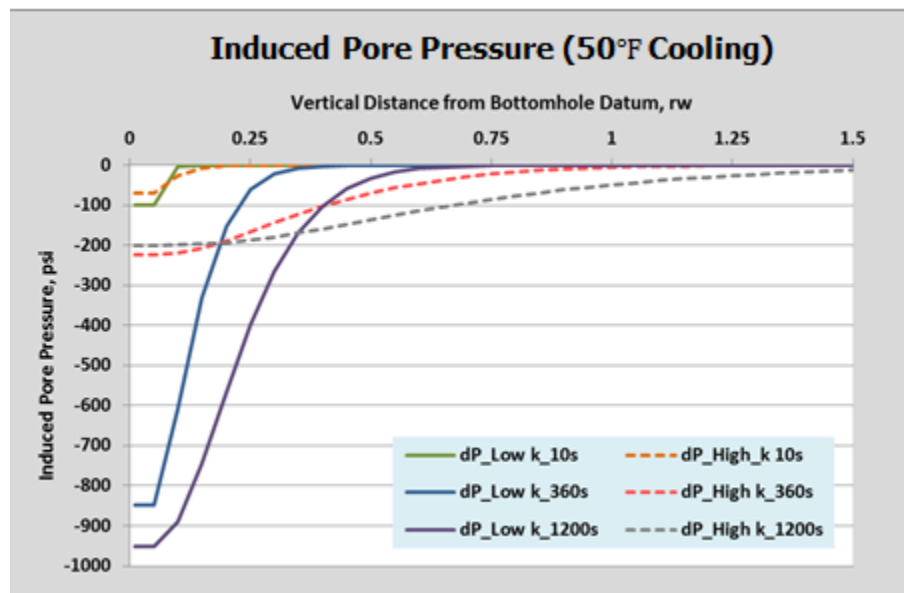
Figure 7.14 – Induced pore pressure in low and high permeability. In high permeability formation, the induced effect on pore pressure dissipates into far-field formation much faster than in low permeability formation. As a result, induced pore pressure right below the bottomhole in low permeability formation is higher than in low permeability formation.

99

CHAPTER VIII

CONCLUSIONS AND RECOMMENDATIONS

8.1 Conclusions

- Drilling fluid temperature affects rock drillability at the bit/formation interface in shale formations. The formation cooling leads to more rock drillability below the bit teeth, whereas formation heating results in less-drillable rock at the same location. The finding of thermoporoelastic effects helps explain the high-temperature/high-pressure (HTHP) drilling incidents in that HTHP wells drilled with water-based fluid gave superior rates of penetration than HTHP wells drilled with oil-based fluid. Because the water-based fluid helps cool the bottomhole formation better than the oil-based fluid, rocks below the bit in wells drilled with water-based fluid are more drillable. This finding helps encourage the use of water-based drilling fluid to potentially promote bit-drilling efficiency.

- Thermoporoelastic effects are time dependent. With the input parameters for shale formations used in this thesis, the cooling effects at the bit/formation interface tend to decrease with time. Therefore, the cooling effect leading to more rock drillability is optimum at the early time. This time period matches well with the requirement of rock-breaking activity in bit drilling, which is dynamic and occurs very fast such that the formation below the bit is exposed to the drilling fluid for a short time before breaking.

- Thermoporoelastic effects are affected by formation properties such as formation permeability and solid-matrix thermal expansion. In high-permeability

formations, the cooling effect helps promote more rock drillability than in low-permeability formations, and the effect is less sensitive to exposure time. In formations with low solid-matrix thermal expansion, the cooling effect on rock drillability is less than in formations with high solid-matrix thermal expansion. The difference in solid-matrix thermal expansion doesn't affect the sensitivity of the cooling effects.

- At the wellbore wall, formation cooling helps reduce wellbore collapse potential but increases wellbore fracture likelihood. Conversely, formation heating leads to more wellbore fracture resistance, but the wellbore wall is exposed to a greater possibility of wellbore collapse. The drilling engineer needs to consider the thermal effects when designing the mud-weight window.

8.2 Recommendations

- The rock model in this thesis is assumed to comply with the thermoporoelastic theory. Real rocks found in drilling operations present non-linear and plastic deformation to some degree. More accurate prediction of thermal effects on the bit/formation interface can be accomplished by incorporating the non-linear behaviors and plasticity theory of materials into the model.

- This thesis decouples the deformation effect from pore pressure change and ignores the heat convection. These assumptions limit the applicability of the solution given by this model to shale formations with low compressibility.

Incorporating fully coupled governing relations will help expand the application of the model.

- Because the thermal effects are dependent on formation properties, more cases with different formation properties need to be studied.

- The actual boundary condition at the wellbore wall is not fully impermeable, as assumed in this thesis. The pressure interaction at the wellbore wall lies between two extreme cases, which are and impermeable wellbore and a permeable wellbore, depending on the drilling conditions and formation properties. To cover all possible cases, a study of the permeable wellbore condition needs to be performed.

REFERENCES

Bilgesu, I., Sunal, O., Tulu, I.B. et al. 2008. Modeling Rock and Drill Cutter Behavior. Paper ARMA-08-342 presented at the The 42nd U.S. Rock Mechanics Symposium (USRMS), San Francisco, CA, 29 June-2 July 2008.

Block, G. and Jin, H. 2009. Role of Failure Mode on Rock Cutting Dynamics. Paper SPE-124870-MS presented at the SPE Annual Technical Conference and Exhibition, New Orleans, Louisiana, 4-7 October 2009. doi: 10.2118/124870-ms.

Chang, D., Shen, Z., Huang, Z. et al. 2012. Analysis of 3D In-situ Differential Stress Influence on Bottom-hole Stress Field. State Key Laboratory of Petroleum Resource and Prospecting, China University of Petroleum, Beijing, China.

Chen, G. and Ewy, R.T. 2004. Thermoporoelastic Effect on Wellbore Stresses in Permeable Rocks. Paper ARMA-04-467 presented at the Gulf Rocks 2004, the 6th North America Rock Mechanics Symposium (NARMS), Houston, Texas, 5-9 June 2004.

Chen, G. and Ewy, R.T. 2005. Thermoporoelastic Effect on Wellbore Stability. *SPE Journal* **10** (2): 121-129. doi: 10.2118/89039-pa.

Deily, F.H. and Durelli, A.J. 1958. Bottom-Hole Stresses in a Well Bore. Paper SPE 1095-G available from SPE, Richardson, Texas. doi: 10.2118/1095-g.

Diek, A., White, L., Roegiers, J.-C. et al. 2011. A Fully Coupled Thermoporoelastic Model for Drilling in Chemically Active Formations. Paper ARMA-11-406 presented at the 45th U.S. Rock Mechanics / Geomechanics Symposium, San Francisco, California, 26-29 June 2011.

Falcao, J.L. 2001. Drilling in High-Temperature Areas in Brazil: A Wellbore Stability Approach. Paper SPE 69516 presented at the SPE Latin American and Caribbean Petroleum Engineering Conference, Buenos Aires, Argentina, 25-28 March 2001. doi: 10.2118/69516-ms.

Farahani, H.S., Yu, M., Miska, S.Z. et al. 2006. Modeling Transient Thermo-Poroelastic Effects on 3D Wellbore Stability. Paper SPE-103159-MS presented at the SPE Annual Technical Conference and Exhibition, San Antonio, Texas, USA, 24-27 September 2006. doi: 10.2118/103159-ms.

Gadde, M.M., and Rusnak, J.A. 2008. Applicability of Drucker-Prager Failure Criterion to Estimate Polyaxial Rock Strength. Paper ARMA-08-137 presented at the 42nd U.S. Rock Mechanics Symposium (USRMS), San Francisco, CA, 29 June-2 July 2008.

Gonzalez, M.E., Bloys, J.B., Lofton, J.E. et al. 2004. Increasing Effective Fracture Gradients by Managing Wellbore Temperatures. Paper IADC/SPE 87217 presented at the IADC/SPE Drilling Conference, Dallas, Texas, 2-4 March 2004. doi: 10.2118/87217-ms.

Hareland, G. and Nygaard, R. 2007. Calculating Unconfined Rock Strength from Drilling Data. Paper ARMA-07-214 presented at the 1st Canada - U.S. Rock Mechanics Symposium, Vancouver, Canada, 27-31 May 2007.

Hettema, M.H.H., Boströ, M.B., and Lund, T. 2004. Analysis of Lost Circulation During Drilling in Cooled Formations. Paper SPE 90442 presented at the SPE Annual Technical Conference and Exhibition, Houston, Texas, 26-29 September 2004. doi: 10.2118/90442-ms.

Kang, Y., Yu, M., Miska, S.Z. et al. 2009. Wellbore Stability: A Critical Review and Introduction to DEM. Paper SPE-124669-MS presented at the SPE Annual Technical Conference and Exhibition, New Orleans, Louisiana, 4-7 October 2009. doi: 10.2118/124669-ms.

Kraussman, A. 2011. The Use of WBM to Improve ROP in HTHP/Hard Rock Environment. MS thesis, Texas A&M University, College Station, Texas (May 2011).

Kurashige, M. 1989. A Thermoelastic Theory of Fluid-Filled Porous Materials. *International Journal of Solids and Structures* **25** (9): 1039-1052. doi: 10.1016/0020-7683(89)90020-6.

Lee, S.H., and Ghassemi, A. 2009. Thermo-Poroelastic Finite-element Analysis of Rock Deformation and Damage. Paper ARMA-09-121 presented at the 43rd U.S. Rock Mechanics Symposium & 4th U.S. - Canada Rock Mechanics Symposium, Asheville, North Carolina, 28 June-1 July 2009.

Lee, S.H., and Ghassemi, A. 2010. A Three-Dimensional Thermo-Poro-Mechanical Finite-element Analysis of a Wellbore on Damage Evolution. Paper ARMA-10-228 presented at the 44th U.S. Rock Mechanics Symposium and 5th U.S.-Canada Rock Mechanics Symposium, Salt Lake City, Utah, 27-30 June 2010.

Li, X. 1998. Thermoporomechanical Modeling of Inclined Boreholes. PhD dissertation, University of Oklahoma, Norman, Oklahoma.

Li, X., Cui, L., and Roegiers, J.-C. 1999. Temperature Induced Pore Pressure and Stresses and Their Potential Impacts on Wellbore Stability. A.A. Balkema. Permission to Distribute - International Society for Rock Mechanics. Paper ISRM-9CONGRESS-1999-091 presented at the 9th ISRM Congress, Paris, France, 25-28 August 1999.

Masri, M., Sibai, M., and Shao, J. 2009. Experimental Study of the Temperature Effect on the Mechanical Behaviour of Anisotropic Rock. Paper ISRM-SINOROCK-2009-040 presented at the ISRM International Symposium on Rock Mechanics - SINOROCK 2009, The University of Hong Kong, China, 19-22 May 2009.

Nawrocki, P.A. 2010. Critical Wellbore Pressure Using different Rock Failure Criteria. Paper ARMS6-2010-103 presented at the ISRM International Symposium - 6th Asian Rock Mechanics Symposium, New Delhi, India, October 23 - 27, 2010.

Nguyen, D.A., Miska, S.Z., Yu, M. et al. 2010. Modeling Thermal Effects on Wellbore Stability. Paper SPE-133428-MS presented at the Trinidad and Tobago Energy Resources Conference, Port of Spain, Trinidad, 27-30 June 2010. doi: 10.2118/133428-ms.

Nygaard, R. and Hareland, G. 2007. Application of Rock Strength in Drilling Evaluation. Paper SPE-106573-MS presented at the Latin American & Caribbean Petroleum Engineering Conference, Buenos Aires, Argentina, 15-18 April 2007. doi: 10.2118/106573-ms.

Paul, B. and Gangal, M.D. 1969. Why Compressive Loads on Drill Bits Produce Tensile Splitting in Rock. Paper SPE 2392-MS presented at the Drilling and Rock Mechanics Symposium, Austin, Texas, 14-15 January 1969. doi: 10.2118/2392-ms.

Sun, X. 2001. A New Rock/Bit Interaction Model for Rotary Drilling Process. Swets & Zeitlinger Lisse, Permission to Distribute - American Rock Mechanics Association. Paper ARMA-01-0903 presented at the The 38th U.S. Symposium on Rock Mechanics (USRMS), Washington D.C., 7-10 July 2001.

Tao, Q. and Ghassemi, A. 2010. Poro-thermoelastic borehole stress analysis for determination of the in situ stress and rock strength. *Geothermics* **39** (3): 250-259. doi: 10.1016/j.geothermics.2010.06.004.

Thosuwan, R., Walsri, C., Poonprakon, P. et al. 2009. Effects of Intermediate Principal Stress on Compressive and Tensile Strengths of Sandstones. International Society for Rock Mechanics and the University of Hong Kong. Paper ISRM-SINOROCK-2009-055 presented at the ISRM International Symposium on Rock

Mechanics - SINOROCK 2009, The University of Hong Kong, China, 19-22 May 2009.

Wang, Y., Papamichos, E., and Dusseault, M.B. 1996. Thermal Stresses and Borehole Stability. Paper A.A. Balkema. Permission to Distribute - American Rock Mechanics Association. Paper ARMA-96-1121 presented at the 2nd North American Rock Mechanics Symposium, Montreal, Quebec, Canada, 19-21 June 1996.

Wang, Y., and Wong, T.F. 1987. Finite-element analysis of two overcoring techniques for in situ stress measurements, *Int. J. Rock Mech. Min. Sci.* **24** (1): 41-52.

Wu, B., Wu, B., Zhang, X. et al. 2011. Wellbore Stability Analyses for HPHT Wells Using a Fully Coupled Thermo-Poroelastic Model. Paper SPE-144978-MS presented at the SPE Asia Pacific Oil and Gas Conference and Exhibition, Jakarta, Indonesia, 20-22 September 2011. doi: 10.2118/144978-ms.

Wu, B., Zhang, X., and Jeffrey, R.G. 2010. A Thermo-Poro-Elastic Analysis of Stress Fields around a Borehole. Paper ARMA-10-442 presented at the 44th U.S. Rock Mechanics Symposium and 5th U.S.-Canada Rock Mechanics Symposium, Salt Lake City, Utah, 27-30 June 2010.

Zhai, Z., Zaki, K.S., Marinello, S.A. et al. 2009. Coupled Thermo-Poro-Mechanical Effects on Borehole Stability. SPE-123427-MS presented at the SPE Annual Technical Conference and Exhibition, New Orleans, Louisiana, 4-7 October 2009. doi: 10.2118/123427-ms.

Zhang, J. and Roegiers, J.-C. 2005. Poroelastic Analysis of Rock Indentation Failure by a Drill Bit. Paper ARMA-05-670 presented at the The 40th U.S. Symposium on Rock Mechanics (USRMS), Anchorage, AK, 25-29 June 2005.

Zhao, X.L., and Roegiers, J.-C. 1995. A fracture mhanics approach to rock drilling. A. A. Balkema, Rotterdam. Permission to Distribute - American Rock Mechanics Association. Paper ARMA-95-0329 available from SPE, Richardson, Texas.

Zhou, S., Hillis, R., and Sandiford, M. 1996. On the Mechanical Stability of Inclined Wellbores. *SPE Drilling & Completion* **11** (2): 67-73. doi: 10.2118/28176-pa.

APPENDIX A

THE NUMERICAL FORMULATION FOR WELLBORE GEOMETRY

STRESSES SOLUTION WITH THE FOURIER-ASSISTED FINITE-ELEMENT

This appendix presents the Fourier-assisted finite-element formulation of the poroelasticity theory governing the formation stress change due to formation evacuation in vertical well drilling. The model geometry covers the formation stress changes at the bottomhole up and the wellbore wall. An actual nature of this model requires three dimensional solution which is computational expansive. Fortunately, the horizontal stress boundary can be presented in a form of the Fourier series of sine and cosine terms. By introducing the Fourier series into the finite-element technique, it reduces a computational complexity from three degree-of-freedom variables with a three dimensional geometry to three degree-of-freedom variables with a two dimensional axisymmetric geometry. The stress solution can be solved separately for each Fourier harmonic due to the linearity of the solutions.

The General Fourier Form of Solutions and Boundary Stresses

This section describes all the axisymmetric boundary loads, which are the radial boundary stress, the tangential boundary stress, the vertical boundary stress and the pore pressure. They are in a form of the full n-harmonic sine and cosine Fourier series.

Radial Boundary Stress:

$$S_r(r,\theta,z) = \sum_{n=0}^{\infty} \left[\bar{S}_r(r,z)cos(n\theta) + \bar{\bar{S}}_r(r,z)sin(n\theta) \right] \qquad \text{(A-1)}$$

Tangential Boundary Stress:

$$S_\theta(r,\theta,z) = \sum_{n=0}^{\infty} \left[\bar{S}_\theta(r,z)sin(n\theta) - \bar{\bar{S}}_\theta(r,z)cos(n\theta) \right] \qquad \text{(A-2)}$$

Vertical Boundary Stress:

$$S_Z(r,\theta,z) = \sum_{n=0}^{\infty} \left[\bar{S}_z(r,z)cos(n\theta) + \bar{\bar{S}}_z(r,z)sin(n\theta) \right] \qquad \text{(A-3)}$$

Boundary Pore Pressure:

$$P_0(r,\theta,z) = \sum_{n=0}^{\infty} \left[\bar{P}_0(r,z)cos(n\theta) + \bar{\bar{P}}_0(r,z)sin(n\theta) \right] \qquad \text{(A-4)}$$

By having the boundary loads in the Fourier series form as shown in Eqs. A-1 to A-4, the result is that all the fundamental solutions also have the same Fourier harmonic characteristic. The fundamental solutions in the Fourier series form are

Radial Displacement Solution:

$$u_r(r,\theta,z) = \sum_{n=0}^{\infty} \left[\bar{u}_r(r,z)cos(n\theta) + \bar{\bar{u}}_r(r,z)sin(n\theta) \right] \qquad \text{(A-5)}$$

Tangential Displacement Solution:

$$u_\theta(r,\theta,z) = \sum_{n=0}^{\infty} \left[\bar{u}_\theta(r,z)sin(n\theta) - \bar{\bar{u}}_\theta(r,z)cos(n\theta) \right] \qquad \text{(A-6)}$$

Vertical Displacement Solution:

$$u_Z(r,\theta,z) = \sum_{n=0}^{\infty} [\bar{u}_z(r,z)cos(n\theta) + \bar{\bar{u}}_z(r,z)sin(n\theta)] \qquad \text{(A-7)}$$

Pore Pressure Solution:

$$P(r,\theta,z) = \sum_{n=0}^{\infty} [\bar{P}(r,z)cos(n\theta) + \bar{\bar{P}}(r,z)sin(n\theta)] \qquad \text{(A-8)}$$

Note that boundary stress and displacement solution in tangential direction have negative cosine in double-bar term. This is to assist in reducing complexity of finite-element matrix formulation. The negative cosine in double-hat term helps create a symmetric property between the single-bar and double-bar terms for some finite-element matrices. This advantage will be used in a later section.

The General Fourier Form of Linear Elastic Stress and Strain

The finite-element matrix of the displacement solutions as given in Eqs. A-5 to A-7 is

$$\begin{bmatrix} u_r \\ u_\theta \\ u_z \end{bmatrix} = [H_u(r,z)] \sum_{n=0}^{\infty} \begin{bmatrix} \bar{u}_{r,n,1}(r,z)\cos(n\theta) + \bar{\bar{u}}_{r,n,1}(r,z)\sin(n\theta) \\ \bar{u}_{\theta,n,1}(r,z)\sin(n\theta) - \bar{\bar{u}}_{\theta,n,1}(r,z)\cos(n\theta) \\ \bar{u}_{z,n,1}(r,z)\cos(n\theta) + \bar{\bar{u}}_{z,n,1}(r,z)\sin(n\theta) \\ \vdots \end{bmatrix} \qquad \text{(A-9)}$$

By separating the single-bar and double-bar terms in Eq. A-9 and factoring out the sine and cosine, Eq. A-9 is simplified to

$$\begin{bmatrix} u_r \\ u_\theta \\ u_z \end{bmatrix} = \sum_{n=0}^{\infty} \{[H_u(r,z)][\overline{CSn}(\theta)][\widehat{\bar{u}_n}] + [H_u(r,z)][\overline{\overline{CSn}}(\theta)][\widehat{\bar{\bar{u}}_n}]\} \qquad \text{(A-10)}$$

where

$$[H_u] = \begin{bmatrix} h_1 & 0 & 0 & h_2 & 0 & 0 & h_3 & 0 & 0 \\ 0 & h_1 & 0 & 0 & h_2 & 0 & 0 & h_3 & 0 \\ 0 & 0 & h_1 & 0 & 0 & h_2 & 0 & 0 & h_3 \end{bmatrix} \tag{A-11}$$

$$[\overline{CSn}] = \begin{bmatrix} \cos(n\theta) & 0 & 0 & \cdots \\ 0 & \sin(n\theta) & 0 & \cdots \\ 0 & 0 & \cos(n\theta) & \cdots \\ \vdots & \vdots & \vdots & \ddots \end{bmatrix} \tag{A-12}$$

$$[\overline{\overline{CSn}}] = \begin{bmatrix} \sin(n\theta) & 0 & 0 & \cdots \\ 0 & -\cos(n\theta) & 0 & \cdots \\ 0 & 0 & \sin(n\theta) & \cdots \\ \vdots & \vdots & \vdots & \ddots \end{bmatrix} \tag{A-13}$$

$$[\hat{\bar{u}}_n] = \begin{bmatrix} \bar{u}_{r,n,1} \\ \bar{u}_{\theta,n,1} \\ \bar{u}_{z,n,1} \\ \bar{u}_{r,n,2} \\ \bar{u}_{\theta,n,2} \\ \vdots \end{bmatrix} \tag{A-14}$$

$$[\hat{\bar{\bar{u}}}_n] = \begin{bmatrix} \bar{\bar{u}}_{r,n,1} \\ \bar{\bar{u}}_{\theta,n,1} \\ \bar{\bar{u}}_{z,n,1} \\ \bar{\bar{u}}_{r,n,2} \\ \bar{\bar{u}}_{\theta,n,2} \\ \vdots \end{bmatrix} \tag{A-15}$$

It is convenient for a later calculation to define new matrices, $[\overline{H}_{u,n}]$ and $[\overline{\overline{H}}_{u,n}]$ to represent the matrix multiplication between $[H_u]$ and sine-cosine matrix.

$$[\overline{H}_{u,n}] = [H_u(r,z)][\overline{CSn}(\theta)]$$

$$= \begin{bmatrix} h_1\cos(n\theta) & 0 & 0 & h_2\cos(n\theta) & 0 & \cdots \\ 0 & h_1\sin(n\theta) & 0 & 0 & h_2\sin(n\theta) & \cdots \\ 0 & 0 & h_1\cos(n\theta) & 0 & 0 & \end{bmatrix} \tag{A-16}$$

$$\left[\bar{\bar{H}}_{u,n}\right] = [H_u(r,z)]\left[\overline{\overline{CSn}}(\theta)\right]$$

$$= \begin{bmatrix} h_1 sin(n\theta) & 0 & 0 & h_2\sin(n\theta) & 0 \\ 0 & -h_1\cos(n\theta) & 0 & 0 & -h_2\cos(n\theta) & \cdots \\ 0 & 0 & h_1\sin(n\theta) & 0 & 0 \end{bmatrix}$$

(A-17)

With the new matrices defined in Eqs. A-16 and A-17, Eq. A-10 reduces to

$$\begin{bmatrix} u_r \\ u_\theta \\ u_z \end{bmatrix} = \sum_{n=0}^{\infty}\left\{\left[\bar{H}_{u,n}\right]\left[\hat{\bar{u}}_n\right] + \left[\bar{\bar{H}}_{u,n}\right]\left[\hat{\bar{\bar{u}}}_n\right]\right\}$$

(A-18)

Because displacement solutions are in the form of Fourier n-harmonic, their corresponding strains also possess the same Fourier form. By differentiating the displacement matrix in Eq. A-10, the result is the strain matrix in the cylindrical coordinate.

$$[\epsilon] = \begin{bmatrix} \epsilon_r \\ \epsilon_\theta \\ \epsilon_z \\ 2\epsilon_{r\theta} \\ 2\epsilon_{\theta z} \\ 2\epsilon_{rz} \end{bmatrix} = \begin{bmatrix} \epsilon_r \\ \epsilon_\theta \\ \epsilon_z \\ \gamma_{r\theta} \\ \gamma_{\theta z} \\ \gamma_{rz} \end{bmatrix} = \begin{bmatrix} \partial/\partial r & 0 & 0 \\ 1/r & \partial/r\partial\theta & 0 \\ 0 & 0 & \partial/\partial z \\ \partial/r\partial\theta & \partial/\partial r - 1/r & 0 \\ 0 & \partial/\partial z & \partial/r\partial\theta \\ \partial/\partial z & 0 & \partial/\partial r \end{bmatrix}\begin{bmatrix} u_r \\ u_\theta \\ u_z \end{bmatrix}$$

(A-19)

Applying displacement matrix in Eq. A-18 into Eq. A-19 and define derivative matrix, $[\partial]$, Eq. A-19 becomes

$$[\epsilon] = \sum_{n=0}^{\infty}\left\{[\partial]\left[\bar{H}_{u,n}\right]\left[\hat{\bar{u}}_n\right] + [\partial]\left[\bar{\bar{H}}_{u,n}\right]\left[\hat{\bar{\bar{u}}}_n\right]\right\}$$

(A-20)

By introducing new matrices, $\left[\bar{B}_{u,n}\right]$ and $\left[\bar{\bar{B}}_{u,n}\right]$, as defined in Eqs. A-22 and A-23 respectively to represent the derivative of n-harmonic shape function matrices, this simplifies Eq. A-20 to

$$[\epsilon] = \sum_{n=0}^{\infty} \left\{ [\bar{B}_{u,n}][\hat{\bar{u}}_n] + [\bar{\bar{B}}_{u,n}][\hat{\bar{\bar{u}}}_n] \right\} \tag{A-21}$$

where

$$[\bar{B}_{u,n}] = [\partial][\bar{H}_{u,n}]$$

$$= \begin{bmatrix}
\partial h_1/\partial r \cdot \cos(n\theta) & 0 & 0 \\
h_1/r \cdot \cos(n\theta) & nh_1/r \cdot \cos(n\theta) & 0 \\
0 & 0 & \partial h_1/\partial z \cdot \cos(n\theta) \\
-nh_1/r \cdot \sin(n\theta) & (\partial h_1/\partial r - h_1/r) \cdot \sin(n\theta) & 0 \\
0 & \partial h_1/\partial z \cdot \sin(n\theta) & -nh_1/r \cdot \sin(n\theta) \\
\partial h_1/\partial z \cdot \cos(n\theta) & 0 & \partial h_1/\partial r \cdot \cos(n\theta)
\end{bmatrix} \cdots \tag{A-22}$$

$$[\bar{\bar{B}}_{u,n}] = [\partial][\bar{\bar{H}}_{u,n}]$$

$$= \begin{bmatrix}
\partial h_1/\partial r \cdot \sin(n\theta) & 0 & 0 \\
h_1/r \cdot \sin(n\theta) & nh_1/r \cdot \sin(n\theta) & 0 \\
0 & 0 & \partial h_1/\partial z \cdot \sin(n\theta) \\
nh_1/r \cdot \cos(n\theta) & -(\partial h_1/\partial r - h_1/r) \cdot \cos(n\theta) & 0 \\
0 & -\partial h_1/\partial z \cdot \cos(n\theta) & nh_1/r \cdot \cos(n\theta) \\
\partial h_1/\partial z \cdot \sin(n\theta) & 0 & \partial h_1/\partial r \cdot \sin(n\theta)
\end{bmatrix} \cdots \tag{A-23}$$

In linear elasticity theory, stress has a linear relation with strain. Finally, the linear elastic constitutive stress-strain relation in the Fourier n-harmonic form is:

$$[\sigma] = [C][\epsilon] = [C] \sum_{n=0}^{\infty} \left\{ [\bar{B}_{u,n}][\hat{\bar{u}}_n] + [\bar{\bar{B}}_{u,n}][\hat{\bar{\bar{u}}}_n] \right\} \tag{A-24}$$

The Solutions of the Cosine Stress Boundary

In geomechanic problems subjected to the earth in-situ stresses, the stress boundaries are the maximum horizontal stress, the minimum horizontal stress and the overburden. The two horizontal stresses serve as basis of the radial and the tangential

boundary stresses in the wellbore model, and the overburden is equivalent to the vertical boundary stress. When the in-situ stresses, which are defined in the Cartesian coordinates, are transformed to the cylindrical coordinates, the cylindrical boundary stresses are in the Fourier form consisting of the first harmonic cosine and sine terms as presented in the section 5.2.2.

This section provides a derivation of the Fourier finite-element formulation only for the single-bar term. The derivation of the double-bar term is analogous and shares most of the resultant matrices with single-bar term when integrate over $-\pi$ to π.

The approach used here is to match the term in the Fourier series of the displacement and pore pressure solutions when the single-hat term of the boundary stresses are applied.

Let assume the single-bar term of the displacement solutions and the pore pressure solution are in the form of sine or cosine Fourier series as shown below.

$$u_r(r,\theta,z) = \sum_{n=0}^{\infty} \bar{u}_{r,n}(r,z)\cos(n\theta) \qquad (A\text{-}25)$$

$$u_\theta(r,\theta,z) = \sum_{n=0}^{\infty} \bar{u}_{\theta,n}(r,z)\sin(n\theta) \qquad (A\text{-}26)$$

$$u_z(r,\theta,z) = \sum_{n=0}^{\infty} \bar{u}_{z,n}(r,z)\cos(n\theta) \qquad (A\text{-}27)$$

$$P(r,\theta,z) = \sum_{n=0}^{\infty} \bar{P}_n(r,z)\cos(n\theta) \qquad (A\text{-}28)$$

113

Note that θ is a positive counter-clockwise horizontal angle from the direction of the earth minimum horizontal stress.

After differentiating the displacements in Eqs. A-25 to A-27, they become three dimensional strains. In the cylindrical coordinate, the strains correspond to Eqs. A-25 to A-28 are

$$\epsilon_r(r,\theta,z) = \frac{\partial u_r}{\partial r} = \sum_{n=0}^{\infty} \frac{\partial \bar{u}_{r,n}(r,z)\cos(n\theta)}{\partial r} \tag{A-29}$$

$$\epsilon_\theta(r,\theta,z) = \frac{u_r}{r} + \frac{\partial u_\theta}{r\partial \theta} = \sum_{n=0}^{\infty} \left\{ \frac{\bar{u}_{r,n}(r,z)\cos(n\theta)}{r} + \frac{\partial \bar{u}_{\theta,n}(r,z)\sin(n\theta)}{r\partial \theta} \right\} \tag{A-30}$$

$$\epsilon_z(r,\theta,z) = \frac{\partial u_z}{\partial z} = \sum_{n=0}^{\infty} \frac{\partial \bar{u}_{z,n}(r,z)\cos(n\theta)}{\partial z} \tag{A-31}$$

By applying the linear elastic stress-strain constitutive relation to convert strains in Eq. A-29 to A-31 into stresses, the resulting stresses are

$$\sigma_r = \sum_{n=0}^{\infty} \left\{ (\lambda + 2G)\frac{\partial \bar{u}_{r,n}}{\partial r}\cos(n\theta) + \lambda\left[\frac{\bar{u}_{r,n}}{r}\cos(n\theta) + \frac{\bar{u}_{\theta,n}}{r}\cos(n\theta)\right] \right. $$
$$\left. + \lambda\frac{\partial \bar{u}_{z,n}}{\partial z}\cos(n\theta) \right\} \tag{A-32}$$

$$\sigma_\theta = \sum_{n=0}^{\infty} \left\{ \lambda\frac{\partial \bar{u}_{r,n}}{\partial r}\cos(n\theta) + (\lambda + 2G)\left[\frac{\bar{u}_{r,n}}{r}\cos(n\theta) + \frac{\bar{u}_{\theta,n}}{r}\cos(n\theta)\right] \right. $$
$$\left. + \lambda\frac{\partial \bar{u}_{z,n}}{\partial z}\cos(n\theta) \right\} \tag{A-33}$$

$$\sigma_z = \sum_{n=0}^{\infty} \left\{ \lambda \frac{\partial \bar{u}_{r,n}}{\partial r} \cos(n\theta) + \lambda \left[\frac{\bar{u}_{r,n}}{r} \cos(n\theta) + \frac{\bar{u}_{\theta,n}}{r} \cos(n\theta) \right] \right. \tag{A-34}$$

$$\left. + (\lambda + 2G) \frac{\partial \bar{u}_{z,n}}{\partial z} \cos(n\theta) \right\}$$

The pore pressure at the boundary is constant and can be described by the zero harmonic of the cosine term in the Fourier series. This leads to a pore pressure solution having only the single-bar term which has the same form as Eq. A-28.

With the displacement solutions having only the single-bar term as given in Eqs. A-25 to A-27, the stresses corresponding to these displacements comprise of the cosine-term in their Fourier n-harmonic forms. Therefore, one can conclude that the solutions provide in Eqs. A-25 to A-28 are results of the single-bar term in the Fourier series of the boundary stress.

In the subsequent sections, only derivations for the solutions related to the single-bar terms are presented. The equations derived from the double-bar terms will be given at the end without detail of derivation.

Poroelasticity – Deformation Equation

The equation governing a deformation in the poroelasticity theory is derived from the mechanical equilibrium equation. Because no thermal strain exists in this poroelastic model, the total stress accounts only for an effective stress and a pore pressure.

$$\nabla \cdot \langle \sigma \rangle + f_b = 0 \tag{A-35}$$

The total stress in a compressive positive sign convention for the poroelastic material is

$$[\sigma] = [\sigma'] + \alpha \begin{bmatrix} 1 \\ 1 \\ 1 \\ 0 \\ 0 \\ 0 \end{bmatrix} P \tag{A-36}$$

The Fourier-assisted finite-element formulation for Eqs. A-35 and A-36 for the single-bar terms are

$$\sum_{n=0}^{\infty} \left\{ \iiint [\bar{B}_{u,n}]^T [C] [\bar{B}_{u,n}] d\theta r dr dz [\hat{\bar{u}}_n] \right.$$

$$+ \alpha \iiint [\bar{B}_{u,n}]^T \cos(n\theta) \, d\theta [M_u][H_p] \, r dr dz [\hat{\bar{P}}_n] \right\} \tag{A-37}$$

$$= \sum_{n=0}^{\infty} [F_{ex,n}]$$

where

$$[M_U] = [1 \quad 1 \quad 1 \quad 0 \quad 0 \quad 0]^T \tag{A-38}$$

$$[H_p] = [h_1 \quad h_2 \quad h_3 \quad h_4 \quad \cdots] \tag{A-39}$$

To simplify a volumetric integration on the first term in the left-hand side of Eq. A-37, one shall start from a line integration of the tangential parameter from $-\pi$ to π. The multiplication result of $[\bar{B}_{u,n}]^T [C][\bar{B}_{u,n}]$ is a matrix with elements composing of either $\cos^2(n\theta)$ or $\sin^2(n\theta)$. These terms give a common factor of π for $n > 0$ and 2π for $n = 0$ when they are integrated over $-\pi$ to π. Therefore, the first integrand term in the left-hand side becomes

116

$$\iint \int_{-\pi}^{\pi} [\bar{B}_{u,n}]^T [C][\bar{B}_{u,n}] d\theta r dr dz = \iint \omega_n [B_{coef,u,n}]^T [C][B_{coef,u,n}] r dr dz \qquad \text{(A-40)}$$

The term ω_n is a coefficient that is π when $n > 0$ and 2π when $n = 0$. The

definition of the new matrix, $[B_{coef,u,n}]$, in Eq. A-40 is

$$[B_{coef,u,n}] = \begin{bmatrix} \partial h_1/\partial r & 0 & 0 \\ h_1/r & nh_1/r & 0 \\ 0 & 0 & \partial h_1/\partial z \\ -nh_1/r & (\partial h_1/\partial r - h_1/r) & 0 \\ 0 & \partial h_1/\partial z & -nh_1/r \\ \partial h_1/\partial z & 0 & \partial h_1/\partial r \end{bmatrix} \cdots \qquad \text{(A-41)}$$

It is worth to note that $[B_{coef,u,n}]$ also applies to the double-bar term of full n-

harmonic Fourier form.

Owing to a symmetric property of the trigonometry integrand in Eq. A-40, the

results from single-bar and double-bar terms are equivalent.

$$\int_{-\pi}^{\pi} [\bar{B}_{u,n}]^T [C][\bar{B}_{u,n}] d\theta = \int_{-\pi}^{\pi} [\bar{\bar{B}}_{u,n}]^T [C][\bar{\bar{B}}_{u,n}] d\theta \qquad \text{(A-42)}$$

Apply the Gauss-Legendre Integration technique for an axisymmetric geometry,

Eq. A-40 changes to

$$\iiint [\bar{B}_{u,n}]^T [C] [\bar{B}_{u,n}] d\theta r dr dz$$

$$= \sum_{int}^{area} \omega_n [B_{coef,u,n}]^T [C][B_{coef,u,n}] \cdot x_{int} w_{int} \det J \qquad \text{(A-43)}$$

The second term in the left-hand side of Eq. A-37 represents alteration of total

stress from the pore pressure change. We shall begin with the formulation of tangential

integral term. By investigating the term $[\bar{B}_{u,n}]^T \cos(n\theta)$, elements of the resulting matrix

consist of terms with $\cos^2(n\theta)$ or $sin(n\theta)\cos(n\theta)$. The line integral of $\cos^2(n\theta)$ over $-\pi$ to π gives π for $n > 0$ and 2π for $n = 0$; the line integral of $sin(n\theta)\cos(n\theta)$ gives zero. These integration properties simplify the second term in the left-hand side of Eq. A-37 to

$$\alpha \iint \left\{ \int_{-\pi}^{\pi} [\bar{B}_{u,n}]^T \cos(n\theta)\, d\theta \right\} [M_u][H_p] r\, dr\, dz$$

$$= \alpha \iint \omega_n [B_{coef,pu,n}]^T [M_u][H_p] r\, dr\, dz \tag{A-44}$$

where

$$[B_{coef,pu,n}] = \begin{bmatrix} \partial h_1/\partial r & 0 & 0 \\ h_1/r & nh_1/r & 0 \\ 0 & 0 & \partial h_1/\partial z \\ 0 & 0 & 0 \\ 0 & 0 & 0 \\ \partial h_1/\partial z & 0 & \partial h_1/\partial r \end{bmatrix} \cdots \tag{A-45}$$

Similar to Eq. A-42, the relation in Eq. A-44 also represents the integrand of the double-bar term.

$$\alpha \iint \left\{ \int_{-\pi}^{\pi} [\bar{\bar{B}}_{u,n}]^T \sin(n\theta)\, d\theta \right\} [M_u][H_p] r\, dr\, dz$$

$$= \alpha \iint \omega_n [B_{coef,pu,n}]^T [M_u][H_p] r\, dr\, dz \tag{A-46}$$

By applying the Gauss-Legendre Integration technique for an axisymmetric geometry on Eq. A-44, it becomes

$$\alpha \iiint \left[\bar{B}_{u,n}\right]^T \cos(n\theta) \, d\theta \, [M_u][H_p] \, r \, dr \, dz$$

$$= \sum_{int}^{area} \alpha \omega_n \left[B_{coef,pu,n}\right]^T [M_u][H_p] \cdot x_{int} w_{int} \, det \, J \tag{A-47}$$

By substituting Eqs. A-43 and A-47 into the deformation equation, Eq. A-37, the result is the Fourier assisted finite-element formulation which is

$$\sum_{n=0}^{\infty} \left\{ \sum_{int}^{area} \omega_n \left[B_{coef,u,n}\right]^T [C][B_{coef,u,n}] \cdot x_{int} w_{int} \, det \, J \, [\hat{\bar{u}}_n] \right.$$

$$\left. + \alpha \sum_{int}^{area} \omega_n \left[B_{coef,pu,n}\right]^T [M_u][H_p] \cdot x_{int} w_{int} \, det \, J \left[\hat{\bar{P}}_n\right] \right\} \tag{A-48}$$

$$= \sum_{n=0}^{\infty} \left[F_{ex,n}\right]$$

Introducing new finite-element matrices, Eq. A-48 is transformed into the final form of finite-element matrix equation.

$$\sum_{n=0}^{\infty} \left\{ [K_{u,n}^g][\hat{\bar{u}}_n] + [K_{pu,n}^g]\left[\hat{\bar{P}}_n\right] \right\} = \sum_{n=0}^{\infty} [F_{ex,n}] \tag{A-49}$$

where

$$[K_{u,n}^g] = \sum_{ele}^{all} \left\{ \sum_{int}^{area} \omega_n \left[B_{coef,u,n}\right]^T [C][B_{coef,u,n}] \cdot x_{int} w_{int} \, det \, J \right\}_{@1 \, ele} \tag{A-50}$$

$$[K_{pu,n}^g] = \sum_{ele}^{all} \left\{ \sum_{int}^{area} \alpha \omega_n \left[B_{coef,pu,n}\right]^T [M_u][H_p] \cdot x_{int} w_{int} \, det \, J \right\}_{@1 \, ele} \tag{A-51}$$

$$[F_{ex,n}] = Nodal \ force \ at \ the \ boundary \ nodes \tag{A-52}$$

The double-bar term has the same finite-element matrix equation as Eq. A-49 due to the symmetric property of trigonometry integration between sine and cosine.

Moreover, this kind of the Fourier solution possesses a linear property; thus, it allows solution of each harmonic term to be solved separately. The complete solution is a superposition of the solutions from all harmonics.

Poroelasticity – Pressure Diffusivity Equation

The pressure diffusivity describes a flow of a pore fluid inside a porous media. The governing equation presents a coupled relation between a pore pressure and a deformation as shown below:

$$\frac{\partial p}{\partial t} = M\left[\frac{k}{\mu}\nabla^2 p + \alpha\frac{\partial \epsilon_{kk}}{\partial t}\right] \tag{A-53}$$

The definition of M and ϵ_{kk} are presented in Eqs. 4.42 and 4.17 respectively.

To simplify the complexity of the Fourier-assisted finite-element formulation, each term in Eq. A-53 shall be investigated individually starting from the first term in the left-hand side which is the time derivative of the pore pressure. Using the pore pressure solution in the Fourier form as described in Eq. A-28, the result is

$$\frac{\partial p}{\partial t} = \frac{1}{\Delta t}\sum_{n=0}^{\infty}\left\{\left[\bar{H}_{p,n}\right]^T\left[\bar{H}_{p,n}\right]\left[\widehat{\bar{P}}_n^{\,t+1}\right] - \left[\bar{H}_{p,n}\right]^T\left[\bar{H}_{p,n}\right]\left[\widehat{\bar{P}}_n^{\,t}\right]\right\} \tag{A-54}$$

where

$$\left[\bar{H}_{p,n}\right] = \begin{bmatrix} h_1\cos(n\theta) & h_2\cos(n\theta) & h_3\cos(n\theta) & \cdots \end{bmatrix} \tag{A-55}$$

By using the pore pressure solution as shown in Eq. A-28, the first term in the right-hand side becomes

$$M \frac{k}{\mu} \nabla^2 p = -M \frac{k}{\mu} \sum_{n=0}^{\infty} \left\{ \eta [\bar{B}_{p,n}]^T [\bar{B}_{p,n}] [\hat{\bar{P}}_n^{t+1}] + (1-\eta)[\bar{B}_{p,n}]^T [\bar{B}_{p,n}] [\hat{\bar{P}}_n^{t}] \right\} \qquad \text{(A-56)}$$

where

$$[\bar{B}_{p,n}] = [\partial][\bar{H}_{p,n}]$$

$$= \begin{bmatrix} \partial h_1/\partial r \cdot \cos(n\theta) & \partial h_2/\partial r \cdot \cos(n\theta) & \partial h_3/\partial r \cdot \cos(n\theta) & \\ -nh_1 \sin(n\theta) & -nh_2 \sin(n\theta) & -nh_3 \sin(n\theta) & \cdots \\ \partial h_1/\partial z \cdot \sin(n\theta) & \partial h_2/\partial z \cdot \sin(n\theta) & \partial h_3/\partial z \cdot \sin(n\theta) & \end{bmatrix}$$

(A-57)

The last term is the second term in the right-hand side in Eq. A-53 which presents a relation of the displacement solutions to pore pressure change. With the displacement solutions in the Fourier series form given by Eqs. A-25 to-27, this coupled term transforms to

$$\alpha M \frac{\partial \epsilon_{kk}}{\partial t} = \frac{\alpha M}{\Delta t} \sum_{n=0}^{\infty} \left\{ [\bar{H}_{p,n}]^T [M_u]^T [\bar{B}_{u,n}][\hat{u}_n^{t+1}] + [\bar{H}_{p,n}]^T [M_u]^T [\bar{B}_{u,n}][\hat{u}_n^{t}] \right\} \qquad \text{(A-58)}$$

By substituting Eqs. A-54, A-56 and A-58 into Eq. A-53 and making use of the Crank-Nicholson time scheme, the result is Eq. A-53 in a finite-element equation which is

$$\sum_{n=0}^{\infty} \left\{ \frac{1}{\Delta t} \iiint [\bar{H}_{p,n}]^T [\bar{H}_{p,n}] d\theta dr dz \right.$$

$$\left. + M \frac{k}{\mu} \iiint \eta [\bar{B}_{p,n}]^T [\bar{B}_{p,n}] d\theta dr dz \right\} [\hat{\bar{P}}_n^{t+1}]$$

$$- \sum_{n=0}^{\infty} \frac{\alpha M}{\Delta t} \iiint [\bar{H}_{p,n}]^T [M_u]^T [\bar{B}_{u,n}] d\theta dr dz [\hat{\bar{u}}_n^{t+1}]$$

$$(A\text{-}59)$$

$$= \sum_{n=0}^{\infty} \left\{ \frac{1}{\Delta t} \iiint [\bar{H}_{p,n}]^T [\bar{H}_{p,n}] d\theta dr dz \right.$$

$$\left. - M \frac{k}{\mu} \iiint (1 - \eta) [\bar{B}_{p,n}]^T [\bar{B}_{p,n}] d\theta dr dz \right\} [\hat{\bar{P}}_n^{t}]$$

$$- \sum_{n=0}^{\infty} \frac{\alpha M}{\Delta t} \iiint [\bar{H}_{p,n}]^T [M_u]^T [\bar{B}_{u,n}] d\theta dr dz [\hat{\bar{u}}_n^{t}]$$

Let consider three tangential integral terms in Eq. A-59 separately. The first tangential integrand belongs to the first term in the left-hand and right-hand side of Eq. A-59. It can be simplified into a constant matrix term as shown below:

$$\int_{-\pi}^{\pi} [\bar{H}_{p,n}]^T [\bar{H}_{p,n}] d\theta = [H_p]^T [H_p] \int_{-\pi}^{\pi} \cos^2(n\theta) \, d\theta = \omega_n [H_p]^T [H_p] \qquad (A\text{-}60)$$

The second tangential integrand governs the properties of pressure diffusion in pore space. It is the second term of both the left-hand and the right-hand sides of Eq. A-59. These terms possess $[\bar{B}_{p,n}]^T [\bar{B}_{p,n}]$ and their elements of the resulting matrix consist of either $\cos^2(n\theta)$ or $\sin^2(n\theta)$, which gives π for $n > 0$ and 2π for $n = 0$, when it is integrated over $-\pi$ to π. As a result, this second tangential integral term becomes

$$\int_{-\pi}^{\pi} [\bar{B}_{p,n}]^T [\bar{B}_{p,n}] d\theta = \omega_n [B_{coef,p,n}]^T [B_{coef,p,n}] \tag{A-61}$$

where

$$[B_{coef,p,n}] = \begin{bmatrix} \partial h_1/\partial r & \partial h_2/\partial r & \partial h_3/\partial r \\ -nh_1 & -nh_2 & -nh_3 & \cdots \\ \partial h_1/\partial z & \partial h_2/\partial z & \partial h_3/\partial z \end{bmatrix} \tag{A-62}$$

The last tangential integrand is the third term of the left-hand and right-hand sides. It represents the relation of displacements in pressure diffusivity equation. This term is

$$\int_{-\pi}^{\pi} [\bar{H}_{p,n}]^T [M_u]^T [\bar{B}_{u,n}] d\theta = [H_p]^T [M_u]^T \int_{-\pi}^{\pi} \cos(n\theta) [\bar{B}_{u,n}] d\theta \tag{A-63}$$

As shown in Eq. A-45, the integral solution of the term $\int_{-\pi}^{\pi} \cos(n\theta) [\bar{B}_{u,n}] d\theta$ has a greatly simplified form. Apply same formulation done to Eq. A-45, Eq. A-63 becomes

$$\int_{-\pi}^{\pi} [\bar{H}_{p,n}]^T [M_u]^T [\bar{B}_{u,n}] d\theta = \omega_n [H_p]^T [M_u]^T [B_{coef,pu,n}] \tag{A-64}$$

By substituting Eqs. A-60, A-61 and A-64 into Eq. A-59, the result is

$$\sum_{n=0}^{\infty}\left\{\frac{1}{\Delta t}\iint \omega_n[H_p]^T[H_p]\,rdrdz\right.$$

$$\left.+ M\eta\frac{k}{\mu}\iint \omega_n[B_{coef,p,n}]^T[B_{coef,p,n}]\,rdrdz\right\}\left[\widehat{\bar{P}}_n^{\,t+1}\right]$$

$$-\sum_{n=0}^{\infty}\frac{\alpha M}{\Delta t}\iint \omega_n[H_p]^T[M_u]^T[B_{coef,pu,n}]\,rdrdz[\hat{\bar{u}}_n^{t+1}]$$

$$=\sum_{n=0}^{\infty}\left\{\frac{1}{\Delta t}\iint \omega_n[H_p]^T[H_p]\,rdrdz - M(1\right.$$

$$\left.-\eta)\frac{k}{\mu}\iint \omega_n[B_{coef,p,n}]^T[B_{coef,p,n}]\,rdrdz\right\}\left[\widehat{\bar{P}}_n^{\,t}\right]$$

$$-\sum_{n=0}^{\infty}\frac{\alpha M}{\Delta t}\iint \omega_n[H_p]^T[M_u]^T[B_{coef,pu,n}]\,rdrdz[\hat{\bar{u}}_n^{t}]$$

(A-65)

By applying the Gauss-Legendre Integration technique in an axisymmetric geometry and introducing new matrices to change Eq. A-65 to the final form of the finite-element equation which is

$$\sum_{n=0}^{\infty}\left\{[K_{up,n}^g][\hat{\bar{u}}_n^{t+1}] + [K_{p,n}^g]\left[\widehat{\bar{P}}_n^{\,t+1}\right]\right\} = \sum_{n=0}^{\infty}\left\{[K_{up,n}^g][\hat{\bar{u}}_n^{t}] + [R_{p,n}^g]\left[\widehat{\bar{P}}_n^{\,t}\right]\right\}$$

(A-66)

where

$$[K_{up,n}^g] = -\frac{M}{\Delta t}[K_{pu,n}^g]^T$$

(A-67)

$$= -\sum_{ele}^{all}\left\{\frac{M}{\Delta t}\sum_{int}^{area}\alpha\omega_n[H_p]^T[M_u]^T[B_{coef,pu,n}]\cdot x_{int}w_{int}\,det J\right\}_{@1\,ele}$$

$$[K_{p,n}^g] = [Q_{p,n}^g] + \eta[W_{p,n}^g]$$

(A-68)

$$[R_{p,n}^g] = [Q_{p,n}^g] - (1 - \eta)[W_{p,n}^g] \tag{A-68}$$

The matrices in Eqs. A-68 and A-69 are

$$[Q_{p,n}^g] = \sum_{ele}^{all} \left\{ \frac{1}{\Delta t} \sum_{int}^{area} \omega_n [H_p]^T [H_p] \cdot x_{int} w_{int} \, det \, J \right\}_{@1 \, ele} \tag{A-69}$$

$$[W_{p,n}^g] = \sum_{ele}^{all} \left\{ M \frac{k}{\mu} \sum_{int}^{area} \omega_n [B_{coef,p,n}]^T [B_{coef,p,n}] \cdot x_{int} w_{int} \, det \, J \right\}_{@1 \, ele} \tag{A-70}$$

The formulation for the double-bar term gives the same result as Eq. A-66. The matrices defined in Eqs. A-67 to A-70 are also applicable to the equation of the double-bar term.

Note again that all the formulations in this appendix are compressive positive sign convention. When writing finite-element program, the sign shall be converted to tensile positive to match with the nature of the finite-element method.

THE NUMERICAL FORMULATION FOR THERMALLY INDUCED STRESS SOLUION WITH THE COMBINED FINITE-DIFFERENT/FINITE-ELEMENT METHOD

This appendix presents a derivation of a numerical formulation of the thermally induced stresses. The model is governed by the partially coupled thermoporoelasticity theory and uses the finite-difference together with the finite-element techniques to formulate numerical equations. The finite-difference method is selected for the thermal diffusivity and the pressure diffusivity equations. This helps avoid a spurious oscillation of pore pressure and temperature solutions when a small time increment is used in finite-element method. The deformation equation is formulated by the finite-element method which gives an excellent result.

As presented in the chapter 4, there are three governing equations in the thermoporoelasticity theory. They are thermal diffusivity equation, pressure diffusivity equation and deformation equation which are presented separately in sections below.

Thermoporoelasticity - Thermal Diffusivity Equation

The transient heat balance equation for a heat conduction process in the shale formation as discussed in chapter 4 is

$$\rho_b C_b \frac{\partial T}{\partial t} = \kappa^T \nabla^2 T \tag{B-1}$$

Expand differential equation of Eq. B-1 using the cylindrical coordinate system, the result is

$$\rho_b C_b \frac{\partial T}{\partial t} = \kappa^T \left(\frac{1}{r} \frac{\partial T}{\partial r} + \frac{\partial^2 T}{\partial r^2} + \frac{\partial^2 T}{\partial z^2} \right) \tag{B-2}$$

Following the finite-difference formulation method, a continuous temperature domain is transformed into a discrete domain. In the finite-difference form, Eq. B-2 can be represented by

$$\frac{\rho_b C_b}{\Delta t} \left(T_{i,j}^{t+1} - T_{i,j}^t \right)$$

$$= \kappa^T \left[\frac{1}{r \Delta r} \left(0.5 T_{i+1,j} - 0.5 T_{i-1,j} \right) \right.$$

$$+ \frac{1}{\Delta r^2} \left(T_{i+1,j} - 2 T_{i,j} + T_{i-1,j} \right)$$

$$\left. + \frac{1}{\Delta z^2} \left(T_{i,j+1} - 2 T_{i,j} + T_{i-1,j} \right) \right] \tag{B-3}$$

The subscript index 'i' is for the location in the radial direction; 'j' is for location in the vertical direction; 't' and 't+1' refer to a time order of the solution.

Using the Crank-Nicholson time scheme donated with η and doing some rearrangements, Eq. B-3 becomes

$$A_T T_{i-1,j}^{t+1} + B_T T_{i,j}^{t+1} + C_T T_{i+1,j}^{t+1} + D_T T_{i,j-1}^{t+1} + E_T T_{i,j+1}^{t+1}$$

$$= F_T T_{i-1,j}^t + G_T T_{i,j}^t + H_T T_{i+1,j}^t + I_T T_{i,j-1}^t + J_T T_{i,j+1}^t \tag{B-4}$$

The coefficients used in Eq. B-4 are

$$A_T = -0.5 \frac{\kappa^T \eta}{r \Delta r} + \frac{\kappa^T \eta}{(\Delta r)^2} \tag{B-5}$$

$$B_T = -\frac{2\kappa^T\eta}{(\Delta r)^2} - \frac{2\kappa^T\eta}{(\Delta z)^2} - \frac{\rho_b C_b}{\Delta t} \tag{B-6}$$

$$C_T = 0.5\frac{\kappa^T\eta}{r\Delta r} + \frac{\kappa^T\eta}{(\Delta r)^2} \tag{B-7}$$

$$D_T = E_T = \frac{\kappa^T\eta}{(\Delta z)^2} \tag{B-8}$$

$$F_T = 0.5\frac{\kappa^T(1-\eta)}{r\Delta r} - \frac{\kappa^T(1-\eta)}{(\Delta r)^2} \tag{B-9}$$

$$G_T = \frac{2\kappa^T(1-\eta)}{(\Delta r)^2} + \frac{2\kappa^T(1-\eta)}{(\Delta z)^2} - \frac{\rho_b C_b}{\Delta t} \tag{B-10}$$

$$H_T = -0.5\frac{\kappa^T(1-\eta)}{r\Delta r} - \frac{\kappa^T(1-\eta)}{(\Delta r)^2} \tag{B-11}$$

$$I_T = J_T = -\frac{\kappa^T(1-\eta)}{(\Delta z)^2} \tag{B-12}$$

Let introduce nodal temperature vector $[\hat{T}]$ that has a nodal index number running in the same node order as a node assignment in pore pressure and displacement solution vectors. Eq. B-4 can be rearranged to

$$[K_T^g][\hat{T}^{t+1}] = [R_T^g][\hat{T}^t] \tag{B-13}$$

For all the nodes that are not at the boundary, the $[K_T^g]$ represents the left-hand side of Eq. B-4 with the coefficients listed in Eqs. B-5 to B-8. All the boundary temperatures except at the top of this model are constant values; thus, matrix elements at $K_T^g(n,n) = 1$, where n is a node number at the boundary. The top temperature boundary condition for this model is no vertical heat flux flow across the top boundary. The nodes along the top boundary have $K_T^g(n,n) = 1$ and $K_T^g(n,n_{below}) = -1$. The

index n represents the nodes at the top of the boundary and n_{below} is the node below the n node.

The $[R_T^g]$ represents the right-hand side of Eq. B-4 with the coefficients listed in Eqs. B-9 to B-12 for all none-boundary nodes. At the boundary where it is not at the top, $[R_T^g][\hat{T}^t]$, has a value of constant boundary temperature. The top boundary nodes have $[R_T^g][\hat{T}^t] = 0$.

Thermoporoelasticity - Pressure Diffusivity Equation

The transient pressure diffusivity equation in a partial differential form that decoupled deformation effect out from the equation is

$$\frac{\partial p}{\partial t} = \beta_{p,1} \nabla^2 p + \beta_{p,2} \frac{\partial T}{\partial t} \tag{B-14}$$

where

$$\beta_{p,1} = \frac{kM}{\mu} \tag{B-15}$$

$$\beta_{p,2} = M\left(\alpha \alpha_m^T + \phi \alpha_f^T - \phi \alpha_m^T\right) \tag{B-16}$$

The definitions of parameters used in the right-hand side of Eqs. B-15 and B-16 can be found in section 4.3.2.

Similar steps as for the thermal diffusivity equation, Eq. B-1, the differential terms in Eq. B-14 is expanded using the cylindrical coordinate system to get

$$\frac{\partial p}{\partial t} = \beta_{p,1}\left(\frac{1}{r}\frac{\partial p}{\partial r} + \frac{\partial^2 p}{\partial r^2} + \frac{\partial^2 p}{\partial z^2}\right) + \beta_{p,2}\frac{\partial T}{\partial t} \tag{B-17}$$

Following the finite-difference formulation method, a continuous pore pressure domain is transformed into a discrete domain. In the finite-difference numerical form, Eq. B-17 is

$$\frac{1}{\Delta t}\left(P_{i,j}^{t+1} - P_{i,j}^{t}\right)$$

$$= \beta_{p,1}\left[\frac{1}{r\Delta r}\left(0.5P_{i+1,j} - 0.5P_{i-1,j}\right)\right.$$

$$+ \frac{1}{\Delta r^{2}}\left(P_{i+1,j} - 2P_{i,j} + P_{i-1,j}\right)$$

$$\left. + \frac{1}{\Delta z^{2}}\left(P_{i,j+1} - 2P_{i,j} + P_{i-1,j}\right)\right] + \frac{\beta_{p,2}}{\Delta t}\left(T_{i,j}^{t+1} - T_{i,j}^{t}\right)$$

$$(\text{B-18})$$

The subscript index 'i' is for the location in the radial direction; 'j' is for location in the vertical direction; 't' and 't+1' refer to a time order of the solution.

Using the Crank-Nicholson time scheme donated with η, Eq. B-18 can be rearranged to get into a form as shown in Eq. B-19.

$$A_{P}P_{i-1,j}^{t+1} + B_{P}P_{i,j}^{t+1} + C_{P}P_{i+1,j}^{t+1} + D_{P}P_{i,j-1}^{t+1} + E_{P}P_{i,j+1}^{t+1} + F_{P}T_{i,j}^{t+1}$$

$$= G_{P}P_{i-1,j}^{t} + HP_{i,j}^{t} + I_{P}P_{i+1,j}^{t} + J_{P}P_{i,j-1}^{t} + K_{P}P_{i,j+1}^{t} + L_{P}T_{i,j}^{t}$$

$$(\text{B-19})$$

The coefficients used in Eq. B-19 are

$$A_{P} = -0.5\frac{\beta_{p,1}\eta}{r\Delta r} + \frac{\beta_{p,1}\eta}{(\Delta r)^{2}} \tag{B-20}$$

$$B_{P} = -\frac{2\beta_{p,1}\eta}{(\Delta r)^{2}} - \frac{2\beta_{p,1}\eta}{(\Delta z)^{2}} - \frac{1}{\Delta t} \tag{B-21}$$

$$C_{P} = 0.5\frac{\beta_{p,1}\eta}{r\Delta r} + \frac{\beta_{p,1}\eta}{(\Delta r)^{2}} \tag{B-22}$$

$$D_P = E_P = \frac{\beta_{p,1}\eta}{(\Delta z)^2} \tag{B-23}$$

$$F_P = \frac{\beta_{p,2}}{\Delta t} \tag{B-24}$$

$$G_P = 0.5\frac{\beta_{p,1}(1-\eta)}{r\Delta r} - \frac{\beta_{p,1}(1-\eta)}{(\Delta r)^2} \tag{B-25}$$

$$H_P = \frac{2\beta_{p,1}(1-\eta)}{(\Delta r)^2} + \frac{2\beta_{p,1}(1-\eta)}{(\Delta z)^2} - \frac{1}{\Delta t} \tag{B-26}$$

$$I_P = -0.5\frac{\beta_{p,1}(1-\eta)}{r\Delta r} - \frac{\beta_{p,1}(1-\eta)}{(\Delta r)^2} \tag{B-27}$$

$$J_P = K_P = -\frac{\beta_{p,1}(1-\eta)}{(\Delta z)^2} \tag{B-28}$$

$$L_P = \frac{\beta_{p,2}}{\Delta t} \tag{B-29}$$

Let introduce nodal pore pressure vector $[\hat{P}]$ that has a nodal index number running in the same node order as node assignment in temperature and displacement solution vectors. The result is Eq. B-19 in a numerical matrix equation.

$$[K_P^g][\hat{P}^{t+1}] + [K_{Tp}^g][\hat{T}^{t+1}] = [R_p^g][\hat{P}^t] + [R_{Tp}^g][\hat{T}^t] \tag{B-30}$$

For all the nodes that are not at the boundary, the $[K_P^g]$ represents the pore pressure terms in the left-hand side of Eq. B-19 with the coefficients listed in Eqs. B-20 to B-23. The $[K_{Tp}^g]$ represents the temperature term in the left-hand side of Eq. B-19 with coefficients of Eq. B-24 in its diagonal elements. All the boundary pore pressure except at the top and at the wellbore are constant; thus, matrix elements at $K_T^g(n,n) = 1$, where n is a node number at the boundary. The boundary condition of pore pressure at the top of the model applies no vertical fluid flow across the top boundary. The nodes along the

top boundary have $K_p^g(n, n) = 1$ and $K_p^g(n, n_{below}) = -1$. The index n represents the

nodes at the top of the boundary and n_{below} is the node right below the n node. Finally,

the boundary condition of the nodes along the wellbore-formation boundary depend on a

choice of boundary type whether it is permeable wellbore or impermeable wellbore. If

the wellbore is permeable, the pore pressure solutions along the wellbore are constant.

Therefore, the elements at $K_T^g(n, n)$ are 1 for all nodes at the wellbore. If the boundary

is impermeable wellbore, this is a no flow boundary condition. The elements at

$K_T^g(n, n)$ are 1 and at $K_T^g(n, n_{side})$ are -1.

The $[R_p^g]$ represents the pore pressure terms in the right-hand side of Eq. B-19

with the coefficients listed in Eqs. B-25 to B-28. The $[R_{Tp}^g]$ represents the temperature

term in the right-hand side of Eq. B-19 with the coefficients listed in Eq. B-29 in its

diagonal elements for all none-boundary nodes. At the boundary where it is not at the

top and at the wellbore, $[R_p^g][\hat{P}^t] + [R_{Tp}^g][\hat{T}^t]$, is constant boundary pore pressure. The

top boundary nodes have $[R_p^g][\hat{P}^t] + [R_{Tp}^g][\hat{T}^t] = 0$. If the wellbore is permeable,

$[R_p^g][\hat{P}^t] + [R_{Tp}^g][\hat{T}^t]$, has a value of wellbore pressure. If the wellbore is impermeable,

$[R_p^g][\hat{P}^t] + [R_{Tp}^g][\hat{T}^t] = 0$.

Thermoporoelasticity – Axisymmetric Equilibrium Equation

The equilibrium equation in a partial differential form of a stress vector with an

external force acting on the body and neglecting body force as discussed in chapter 4 is

$$\nabla \cdot \langle \sigma \rangle + [f_{ex}] = 0 \qquad\qquad (\text{B-31})$$

where

$$\langle \sigma \rangle = \begin{bmatrix} \sigma_r & \sigma_{rz} & 0 \\ \sigma_{rz} & \sigma_z & 0 \\ 0 & 0 & \sigma_\theta \end{bmatrix} \tag{B-32}$$

$$[f_{ex}] = \begin{bmatrix} f_{r,ex} \\ f_{z,ex} \end{bmatrix} \tag{B-33}$$

Stress relation following the thermoporoelastic theory in tensile positive is

$$[\sigma] = \begin{bmatrix} \sigma_r \\ \sigma_z \\ \sigma_\theta \\ \sigma_{rz} \end{bmatrix} = [C][\epsilon] - \alpha \begin{bmatrix} 1 \\ 1 \\ 1 \\ 0 \end{bmatrix} p - \beta_{T,2} \begin{bmatrix} 1 \\ 1 \\ 1 \\ 0 \end{bmatrix} T \tag{B-34}$$

where

$$[C] = \frac{2G}{(1-2v)} \begin{bmatrix} (1-v) & v & v & 0 \\ v & (1-v) & v & 0 \\ v & v & (1-v) & 0 \\ 0 & 0 & 0 & \frac{1}{2}(1-2v) \end{bmatrix} \tag{B-35}$$

$$[\epsilon] = \begin{bmatrix} \epsilon_r \\ \epsilon_z \\ \epsilon_\theta \\ \epsilon_{rz} \end{bmatrix} \tag{B-36}$$

and tensile strain is

$$[\epsilon] = [\partial][u] \tag{B-37}$$

where

$$[\partial] = \begin{bmatrix} \partial/\partial r & 0 \\ 0 & \partial/\partial z \\ 1/r & 0 \\ \partial/\partial z & \partial/\partial r \end{bmatrix} \tag{B-38}$$

$$[u] = \begin{bmatrix} u_r \\ u_z \end{bmatrix} \tag{B-39}$$

133

With Eqs. B-34 and B-37 describe the total stress in term of displacement and pore pressure, Eq. B-31 becomes

$$\nabla \cdot \left\{ [C][\partial][u] - \alpha \begin{bmatrix} 1 \\ 1 \\ 1 \\ 0 \end{bmatrix} p - \beta_{T,2} \begin{bmatrix} 1 \\ 1 \\ 1 \\ 0 \end{bmatrix} T \right\} + [f_{ex}] = 0 \tag{B-40}$$

Applying weighted-residual finite-element formulation to generate finite-element equation for formation deformation, Eq. B-40 becomes

$$\iiint [B_u]^T [C][B_u] dV \, [\hat{u}] - \alpha \iiint [B_u]^T \begin{bmatrix} 1 \\ 1 \\ 1 \\ 0 \end{bmatrix} [H_p] dV \, [\hat{P}]$$

$$- \beta_{T,2} \iiint [B_u]^T \begin{bmatrix} 1 \\ 1 \\ 1 \\ 0 \end{bmatrix} [H_T] dV \, [\hat{T}] = \iiint [H_u]^T [H_u] dV \, [f_{ex}] \tag{B-41}$$

Applying the Gauss-Legendre Integration technique for an axisymmetric geometry and introducing coefficient matrices to get the final numerical form as shown in Eq. B-42.

$$[K_u^g][\hat{u}] - [K_{pu}^g][\hat{P}] - [K_{Tu}^g][\hat{T}] = [F_u^g] \tag{B-42}$$

where

$$[K_u^g] = \sum_{ele}^{all} \left\{ \sum_{int}^{area} [B_{u,int}]^T [C_{int}][B_{u,int}] \cdot x_{int} w_{int} \, det \, J \right\}_{@1 \; element} \tag{B-43}$$

$$[K_{pu}^g] = \alpha \sum_{ele}^{all} \left\{ \sum_{int}^{area} [B_{u,int}]^T \begin{bmatrix} 1 \\ 1 \\ 1 \\ 0 \end{bmatrix} [H_{p,int}] \cdot x_{int} w_{int} \, det \, J \right\}_{@1 \; element} \tag{B-44}$$

$$[K_{Tu}^g] = \beta_{T,2} \sum_{ele}^{all} \left\{ \sum_{int}^{area} [B_{u,int}]^T \begin{bmatrix} 1 \\ 1 \\ 1 \\ 0 \end{bmatrix} [H_{T,int}] \cdot x_{int} w_{int} \, det J \right\}_{@1 \, element} \qquad (B\text{-}45)$$

$$[F_u^g] = Boundart \; Condition \; (if \; any) otherwise \; is \; zero \qquad (B\text{-}46)$$

$$[B_u] = \begin{bmatrix} \partial h_1/\partial x & 0 & \partial h_2/\partial x & 0 \\ 0 & \partial h_1/\partial y & 0 & \partial h_2/\partial y \\ h_1/x & 0 & h_2/x & 0 \\ \partial h_1/\partial y & \partial h_1/\partial x & \partial h_2/\partial y & \partial h_2/\partial x \end{bmatrix} \cdots \qquad (B\text{-}47)$$

$$[H_u] = \begin{bmatrix} h_1 & 0 & h_2 & 0 & h_3 & 0 & h_4 & 0 \\ 0 & h_1 & 0 & h_2 & 0 & h_3 & 0 & h_4 \end{bmatrix} \cdots \qquad (B\text{-}48)$$

Thermoporoelastic Model Finite-element

A combination of the thermal diffusivity equation, the pressure diffusivity equation and the equilibrium equation serves as governing relations for thermoporoelasticity theory. The derived three fundamental finite-element equations, which are Eqs. B-13, B-30, and B-42, are combined to give a form of linear equation representing a coupled thermoporoelastic finite-element equation for shale formation.

$$[K_{TPU}^g][X_{TPU}^{n+1}] = [R_{TPU}^g][X_{TPU}^n] + [F_{BDC}] \qquad (B\text{-}49)$$

where

$$[K_{TPU}^g] = \begin{bmatrix} [K_T^g] & 0 & 0 \\ [K_{Tp}^g] & [K_p^g] & 0 \\ -[K_{Tu}^g] & -[K_{pu}^g] & [K_u^g] \end{bmatrix} \qquad (B\text{-}50)$$

$$[X_{TPU}^{n+1}] = \begin{bmatrix} [\hat{T}_{i+1}] \\ [\hat{P}_{i+1}] \\ [\hat{u}_{i+1}] \end{bmatrix} \qquad (B\text{-}51)$$

$$[R_{TPU}^g] = \begin{bmatrix} [R_T^g] & 0 & 0 \\ [R_{Tp}^g] & [R_p^g] & 0 \\ 0 & 0 & 0 \end{bmatrix} \tag{B-52}$$

$$[X_{TPU}^n] = \begin{bmatrix} [\hat{T}_i] \\ [\hat{P}_i] \\ [\hat{u}_i] \end{bmatrix} \tag{B-53}$$

$$[F_{BDC}] = [F_T^g] + [F_u^g] \tag{B-54}$$